
HOMEPLUG AV TWG CONTRIBUTION

TO: HOMEPLUG AV TECHNICAL WORKING GROUP
DATE: 23rd July 2009
FROM: Pascal Pagani, France Telecom
SUBJECT: <FT_AV090723_01: OMEGA Project Input on PLC Channel>
RE:
SOURCE VERSION NUMBER OF CUT & PASTE TEXT:
DOES THIS AFFECT OTHER HP SPECS?

DESCRIPTION OF ISSUE

The Market Requirement Document for Home Plug AV2 [1] specifies an important increase in data rate, compared to the current Home Plug AV specifications. A 1 Gbps class PHY layer is requested, leading to a net throughput in the order of 600 Mbps.

One of the most direct ways to increase Home Plug AV current throughput is to increase the frequency band of operation above the current upper frequency of 30 MHz.

Currently, there is a lack of information on the characteristics of the powerline transmission medium at high frequencies. Parameters of interest are the Channel Transfer Function, characterizing the frequency attenuation and multipath nature of the transmission channel, the stationary noise, and the impulsive noise. Thus, there is a need for channel characterization and modelling studies for a better understanding of the physics of transmission above 30 MHz. The result of such studies will serve as an input for the development of robust and efficient signal processing techniques for the Home Plug AV2 specification.

PROPOSED SOLUTION

The following document is a deliverable from the ICT OMEGA Project, describing the PLC channel characterization and modelling studies conducted within this project.

The ICT OMEGA Project [2] is a 3-year, European Commission funded project, started in Jan. 2008. It involves 20 partners, from the European academic and industrial community. The goal is to define and implement a Gbps home network over heterogeneous technologies. Three main technologies are particularly investigated: radio communications in the 2.4 GHz, 5 GHz and 60 GHz bands; wireless optical communications; and Power Line Communications. In addition, a new method of inter-MAC convergence is developed for the inter-working of the different home network technologies. Demonstrations will be set up as proof of concept for an ultra broadband Home Network Area.

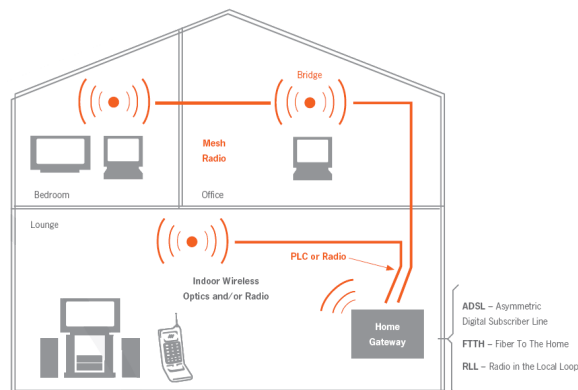


Fig. 1: The OMEGA Project concept

Within the OMEGA project, WP3 is devoted to the study of future indoor Power Line Communication (PLC) systems, with a particular focus on high throughput transmission systems, on a frequency range extending up to 100 MHz. OMEGA partners involved in WP3 include both industrials (France Telecom, Spidcom Technologies, Thyia) and universities (University of Udine, IETR).

The following document [3] presents the studies conducted within the OMEGA project on the characterization and modelling of the PLC channel. The main components of the PLC channel, namely the transfer function, the stationary noise and the impulsive noise, are fully characterized, based on both experimental studies and theoretical analysis. For each of these components, models are provided to be used for future system simulations.

In particular, the document provides:

- A detailed measurement method for the assessment of the channel characteristics
- Results on an experimental characterization of the PLC channel up to 100 MHz, based on an extensive measurement campaign
- Statistical models of the Channel Transfer Function based on both empirical and analytical approaches
- A study of the Channel Transfer Function based on the transmission line theory
- A model for the impulsive noise based on observations of the noise at the source
- A model for the stationary noise up to 100 MHz based on experimental results

This document is provided to serve as an input for the PLC channel characterization and modelling studies conducted within the Home Plug AV Technical Working Group.

References

- [1] HomePlug Powerline Alliance, Market Requirements for HomePlug AV2, April 2009.
- [2] OMEGA project website: <http://www.ict-omega.eu>
- [3] Seventh Framework Programme: Theme 3 ICT-213311 OMEGA, Deliverable D3.2, "PLC Channel Characterization and Modelling", Dec. 2008

SEVENTH FRAMEWORK PROGRAMME
THEME 3
Information & Communication Technologies (ICT)



ICT-213311
OMEGA



Deliverable D3.2

PLC Channel Characterization and Modelling

Contractual Date of Delivery:	31/12/2008
Actual Date of Delivery:	V1.0: 19/12/2008, V1.1: 10/07/2009
Editor(s):	Pascal PAGANI
Author(s):	Mohamed TLICH, Pascal PAGANI, Gautier AVRIL, Frédéric GAUTHIER, Ahmed ZEDDAM, Abdelkarim KARTIT, Olivier ISSON, Andrea TONELLO, Francesco PECILE, Salvatore D'ALESSANDRO, Tao ZHENG, Milena BIONDI, Gordana MIJIC, Klemen KRIZNAR, Jean-Yves BAUDAIS, Ali MAIGA
Work package:	WP3
Estimated person months:	15
Security:	PU
Nature:	Report
Version:	v1.1
Total number of pages:	112

Abstract

This OMEGA deliverable presents a detailed study of the channel characterization and modelling for the Power Line Communications (PLC) channel. The Channel Transfer Function (CTF) is first thoroughly investigated. The channel time-frequency characteristics are studied from a measurement campaign covering a frequency band up to 100 MHz. Different approaches for the modelling of the CTF are proposed. Statistical channel generators are derived from both experimental observations and analytical representations, and an approach based on the transmission line theory is provided to study the effect of the network topology. Then, the impulsive noise generated by different electrical appliances is experimentally characterized at the source, and used to generate a model at the receiver. Stationary noise is finally investigated by both literature overview and experimental observations, and a simple model is provided. The models proposed in this deliverable will be used to support future studies on advanced signal processing techniques for PLC systems.

Keyword list

Power Line Communications, measurement campaign, channel characterization, channel modelling, channel transfer function, channel impulse response, impulsive noise, stationary noise

Executive Summary

Within the OMEGA project, WP3 is devoted to the study of future indoor Power Line Communication (PLC) systems, with a particular focus on high throughput transmission systems. In order to develop efficient PLC systems, and propose improvements to the existing technology, it is necessary to accurately characterise the electrical infrastructure.

This document presents the studies conducted within the OMEGA project on the characterization and modelling of the PLC channel. The main components of the PLC channel, namely the transfer function, the stationary noise and the impulsive noise, are fully characterized, based on both experimental studies and theoretical analysis. For each of these components, models are provided to be used for future system simulations.

The topic of PLC Channel Transfer Function (CTF) is first covered in details. A measurement campaign covering a frequency band up to 100 MHz is presented and the main time-frequency channel parameters are evaluated from this collection of experimental data. Statistical models are proposed for the PLC channel transfer function, following two complementary approaches. Firstly, an empirical model of the CTF is given to reflect the experimentally observed channel characteristics. Secondly, a model is presented in an analytical form, allowing for close form computation of the channel characteristic parameters. Finally, a model of the PLC CTF based on transmission line theory is provided, and the effect of Surge Protection Devices (SPD) on the PLC channel characteristics is investigated.

As a major impairment for PLC transmission, impulsive noise is then thoroughly investigated. Based on a measurement campaign of the noise generated by different electrical appliances, the impulsive noise is characterized at the source and classified into specific classes of noise. A model is provided to emulate the impulsive noise observed at the receiver.

Finally, a study of stationary noise linked to PLC networks is provided. After a state of the art, experimental measurements are presented, and a model is developed, as a composition of a coloured background noise and specific interference carriers.

The models proposed in this deliverable will be used as a starting point for the future WP3 studies on digital communications. In particular, the different proposals for advanced signal processing for PLC communications will be assessed through link level simulations. The proposed models will ensure that the simulations reflect operation in a realistic PLC environment.

List of Authors

First name	Last name	Beneficiary	Email address
Mohamed	TLICH	France Telecom	mohamed.tlich@orange-ftgroup.com
Pascal	PAGANI	France Telecom	pascal.pagani@orange-ftgroup.com
Gautier	AVRIL	France Telecom	
Frédéric	GAUTHIER	France Telecom	frederic.gauthier@orange-ftgroup.com
Ahmed	ZEDDAM	France Telecom	ahmed.zeddami@orange-ftgroup.com
Abdelkarim	KARTIT	Spidcom	Abdelkarim.Kartit@spidcom.com
Olivier	ISSON	Spidcom	Olivier.Isson@spidcom.com
Andrea	TONELLO	University Udine	tonello@uniud.it
Francesco	PECILE	University Udine	francesco.pecile@uniud.it
Salvatore	D'ALESSANDRO	University Udine	salvatore.dalessandro@uniud.it
Tao	ZHENG	University Udine	tao.zheng@uniud.it
Milena	BIONDI	University Udine	milena.biondi@uniud.it
Gordana	MIJIC	Thyia	gmijic@thyia.si
Klemen	KRIZNAR	Thyia	kkriznar@thyia.si
Jean-Yves	BAUDAIS	IETR	jean-yves.baudais@insa-rennes.fr
Ali	MAIGA	IETR	ali.maiga@insa-rennes.fr

Document History

Version	Date	Notes
V1.0	19/12/2008	Initial version
V1.1	10/07/2009	Addition of an annex on PLC channel measurement campaign, equation (18) modified.

List of Acronyms

Acronym	Meaning
CIR	Channel Impulse Response
CTF	Channel Transfer Function
DUT	Device Under Test
FCF	Frequency Correlation Function
ISI	Inter Symbol Interference
LISN	Line Impedance Stabilization Network
MSE	Mean Square Error
PDP	Power Delay Profile
PL	Path Loss
PLC	Power Line Communications
Rx	Receiver
Tx	Transmitter
VNA	Vector Network Analyser
WSSUS	Wide Sense Stationary Uncorrelated Scattering

Table of contents

1	Introduction.....	11
2	Channel Transfer Function Characterization.....	12
2.1	State of the Art.....	12
2.2	Channel Measurement Campaign	12
2.3	Time-Frequency Channel Characteristics.....	14
2.3.1	Wideband Propagation Parameters.....	14
2.3.1.1	Coherence Bandwidth.....	14
2.3.1.2	Time-Delay Parameters.....	14
2.3.2	Analysis of Results	15
2.3.2.1	Coherence Bandwidth Results	15
2.3.2.2	Time-Delay Parameters Results	18
2.3.2.3	Coherence Bandwidth versus RMS Delay Spread.....	20
3	Statistical Channel Transfer Function Modelling.....	22
3.1	General Observations and Channel Classification.....	22
3.2	Average Attenuation and Phase Modelling.....	24
3.2.1	Average Attenuation Modelling.....	24
3.2.2	Average Phase Modelling	26
3.3	Statistical Study of the Channel Frequency Fading	28
3.3.1	Peak and Notch Widths	29
3.3.2	Peak and Notch Heights.....	31
3.3.3	Peak and Notch Numbers	32
3.4	Channel Transfer Function Generator	34
3.4.1	PLC Magnitude Generator	34
3.4.1.1	Peaks and Notches Generation	34
3.4.1.2	Introduction of the Average Attenuation.....	35
3.4.2	PLC Phase Generator.....	37
3.4.2.1	Global Distortions Applied to the Linear Phases	37
3.4.2.2	Local Distortions Applied to the Linear Phases	38
3.5	Channel Impulse Response Generator	40
3.5.1	Regeneration of the Impulse Response.....	40
3.5.2	First Method: by Truncation	42
3.5.3	Second Method: Truncation by Windowing	42
3.5.4	Third Method: with the invfreqz MATLAB Function	43
3.5.5	Comparing the Proposed Methods	44
3.5.6	Conclusion	47
3.6	Simulation Results and Model Validation	47
4	Statistical Channel Transfer Function Model Software.....	49
5	Analytical Modelling of the Channel Transfer Function	52
5.1	Statistical Characterization	53
5.2	Channel Generation and Numerical Characterization.....	54
5.3	Matlab Code.....	60
6	Channel Transfer Function Model based on Transmission Line Theory.....	63
6.1	Introduction	63
6.2	Power Cable	63

6.3	Electrical Model of the Cable	63
6.3.1	Calculated Cable Parameters	65
6.4	Simulated Results	67
6.4.1	Transfer Function of the Cable Without and With Surge Protection Device (SPD)	68
6.4.2	Transfer Function of Typical Wiring	70
6.5	Conclusions	72
7	<i>Impulsive noise characterization and modelling</i>	73
7.1	State of the Art	73
7.2	Impulsive Noise Measurement Campaign	73
7.2.1	Measurement Description	73
7.2.2	Measurement Hardware	75
7.3	Impulsive Noise Characterization	75
7.3.1	General Observations	75
7.3.2	Noise Classification	80
7.3.2.1	Impulsive Noise Class 1	80
7.3.2.2	Impulsive Noise Class 2	80
7.3.2.3	Impulsive Noise Class 3	81
7.3.2.4	Impulsive Noise Class 4	81
7.3.2.5	Impulsive Noise Class 5	82
7.3.2.6	Impulsive Noise Class 6:	82
7.4	Impulsive Noise Modelling	83
7.4.1	Noise Modelling at Source	83
7.4.2	Impulsive Noise Modelling at the Receiver	84
7.4.2.1	Powerline Channel Model	85
7.4.2.2	Impulsive Noise at Receiver	85
7.4.2.3	Impulsive Noise Modelization by Electrical Device	87
7.4.2.4	Random Generator of Impulsive Noise at Receiver	89
8	<i>Stationary noise characterization and modelling</i>	90
8.1	State of the art	90
8.2	Stationary Noise Measurement Campaign	92
8.3	Stationary Noise Characterization	93
8.4	Stationary Noise Modelling	94
9	<i>Conclusion and Future Work</i>	97
10	<i>References</i>	98
11	<i>Annexes</i>	101
11.1	Additional information on PLC channel measurement campaign	101
11.2	Representative Noise Models at Source	103
11.2.1	Class 1 Model	103
11.2.2	Class 2 Model	104
11.2.2.1	Class 2-2 Noises	104
11.2.2.2	Class 2-1 Noises	105
11.2.3	Class 3 Model	106
11.2.4	Class 4 Model	107
11.2.5	Class 5 Model	108
11.2.6	Class 6 Model	110
11.2.6.1	Class 6-S Noises	110
11.2.6.2	Class 6-L noises	111

List of Tables

Table 1: Distribution of transfer functions by site	13
Table 2: Coherence bandwidth values in kHz for 0.5, 0.7 and 0.9 correlation levels for the curves of Figure 3.....	16
Table 3: Statistics of the coherence bandwidth function for 0.5, 0.7, and 0.9 correlation levels in kHz	17
Table 4: Statistics of time delay parameters in μ s.....	20
Table 5: Channel capacities calculation parameters.....	23
Table 6: Channel percentages and average capacities of classes	23
Table 7: Distribution of sites by class	24
Table 8: Average attenuation model by class	24
Table 9: Phase models and mean group delay values by class.	28
Table 10: Concavity depth C_c by class	38
Table 11: Phase shift signs probabilities	40
Table 12: MSE comparison of the three proposed methods ($M = 228$)	46
Table 13: MSE comparison of the three proposed methods ($M = 1213$)	47
Table 14: Model validation delay spread values	48
Table 15: List of devices and states generating by impulsive noise	74
Table 16: Amplitude and duration statistics of the class 1 impulsive noises.....	80
Table 17: Amplitude and duration statistics of the class 2-2 noises	81
Table 18: Amplitude and duration statistics of the class 2-1 noises	81
Table 19: Amplitude and duration statistics of the class 3 impulsive noises.....	81
Table 20: Amplitude and duration statistics of the class 4 impulsive noises.....	81
Table 21: Amplitude and duration statistics of the class 5 impulsive noises.....	82
Table 22: Amplitude and duration statistics of the class 6/S noises	83
Table 23: Amplitude and duration statistics of the class 6/L noises.....	83
Table 24: Duration and amplitude statistics by class	84
Table 25: Durations of the representative noises.....	84
Table 26: List of devices and states accompanied by impulsive noises	87
Table 27: Stationary noise measurements configuration	92
Table 28: Radio broadcasting frequency limits up to 100MHz.....	95
Table 29: Distribution of transfer functions by site	101
Table 30: Distribution of sites by class	101
Table 31: Repartition of the channel categories for each class	102
Table 32: Repartition of the channel c classes for each site.....	102

List of Figures

Figure 1: Power line channel measurement system.	13
Figure 2: An illustration of a typical power-delay profile and the definition of the delay parameters. ...	15
Figure 3: Frequency correlation functions of the measured channels - (i) good channel; (ii) mean channel; (iii) bad channel.....	16
Figure 4: Measured transfer function envelope of the maximum $B_{0,9}$ value.....	17
Figure 5: Measured transfer function envelope of the minimum $B_{0,9}$ value.....	18
Figure 6: Impulse response of Figure 4 channel.....	18
Figure 7: Impulse response of Figure 5 channel.....	19
Figure 8: Scatter plot of coherence bandwidth against RMS delay spread.	21
Figure 9: PLC channel measurements in a same site.	22
Figure 10: Channels and average attenuation model of class 6.	25
Figure 11: Channels and average attenuation model of class 2.	25
Figure 12: Gathered average attenuation models.....	26
Figure 13: Phases and average phase model of class 6.	26
Figure 14: Phases and average phase model of class 2.	27
Figure 15: Gathered average phase models.....	27
Figure 16: Specification of channel magnitude extrema.	29
Figure 17: Peak width definition.	29
Figure 18: Peak and notch widths distribution – same electrical circuit.....	30
Figure 19: Peak and notch widths distribution – different electrical circuits.....	30
Figure 20: Peak height definition.....	31
Figure 21: Peak and notch heights distribution – same electrical circuit.	32
Figure 22: Peak and notch heights distribution – different electrical circuits.	32
Figure 23: Number of peaks and notches distribution – same electrical circuit.	33
Figure 24: Number of peaks and notches distribution–different electrical circuits.	33
Figure 25: Lobe structure.	34
Figure 26: 1 st stage magnitude generation – same electrical circuit.....	35
Figure 27: 1 st stage magnitude generation – different electrical circuits.....	35
Figure 28: 2 nd stage magnitude generation – class 9.....	36
Figure 29: 2 nd stage magnitude generation – class 2.....	36
Figure 30: Histogram of the class 2 channel capacities distribution.	37
Figure 31: Concavity application to the linear phase.	38
Figure 32: Local distortions applied to the linear phase.....	39
Figure 33: Class 2 channel measured group delay.....	39
Figure 34: Class 9 channel measured group delay.....	40
Figure 35: Generated CTF.	41
Figure 36: Generated real-valued CIR.	41
Figure 37: Illustration of the truncation method.....	42
Figure 38: Illustration of the windowed truncation method.....	43
Figure 39: Illustration of the invfreqz function method.....	44
Figure 40: CTF comparison using the truncation method.....	45
Figure 41: CTF comparison using the windowed truncation method.....	45
Figure 42: CTF comparison using the invfreqz method.....	46
Figure 43: Magnitude and Phase generation – class 2.....	47
Figure 44: Magnitude and Phase generation – class 9.....	48
Figure 45: WITS workspace creation and definition.....	49
Figure 46: WITS general interface view.	50
Figure 47: WITS exporting options.....	50
Figure 48: Realization of a PLC channel impulse response and frequency response.	56
Figure 49: PDF of the frequency response amplitude for a given frequency f_0	56
Figure 50: CDF of the frequency response amplitude for a given frequency f_0	56
Figure 51: PDF of the frequency response square amplitude for a given frequency f_0	57
Figure 52: CDF of the frequency response square amplitude for a given frequency f_0	57
Figure 53: Theoretical and simulated expected path loss.....	57
Figure 54: PDF of the channel energy.	58
Figure 55: CDF of the channel energy.....	58
Figure 56: PDF of the impulse response amplitude for a given time instant t_0	58

Figure 57: CDF of the impulse response amplitude for a given time instant t_0	59
Figure 58: PDF of the impulse response square amplitude for a given time instant t_0	59
Figure 59: CDF of the impulse response square amplitude for a given time instant t_0	59
Figure 60: PDF of the delay spread	60
Figure 61: CDF of the delay spread	60
Figure 62: Normalized delay spread and channel energy for one hundred channel realizations.	60
Figure 63: Evaluated cable	63
Figure 64: Evaluated cable	64
Figure 65: Cable model	64
Figure 66: Wire resistance per unit length	65
Figure 67: Self inductance of a wire per unit length	66
Figure 68: Mutual inductance between wires 1 and 2 per unit length	66
Figure 69: Capacitance between two wires per unit length	67
Figure 70: Conductance between two wires per unit length	67
Figure 71: ADS 2008 computer software model	68
Figure 72: Cable with surge protection devices and PLC modems	68
Figure 73: Amplitude response of 1 m cable without surge protection devices	69
Figure 74: Amplitude response of 1 m cable with surge protection devices	69
Figure 75: Amplitude response of 10 m cable without surge protection devices	70
Figure 76: Amplitude response of 1 m cable with surge protection devices	70
Figure 77: Wiring model	71
Figure 78: Amplitude response of the wiring without and with surge protection device	71
Figure 79: Measurement hardware of impulsive noise at source	75
Figure 80: Turning Off event impulsive noises for different devices:	76
Figure 81: Washing machine turning On event	77
Figure 82: Can opener tuning On event	77
Figure 83: Flat TV turning On event	77
Figure 84: Iron thermostat On event	78
Figure 85: Refrigerator door closing event	78
Figure 86: Coffee maker turning On event	78
Figure 87: Electrical heating thermostat Off event	79
Figure 88: Laptop plug plugging event	79
Figure 89: Laptop plug unplugging event	79
Figure 90: Fluorescent lamp turning on event	82
Figure 91: Residential Gateway IP Phone pick up event	83
Figure 92: Impulsive noise at receiver – general model	84
Figure 93: Class 2 and Class 9 magnitude examples	85
Figure 94: Impulsive noise after class 9 and class 2 channels – time domain representation.	86
Figure 95: Impulsive noise after class 9 and class 2 channels – frequency domain representation. ...	86
Figure 96: Hair dryer high to soft event	89
Figure 97: Background noise PSD in dBm/Hz. (a) in Finland [46], (b) in Canada [3]	91
Figure 98: Stationary noise measuring hardware	92
Figure 99: measured stationary noise	93
Figure 100: Stationary noise levels from [54]	94
Figure 101: Stationary noise model - $\frac{1}{f^2}$ decreasing shape	96
Figure 103: Mean case – Refrigerator opening door event – 0.3 ms	103
Figure 104: Short case – vacuum cleaner turning On event – 0.003 ms	103
Figure 105: Long case – Iron thermostat On event – 3.1 ms	104
Figure 106: Mean case – Electrical heating thermostat Off event – 4.12 ms.	104
Figure 107: Short case – Paint burner Off event – 1.44 ms	105
Figure 108: Long case – Paint burner Off event – 8.6 ms	105
Figure 109: Mean case – Fluorescent lamp Off event – 1.8 ms	105
Figure 110: Short case – Refrigerator door closing event – 0.16 ms	106
Figure 111: Long case – Fluorescent lamp Of event – 3.1 ms	106
Figure 112: Mean case – Vacuum cleaner plug plugging event – 2 ms	106
Figure 113: Short case – Vacuum cleaner plug plugging event – 0.006 ms	107
Figure 114: Long case – Vacuum cleaner plug plugging event – 6.8 ms	107
Figure 115: Mean case – Laptop power adapter plug unplugging event – 0.52 ms	107
Figure 116: Short case – Laptop power adapter plug unplugging event – 0.012 ms	108
Figure 117: Long case – Laptop power adapter plug unplugging event – 0.73 ms	108

Figure 118: Mean case – Can opener On event – 26 ms.	108
Figure 119: Short case – Fluorescent lamp On event – 18 ms.	109
Figure 120: Long case – Can opener On event – 36 ms.	109
Figure 121: Mean case – Residential Gateway IP Phone pick up event – 0.17 ms.	110
Figure 122: Short case – Induction Hob On event – 0.01 ms.	110
Figure 123: Long case – Residential Gateway IP Phone pick up – 0.29 ms.	111
Figure 124: Mean (=short) case – Flat TV On event – 12 ms.	111
Figure 125: Long case – Laptop On event – 48 ms.	111

1 Introduction

Within the OMEGA project, WP3 is devoted to the study of future indoor Power Line Communication (PLC) systems, with a particular focus on high throughput transmission systems. The PLC technology uses the classical electrical network to perform data transmission. As a result it represents an effective way to build home network connectivity without the need for additional cable infrastructure. The powerline medium, however, is a challenging environment for high throughput data communication. First, transmission over tens of meters of copper lines lead to a strong attenuation, and the particular network topology generates multiple propagation paths that yield to frequency selective fading. In addition, the different types of electrical noise observed on the powerline medium lead to data corruption. Finally, the channel characteristics may vary from one segment of the network to the other, and fluctuate in time depending on the different domestic appliance connected to the medium.

In order to develop efficient PLC systems, and propose improvements to the existing technology, it is necessary to accurately characterise the electrical infrastructure. The characteristics of the Channel Transfer Function (CTF) and of the stationary noise give an indication of the PLC channel capacity, and allow to evaluate the PLC systems performance in a realistic environment. The knowledge of additional electromagnetic perturbations, such as impulsive noise, allow to understand the intrinsic impairments of the PLC channel and develop efficient protection methods.

In this context, this OMEGA deliverable presents a complete study of the indoor PLC channel. The main components of the PLC channel, namely the transfer function, the stationary noise and the impulsive noise, are fully characterized, based on both experimental studies and theoretical analysis. For each of these components, models are provided to be used for future system simulations.

Section 2 presents a statistical study of the CTF characteristics, based on a large collection of experimental data, on a bandwidth extending to 100 MHz. The channel measurement campaign is first presented, and the time-frequency characteristics of the PLC channel are studied, with a particular emphasis on the delay spread and the coherence bandwidth.

In Section 3, a statistical model of the PLC CTF is proposed. The channel observations are classified into 9 classes with increasing channel capacity. A model for each class is proposed in the frequency domain, accounting for the average phase and magnitude decay, and for the statistical behaviour due to frequency fading. Methods for generating tractable time domain Channel Impulse Responses are also provided. A model generation software has been developed for the use of the proposed model in the OMEGA project (Section 4).

Section 5 presents an analytical model of the PLC channel, based on the theoretical description of the CIR. Statistical parameters are introduced to render the effect of different electrical network topologies. The model parameters can be optimized to fit the characteristic channel parameters, such as delay spread, to measurements observations.

A model of the CTF based on transmission line theory is presented in Section 6. From the properties of the powerline cables, the CTF of a complete electrical network is evaluated. The effect of Surge Protection Devices (SPD) on the PLC channel characteristics is investigated.

Section 7 is devoted to the characterization and modelling of impulsive noise. Based on a measurement campaign of the noise generated by different electrical appliances, the impulsive noise is characterized at the source and classified into specific classes of noise. A model is provided to emulate the impulsive noise observed at the receiver.

Finally Section 8 gives a study of stationary noise linked to PLC networks. After a state of the art, experimental measurements are presented, and a model is developed, as a composition of a coloured background noise and specific interference carriers.

2 Channel Transfer Function Characterization

2.1 State of the Art

The PLC channel is characterized by several differences from other wired media, as its interference and noise levels are much larger. An accurate understanding of the complete characteristics of the broadband PLC channel is important [1] when developing PLC transmission chains [2] and simulating the performance of advanced communication technologies [3][4]. A PLC channel model is, in this case, very important to set up.

Several approaches have been followed for characterizing the PLC channel [5][6][7][8]. An interesting approach describes the PLC by its multipath behaviour [6][7]. There has also been attempts to model the PLC as a two-conductor transmission line [8] or as a three-conductor transmission line [9][10]. These approaches share a common deficiency in that they are only able to partially describe the underlying physics of powerline signal propagation and, therefore, do not allow the unveiling of general properties or any embedded determinism of the PLC channel. Moreover, the multipath echo-model approach is based on a parametric model where the many parameters can be estimated only after having measured the PLC Channel Impulse Response (CIR), thus limiting the capability of a priori channel modelling.

Some deterministic models have also been proposed in the literature. Deterministic model basically means finding the Channel Transfer Function (CTF) theoretically without taking actual measurements of the transmission line. In [11], authors use chain matrix theory to represent the complex multipath network. The developed deterministic model is incomplete in some extent because of the unavailability of neither the impedances values of the ends of branches nor their time variability information.

Extensive characterizations of powerline channels have been reported in [7][12][13][14]. These studies are mainly focused on frequencies up to 30 MHz.

The coherence bandwidth is a key parameter for the PLC transmission channel. Its value, relatively to the bandwidth of the transmitted signal, subsequently determines the need for employing channel protection techniques, e.g. equalisation or coding, to overcome the dispersive effects of multipath [15][16]. The CIR of transmission channels can be characterised by various parameters. The average delay is derived from the first moment of the delay power spectrum and it is a measure of the mean delay of signals. The delay spread is derived from the second moment of the delay power spectrum and describes the dispersion in the time domain due to multipath transmission.

For PLC channels, and for the 1-30 MHz frequency band, thorough studies were undertaken in [12][13]. It was observed that 99% of the studied channels have an RMS delay spread below $0.5\mu\text{s}$. In [12], the coherence bandwidth at 0.9 correlation level, $B_{0.9}$, was observed to have an average value of 1 MHz.

Furthermore, in [14], it was indicated that for signals in the 0.5-15 MHz frequency band, the maximum excess delay was below $3\mu\text{s}$, and the minimum estimated value of $B_{0.9}$ was 25 KHz.

In [7] and for the frequency range up to 30 MHz, it has been found that, for 95 % of the measured channels the mean-delay spread is between 160ns and $3.2\mu\text{s}$. 95 % of the channels exhibit a delay spread between 240ns and $2.5\mu\text{s}$.

2.2 Channel Measurement Campaign

The proposed PLC channel model is proposed over a frequency band ranging up to the 100 MHz. For this purpose wideband propagation measurements were undertaken in the 30 KHz – 100 MHz band in various indoor channel environments (country and urban, new and old buildings, apartments and houses) as shown in Table 1.

Site number	Site information	Number of transfer functions
1	House - Urban	19
2	New house - Urban	13
3	Recently restored apartment – Urban	12
4	Recent house – Urban	28
5	Recent house – Urban	34
6	Recent house – country	22
7	Old House - country	16

Table 1: Distribution of transfer functions by site

The PLC CTF study presented here relates to seven measurement sites and a total of 144 transfer functions. For each site, the transfer functions are measured between a principal outlet (most probable to receive a PLC module) and all other outlets in the home (except improbable outlets such as refrigerator ones...). More information is given about measurements distribution in Annex 11.1.

CTF measurements were carried out in the frequency domain, by means of a Vector Network Analyser (VNA), as shown in the block diagram of Figure 1.

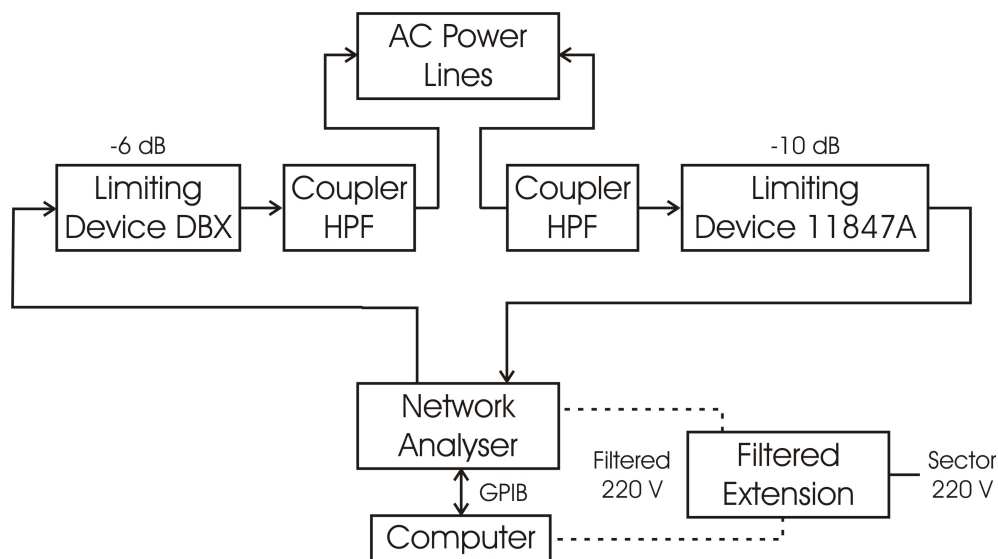


Figure 1: Power line channel measurement system.

The coupler box plugged in the AC wall outlet behaves like a high-pass filter, with the 3 dB cutoff at 30 KHz. The probing signal passes through the coupler and the AC power line network and exits through a similar coupler plugged in a different outlet. A direct coupler to coupler connection is used to calibrate the test setup.

Two over-voltage limiting devices with -10 dB and -6 dB losses, respectively, are used in front of the entry port of the VNA 8753ES and its exit port, which can serve as an entry port, to protect it from over-voltages produced by the impulsive noises of the AC powerline.

A computer is connected to the VNA through a GPIB bus. This allows the computer to record data and control the VNA using the INTUILINK software [21].

The VNA and the computer are isolated from the powerline network using a filtered extension. This extension is systematically connected to an outlet not likely to be connected to a PLC modem, such as washing machine outlet. These precautions are taken in order to minimize the influence of the measurement devices on the measured transfer functions.

2.3 Time-Frequency Channel Characteristics

The measurements obtained using a swept frequency channel sounder (Figure 1) yielded sufficient statistical data from which frequency correlation functions were derived. These results were used to obtain the coherence bandwidth of the PLC channels investigated. The CIR were obtained by applying the inverse Fourier transform to the estimated frequency response [16].

Here, a comparison between coherence bandwidth and time-delay parameters estimated in both frequency bands 30 KHz - 100 MHz and 2 MHz - 100 MHz is elaborated. Results are intended for applications in high-capacity indoor powerline networks. The investigation is aimed to show that the PLC channel studies in a band starting from a frequency lower than 2 MHz distorts the real values that an implementer should take, as the PLC modem only operates in the frequencies above 2 MHz.

2.3.1 Wideband Propagation Parameters

Characterisation of wideband channel performance subject to multipath can be usefully described using the coherence bandwidth and delay spread parameters.

2.3.1.1 Coherence Bandwidth

The frequency-selective behaviour of the channel can be described in terms of the auto-correlation function for a Wide Sense Stationary Uncorrelated Scattering (WSSUS) channel¹. Equation (1) gives $R(\Delta f)$, the Frequency Correlation Function (FCF):

$$(1) \quad R(\Delta f) = \int_{-\infty}^{+\infty} H(f)H^*(f + \Delta f)df$$

where $H(f)$ is the CTF, Δf is the frequency shift and $*$ denotes the complex conjugate. $R(\Delta f)$ is a measure of the magnitude of correlation between the channel response at two spaced frequencies. The coherence bandwidth is a statistical measure of the range of frequencies over which the FCF can be considered 'flat' (i.e. a channel passes all spectral components with approximately equal gain and linear phase).

In other words, coherence bandwidth is the range of frequencies over which two frequency components have a strong potential for amplitude correlation. It is a frequency-domain parameter that is useful for assessing the performances of various modulation techniques [22]. No single definitive value of correlation has emerged for the specification of coherence bandwidth. Hence, coherence bandwidths for generally accepted values of correlations coefficient equal to 0.5, 0.7 and 0.9 were evaluated from each FCF, and these are referred to as $B_{0.5}$, $B_{0.7}$ and $B_{0.9}$, respectively.

2.3.1.2 Time-Delay Parameters

Random and complicated PLC propagation channels can be characterized using the impulse response approach. Here, the channel is a linear filter with impulse response $h(t)$. The Power-Delay Profile (PDP) provides an indication of the dispersion or distribution of transmitted power over various paths in a multipath model for propagation. The PDP of the channel is calculated by taking the spatial average of $|h(t)|^2$. It can be thought of as a density function, of the form:

¹ As a first approximation, the PLC channel is considered WSSUS here, as is also assumed for outdoor PLC channels in [17], [18]. For further study on this topic, a thorough discussion about the validation of the WSSUS assumption for experimental measurements is given in [19]. In particular, the RUN method is based on assessments of the process variance over successive sub-intervals [20].

$$(2) \quad P(\tau) = \frac{|h(\tau)|^2}{\int_{-\infty}^{+\infty} |h(\tau)|^2 d\tau}$$

The RMS delay spread is the square root of the second central moment of a power-delay profile. It is the standard deviation about the mean excess delay, and is expressed as:

$$(3) \quad \tau_{RMS} = \left[\int (\tau - \tau_e - \tau_A)^2 P(\tau) d\tau \right]^{1/2}$$

where τ_A is the first-arrival delay, a time delay corresponding to the arrival of the first transmitted signal at the receiver; and τ_e is the mean excess delay, the first moment of the power-delay profile with respect to the first arrival delay:

$$(4) \quad \tau_e = \int (\tau - \tau_A) P(\tau) d\tau$$

The RMS delay spread is a good measure of the multipath spread. It gives an indication of the nature of the inter-symbol interference (ISI). Strong echoes (relative to the shortest path) with long delays contribute significantly to τ_{RMS} .

A fourth time-delay parameter is the maximum excess delay (τ_m). This is measured with respect to a specific power level, which is characterized as the threshold of the signal. When the signal level is lower than the threshold, it is processed as noise. For example, the maximum excess delay spread can be specified as the excess delay (τ_m) for which $P(\tau)$ falls below -30 dB with respect to its peak value, as shown in Figure 2.

A typical plot of the time delay parameters is presented in Figure 2.

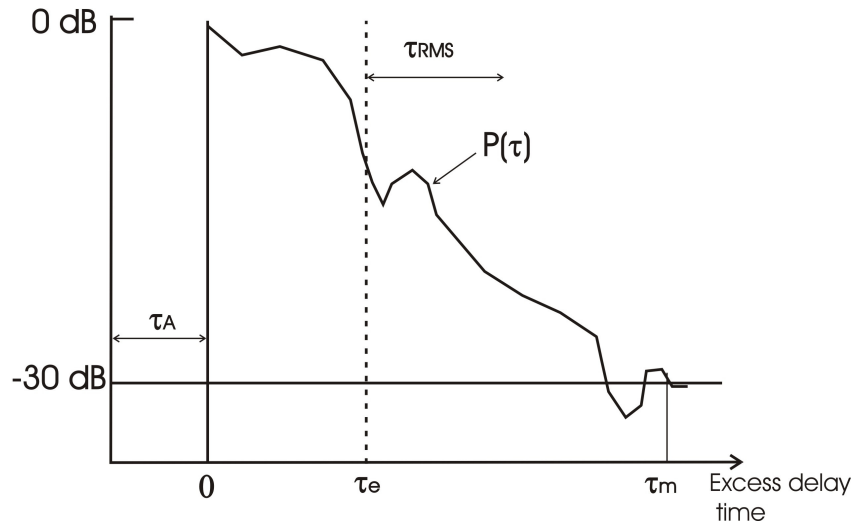


Figure 2: An illustration of a typical power-delay profile and the definition of the delay parameters.

2.3.2 Analysis of Results

In this section, an analysis of the measured results, estimation of coherence bandwidth, its variability and interrelationship with RMS delay spread, and analysis of time-delay spread parameters are outlined for the both frequency bands 30 KHz – 100 MHz and 2 MHz – 100 MHz referred to as FB₁ and FB₂, respectively.

2.3.2.1 Coherence Bandwidth Results

For the both frequency bands, Figure 3 shows the frequency FCF obtained for three transmitter receiver scenarios: a good channel (curves (i)), which can be assumed to have the least multipath contributions. Curves (ii) and (iii) correspond to the FCF obtained from a mean-case and bad channels, respectively.

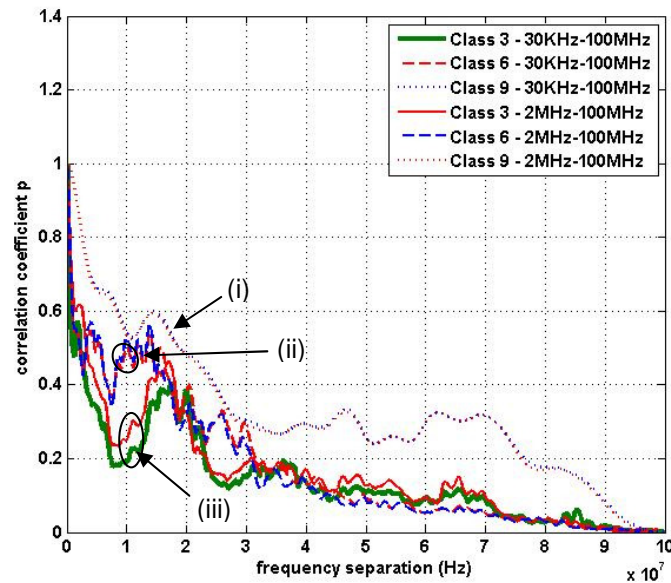


Figure 3: Frequency correlation functions of the measured channels - (i) good channel; (ii) mean channel; (iii) bad channel.

The degradation of the FCF corresponding to mean-case and bad channels with respect to the good channel can be seen in Figure 3. Rapid decrease of the frequency correlation function with respect to the frequency separation and also as the channel is bad can be observed. The decrease in frequency correlation function is not monotonic, and this is due to the presence of multipath echoes in the PLC channel.

Concerning frequency bands comparison, a first result can be already released: the FCF associated to each frequency band are juxtaposed for the good and mean-case channels (dotted lines and dashed lines curves respectively). Nevertheless, a significant difference tags the bad-case channel (bold lines curves).

From the shape of the FCF, an estimation of the coherence bandwidth corresponding to a correlation coefficient of 0.5 can be obtained. In Figure 3, this is almost 2.1 MHz for curves (ii) and 18.8 MHz for curves (iii). In general, the smallest frequency separation value is normally chosen to estimate the coherence bandwidth. This is in agreement with observations made in [23] that coherence bandwidth characterisation using spaced tones [22] is not satisfactory unless measurements are taken over a large number of points.

Coherence bandwidth values for 0.5, 0.7 and 0.9 correlation levels for the curves of Figure 3 are given in Table 2, and statistics of the coherence bandwidth function for 0.5, 0.7 and 0.9 correlation levels for all channel measurements are shown in

Table 3.

Curve	$B_{0.5} (FB_1/FB_2)$, kHz	$B_{0.7} (FB_1/FB_2)$, kHz	$B_{0.9} (FB_1/FB_2)$, kHz
(i)	18 819.5 / 18 760.5	3 852.5 / 3 725.5	1 586.5 / 1 587.5
(ii)	2 171.5 / 2 138.5	586.5 / 602.5	249.5 / 267.5
(iii)	909.5 / 3 214.5	347.5 / 720.5	50.5 / 243.5

Table 2: Coherence bandwidth values in kHz for 0.5, 0.7 and 0.9 correlation levels for the curves of Figure 3

	Min	Max	Mean	Std	90% above	90% below
$B_{0.5} (FB_1)$	230.5	33 850.5	4 539.3	6 544.7	423.5	13 376.5
$B_{0.5} (FB_2)$	152.5	33 695.5	4 801.6	6 058.7	387.5	13 286.5
$B_{0.7} (FB_1)$	98.5	8 054.5	833.9	1 063.2	181.5	1 774.5
$B_{0.7} (FB_2)$	97.5	7 948.5	876.94	1 033	232.5	1 820.5
$B_{0.9} (FB_1)$	32.5	1 859.5	291.97	334.36	65.5	691.5
$B_{0.9} (FB_2)$	43.5	1 899.5	310.1	330.03	89.5	714.5

Table 3: Statistics of the coherence bandwidth function for 0.5, 0.7, and 0.9 correlation levels in kHz

For the 0.9 coherence level and the frequency band FB_1 , the coherence bandwidth was observed to have a mean of 291.97 kHz, minimum coherence bandwidth of 32.5 kHz, and 334.36 KHz standard deviation (Std). For 90% of the time, the value of $B_{0.9}$ obtained was below 691.5 kHz and above 65.5 kHz. If we focus on the frequency band FB_2 values, we see that they are greater than the FB_1 values. The minimum coherence bandwidth becomes 43.5 kHz, and 90% of the PLC channels have $B_{0.9}$ values greater than 89.5 kHz.

For the 0.7 coherence level and the frequency band FB_1 , a mean coherence bandwidth of 833.9 kHz was obtained. Here, the minimum value emerged as 98.5 kHz and the standard deviation as 1.063 MHz. The FB_2 values are very close to the FB_1 ones.

In the 0.5 coherence level, 80% of the channel measurements have a $B_{0.5}$ values below 13.376 MHz and above 423.5 kHz. Like the 0.9 and 0.7 coherence levels, the FB_2 mean value of $B_{0.5}$ (4.801 MHz) is greater than the FB_1 one (4.539 MHz). But, the min and max values are lower in the FB_2 case.

To investigate the reasons for the fluctuations of the coherence bandwidth values, magnitude curves of the complex frequency responses are shown. Figure 4 represents the channel frequency response for the case where the coherence bandwidth was estimated at 1.859 MHz in FB_1 (max value). Figure 4 clearly shows that the channel frequency response presents few notches, large peaks, and is relatively flat over the 100 MHz bandwidth. Not surprisingly therefore, the coherence bandwidth assumed a relatively high value.

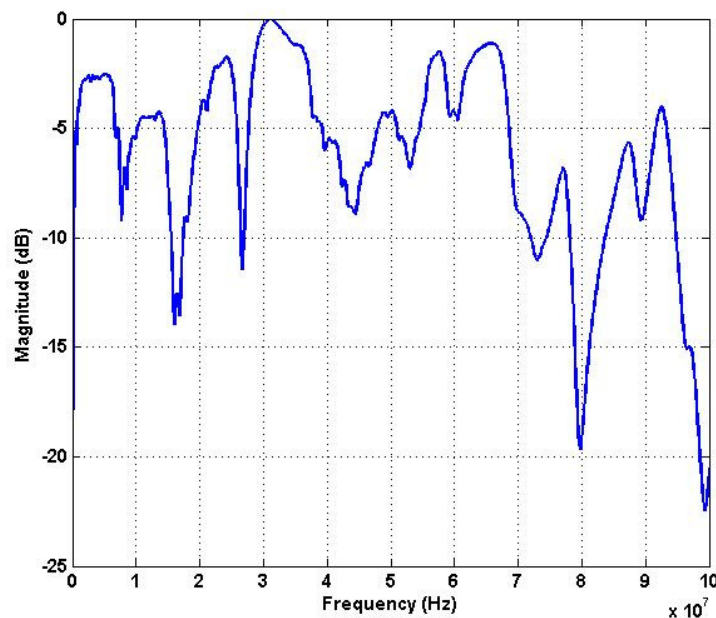


Figure 4: Measured transfer function envelope of the maximum $B_{0.9}$ value.

Next, the least value of the coherence bandwidth (32.5 KHz) in FB_1 was investigated. Figure 5 shows the magnitude response in this case which shows significant frequency selective fading of the channel, resulting in

deep fades at several frequencies and narrow peaks. The presence of this significant frequency selective fading explains the relatively small value of coherence bandwidth observed. Both of these cases demonstrate that the PLC indoor channel is considerably affected by multipath, and that the coherence bandwidth value decreases with frequency selective fading.

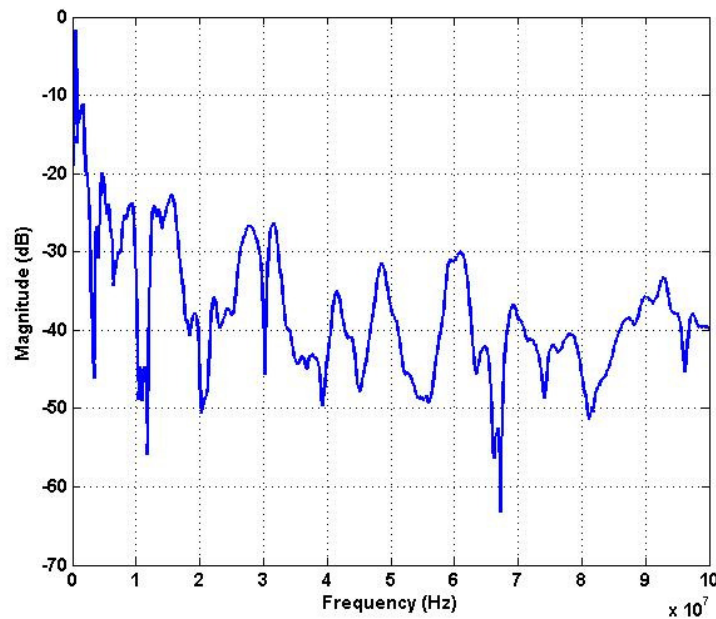


Figure 5: Measured transfer function envelope of the minimum $B_{0,9}$ value.

2.3.2.2 Time-Delay Parameters Results

By means of an inverse Fourier transform the impulsive response $h(t)$ can be derived from the absolute value and the phase of a measured transfer function. For the frequency bands 30 KHz – 100 MHz (FB_1) and 2 MHz – 100 MHz (FB_2), the amplitudes of the impulse responses of the channels of Figure 4 and Figure 5 are depicted in Figure 6 and Figure 7, respectively.

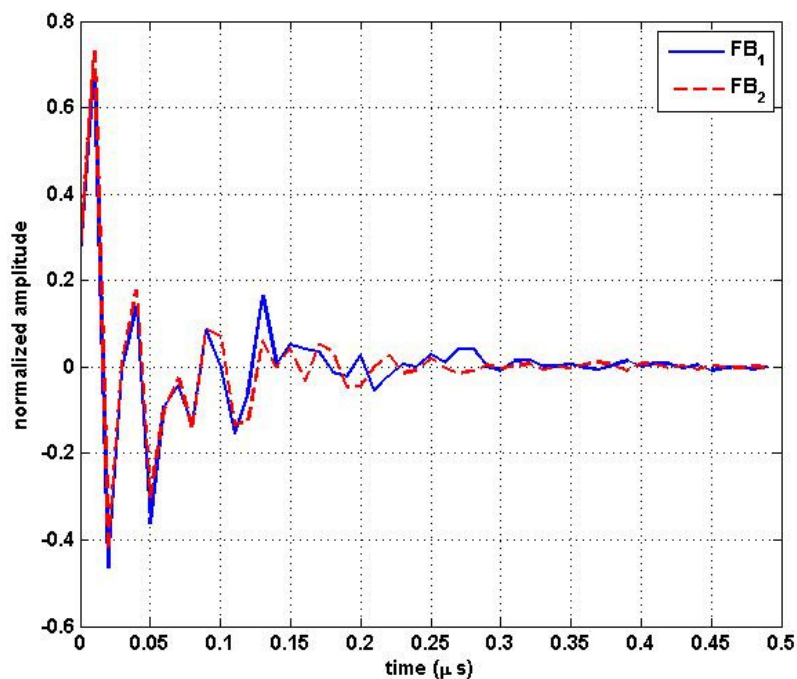


Figure 6: Impulse response of **Figure 4** channel.

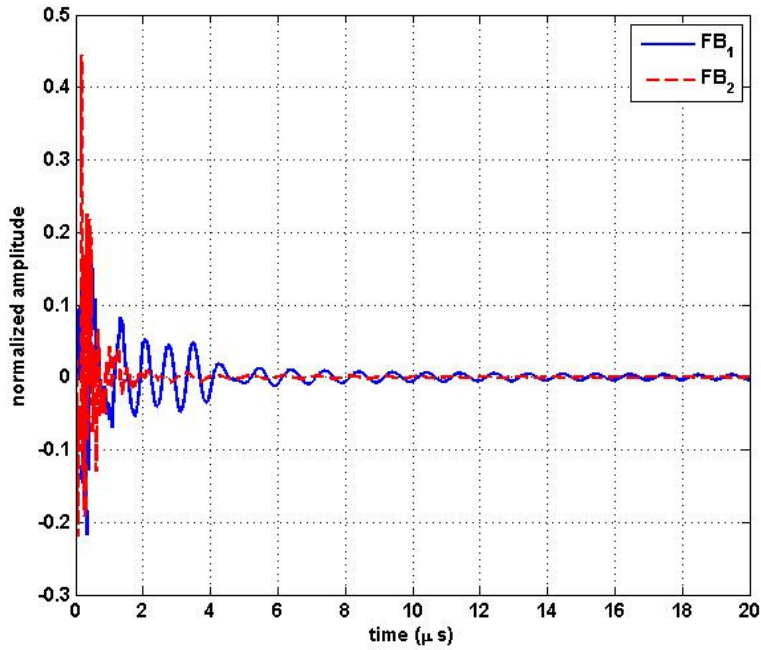


Figure 7: Impulse response of **Figure 5** channel.

As the maximum excess delay (τ_m) is specified as the excess delay for which $P(\tau)$ falls below -30 dB with respect to its peak value, the lower signal levels are processed as noise. Consequently, it is more suitable to calculate the mean excess delay (τ_e) and the RMS delay spread (τ_{RMS}) on the basis of channel time coefficients lower than τ_m .

The CIR of Figure 6 and Figure 7 show some peaks which confirm the multipath characteristics of PLC channels. For the frequency band FB1, the CIR of Figure 6 exhibits a maximum peak at a delay $\tau_A = 0.01\mu s$, a mean excess delay $\tau_e = 0.0187\mu s$, an RMS delay spread $\tau_{RMS} = 0.0368\mu s$, and a maximum excess delay $\tau_m = 0.28\mu s$ for which $P(\tau)$ falls below -30 dB with respect to its peak value.

The same parameters of the CIR of Figure 7 are $\tau_A = 0.32\mu s$, $\tau_e = 0.9521\mu s$, $\tau_{RMS} = 1.3674\mu s$, and $\tau_m = 9.41\mu s$. This is quite foreseeable as the CIR of Figure 6 is associated to a shorter PLC channel and much less affected by multipath.

More interesting are the reduced delays of the CIR of Figure 6 and Figure 7 when the frequency band FB2 is considered. Mean excess delay, RMS delay spread, and maximum excess delay parameters become $\tau_e = 0.0145\mu s$, $\tau_{RMS} = 0.031\mu s$, and $\tau_m = 0.22\mu s$ for the CIR in Figure 6. For the CIR in Figure 7, the effect is more undeniable. In fact, time delay parameters fall spectacularly until $\tau_A = 0.17\mu s$, $\tau_e = 0.13\mu s$, $\tau_{RMS} = 0.228\mu s$, and $\tau_m = 1.6\mu s$.

Statistics of time-delay spread parameters for all measured PLC channels are given in Table 4.

	Min	Max	Mean	Std	90% above	90% below
$\tau_A (FB_1)$, μs	0.01	0.55	0.1751	0.1134	0.05	0.31
$\tau_A (FB_2)$, μs	0.01	0.41	0.1523	0.0967	0.05	0.30
$\tau_e (FB_1)$, μs	0.001	0.9521	0.2584	0.2364	0.0339	0.6352
$\tau_e (FB_2)$, μs	0.0003	0.8822	0.1821	0.1567	0.0253	0.3559
$\tau_{RMS} (FB_1)$, μs	0.027	1.367	0.413	0.294	0.066	0.784
$\tau_{RMS} (FB_2)$, μs	0.026	1.039	0.309	0.212	0.067	0.601
$\tau_m (FB_1)$, μs	0.26	10.93	3.18	2.21	0.6	6.45
$\tau_m (FB_2)$, μs	0.18	6.26	2.228	1.327	0.55	3.81

Table 4: Statistics of time delay parameters in μs .

In the frequency band FB_1 , the first-arrival delay (τ_A) was observed to have a mean of $0.17\mu\text{s}$, minimum of $0.01\mu\text{s}$, and $0.11\mu\text{s}$ standard deviation. For 90% of the time, the value of τ_A obtained was below $0.31\mu\text{s}$ and above $0.05\mu\text{s}$. Comparing to the frequency band FB_2 case, there is not a great difference to note for this parameter.

For the mean-excess delay parameter and the FB_1 case, a mean value of $0.25\mu\text{s}$ was obtained. Here, the minimum value emerged as 1ns and the standard deviation as $0.23\mu\text{s}$. Concerning the maximum-excess delay, 80% of the channel measurements have values of τ_m between $0.6\mu\text{s}$ and $6.45\mu\text{s}$. 80 % of the channels exhibit an RMS delay spread between $0.06\mu\text{s}$ and $0.78\mu\text{s}$. The measured channels have a mean RMS delay spread of $0.413\mu\text{s}$.

The passage to FB_2 induced an important reduction of the maximum excess delay, whose min, max, mean, and standard deviation values were almost divided by 2.

2.3.2.3 Coherence Bandwidth versus RMS Delay Spread

Figure 8 shows a scatter plot of the RMS delay spread against the coherence bandwidth of the PLC channel measures for the two frequency bands FB_1 and FB_2 . The scatter plot shows a high concentration of points in the range $0.1\mu\text{s}$ - $0.9\mu\text{s}$ at which the coherence bandwidth is almost under 500 kHz and over 50kHz. Higher values of coherence bandwidth are observed for RMS delay spread values less than $0.1\mu\text{s}$. In system design terms, higher coherence bandwidth translates to faster symbol transmission rates [22].

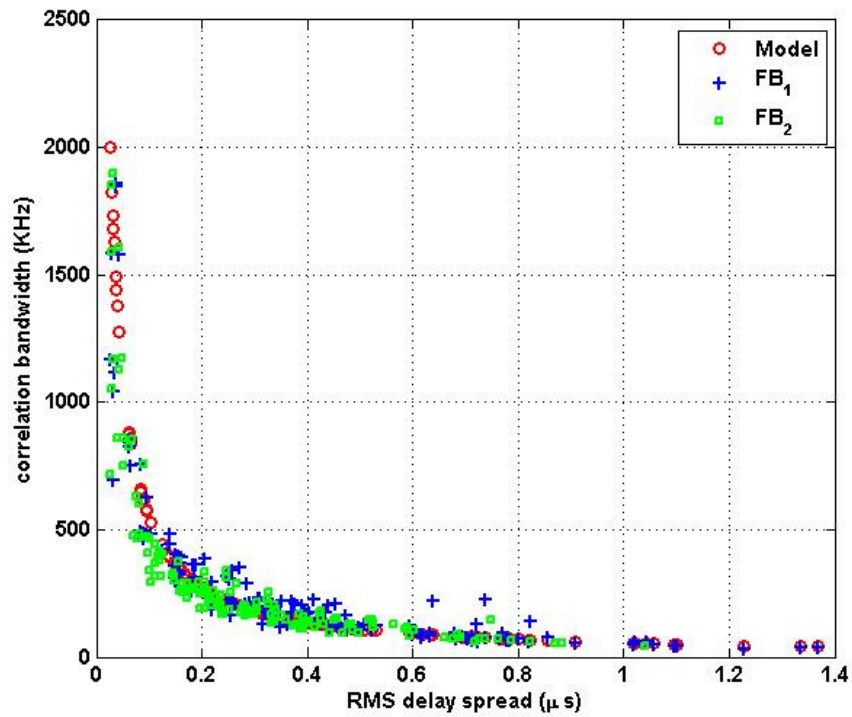


Figure 8: Scatter plot of coherence bandwidth against RMS delay spread.

For both frequency bands, Figure 8 depicts a same and clear relation between the values of $B_{0.9}$ and τ_{RMS} estimated in the overall set of measured channels, and which can be approximated by:

$$(5) \quad \tau_{RMS}(\mu s) = \frac{55}{B_{0.9}(KHz)}$$

On Figure 8, the relation (5) is represented by the red-circles curve.

3 Statistical Channel Transfer Function Modelling

As explained in Section 2.1, the unavailability of a model that fully describes signal propagation along powerline cables led the powerline community to often reach overly pessimistic conclusions: the PLC is impossible to model a priori [24].

An a priori approach to the characterization of the PLC channel based on CTF classification and thorough statistical study of their fading properties was described in [25] and [26] and further improved in this Section.

3.1 General Observations and Channel Classification

If we observe the measurement results of the PLC channel transfer functions by site, we can distinguish two categories of channels:

- PLC CTF where the transmitter (Tx) and receiver (Rx) outlets pertain to the same electrical circuit, i.e. are situated in series on the same branch corresponding to one fuse in the electrical box
- PLC CTF where the Tx and Rx outlets pertain to two different electrical circuits, i.e. are situated on different branches of the electrical box.

For each category and site, the PLC CTF are almost identical and are independent of their outlets location (peaks and notches almost at the same frequencies).

On Figure 9 are reported the CTF measurements in a same site. The top curves are associated to the same electrical circuit case, and the bottom curves to the different electrical circuits case.

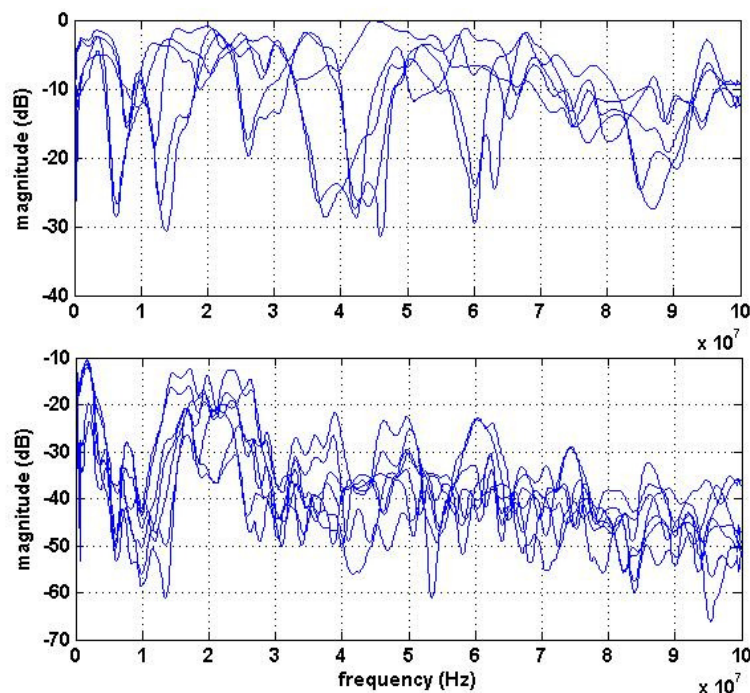


Figure 9: PLC channel measurements in a same site.

This observation leads to the idea to classify measured PLC channels according to their potential transmission performance. Because calculating distances separating transmitters from receivers was impossible, PLC channels were classified into several classes per ascending order of their capacities (according to the Shannon's capacity formula and for a same reference noise and PSD emission mask). The transfer functions of class 1 are those which convey the lowest data rate, the transfer functions of class 2 are those which convey rates higher than those of class 1, etc.

To carry out this classification, we started by calculating for each measured channel (with CTF H) its capacity in the presence of a white noise. The calculation parameters are described in Table 5, and the capacity (C) formula is described in Equation (6).

$$(6) \quad C = \Delta f \cdot \sum_{i=1}^N \log_2 \left(1 + \frac{P_e \cdot |H(f_i)|^2}{P_b} \right) \quad (\text{bits/s})$$

Frequency bands:	1MHz - 100 MHz
Carrier width (Δf):	25 KHz
Number of Carriers (N):	3960
Transmitted PSD (P_e):	-50 dBm/Hz
White noise PSD (P_b):	-140 dBm/Hz

Table 5: Channel capacities calculation parameters

In the 1MHz - 100 MHz frequency band, the minimum capacity was about 1 Gbps and the maximum capacity about 2.8 Gbps. Nine classes are thus defined with a constant interval of 200 Mbps. The first class comprises the channels with capacities ranging between 1 Gbps and 1.2 Gbps, and the ninth class consists of channels with capacities between 2.6 Gbps and 2.8Gbps. With the enrichment of the channel data base, new transfer functions with capacities lower than 1Gbits/s or higher than 2.8Gbits/s could constitute new classes.

The classification results, in terms of measured transfer function percentage, capacity interval, and average capacity distributions, are presented in Table 6. We can observe that, for the considered reference white noise and the 1 MHz-100 MHz frequency band, the average capacities vary between 1120 Mbps for class 1 and 2699 Mbps for class 9. The transfer functions are distributed over all of the 9 classes with an almost constant number of individuals for classes 4, 5, 6, and 7 (~11%), a more consequent number for classes 2 and 3 (~17%), and a lower number for classes 1, 8, and 9 (~3 % and ~7%).

Class	Percentage of channels	Capacity interval (Mbps/s)	Capacity (Mbps/s) [1MHz-100MHz]
1	3.49 %	1000-1200	1120
2	16.78 %	1200-1400	1307
3	18.18 %	1400-1600	1486
4	11.88 %	1600-1800	1687
5	11.88 %	1800-2000	1899
6	12.58 %	2000-2200	2098
7	9.79 %	2200-2400	2298
8	7.69 %	2400-2600	2499
9	7.69 %	2600-2800	2699

Table 6: Channel percentages and average capacities of classes

The distribution of the sites by class is indicated in Table 7. Excepting the class 1, the other classes consist of transfer functions from various sites (3 to 6 sites). The sites are variable in terms of size (apartments, houses) and building construction date (recent and old electric installations), as the CTF measured on of each site may correspond to low-capacity classes as well as high-capacity classes.

Class number	Sites
1	6
2	1, 5, and 6
3	1, 3, 4, 5, 6, and 7
4	1, 3, 4, and 7
5	1, 3, 4, 5, and 7
6	2, 4, 5, and 7
7	2, 4, 5, and 6
8	2, 3, 4, and 6
9	1, 2, 3, 5, 6, and 7

Table 7: Distribution of sites by class

More interestingly, the CTF corresponding to the same class present the same average attenuation (Figure 9).

3.2 Average Attenuation and Phase Modelling

3.2.1 Average Attenuation Modelling

As the channels of each class follow almost the same average frequency response, an average attenuation model is proposed by class.

Table 8 shows for each class the equation of its average attenuation model (in dB) as a function of the frequency f which varies between 1 MHz and 100 MHz with a 100 KHz step.

Class number	Channel model
1	$-80+30.\cos\left(\frac{f}{5.5.10^7}-0.5\right)$
2	$-43+25.\exp\left(\frac{f}{3.10^6}\right)-\frac{15}{10^8}f$
3	$-38+25.\exp\left(\frac{f}{3.10^6}\right)-\frac{14}{10^8}f$
4	$-32+20.\exp\left(\frac{f}{3.10^6}\right)-\frac{15}{10^8}f$
5	$-27+17.\exp\left(\frac{f}{3.10^6}\right)-\frac{15}{10^8}f$
6	$-38+17.\cos\left(\frac{f}{7.10^7}\right)$
7	$-32+17.\cos\left(\frac{f}{7.10^7}\right)$
8	$-20+9.\cos\left(\frac{f}{7.10^7}\right)$
9	$-13+7.\cos\left(\frac{f}{4.5.10^7}-0.5\right)$

Table 8: Average attenuation model by class

Figure 10 and Figure 11 show, for the classes 2 and 6, the set of measured CTF (blue thin curves) and their average attenuation models (red bold curves).

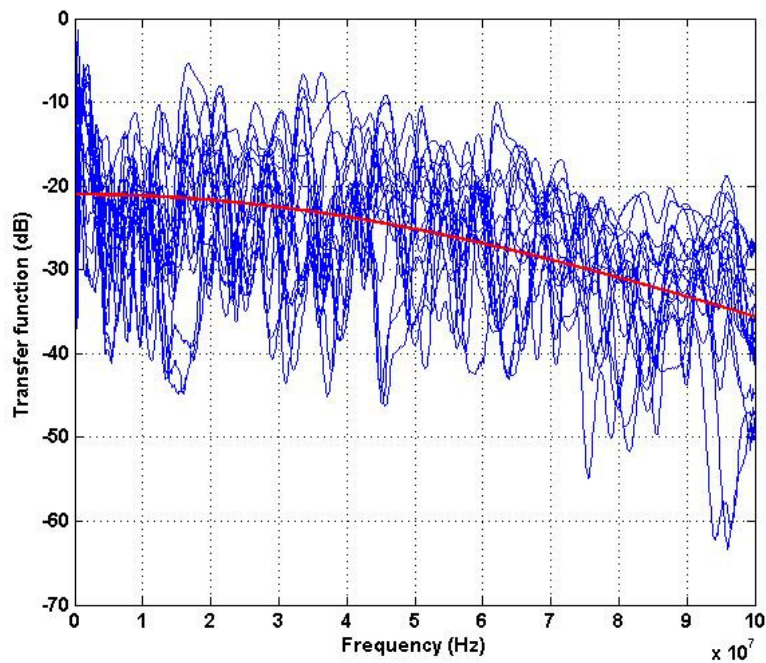


Figure 10: Channels and average attenuation model of class 6.

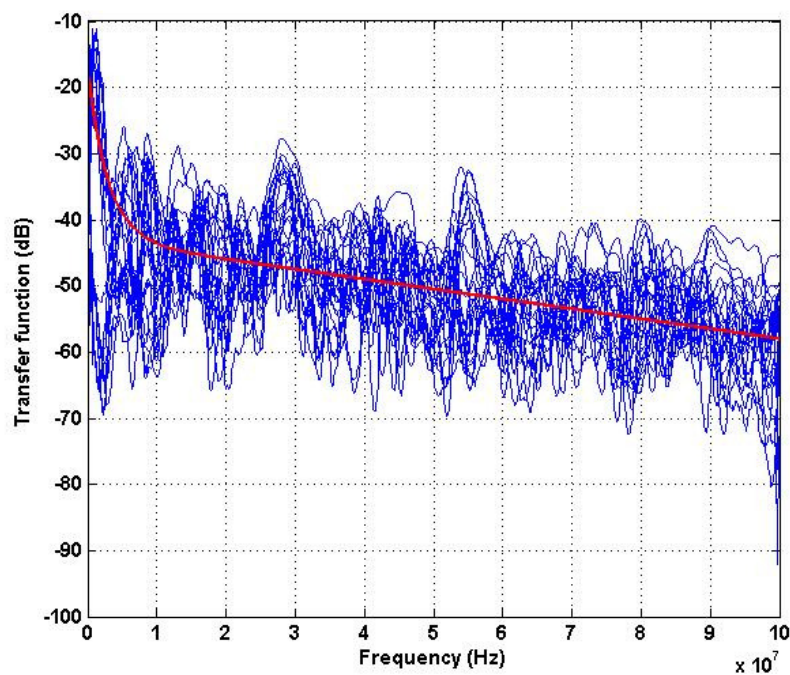


Figure 11: Channels and average attenuation model of class 2.

Figure 12 shows the gathered average attenuation models of the classes 1 to 9.

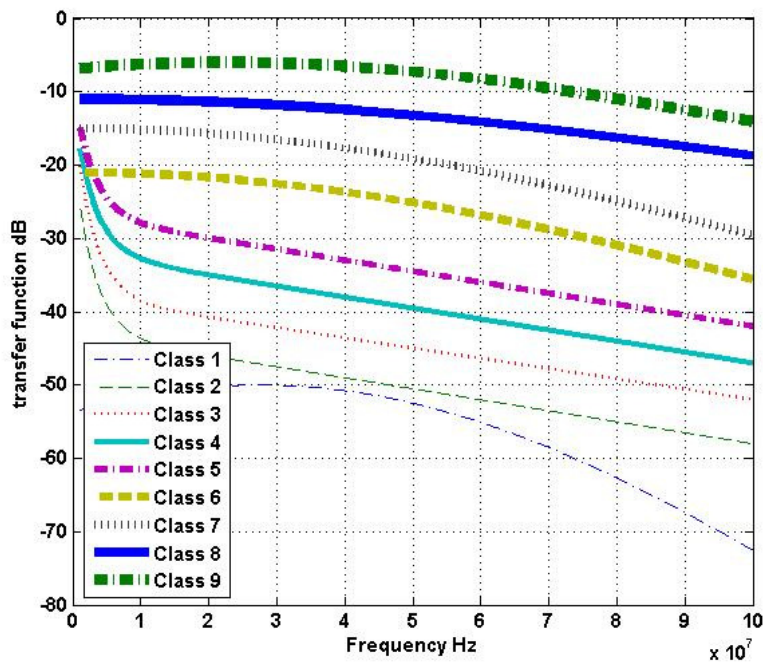


Figure 12: Gathered average attenuation models.

3.2.2 Average Phase Modelling

In the preceding Sections, a PLC channel classification was carried out, and an average attenuation model was suggested per class. In this section, an average phase model per class is proposed.

The blue curves of Figure 13 and Figure 14 represent the measured PLC channel phases of the classes 6 and 2, respectively. Note that the figures represent an unwrapped phase in radians. The average phase model of each class (red bold curves) is obtained by linearization of the median of the blue curves. The phase models of the whole classes are gathered in Figure 15.

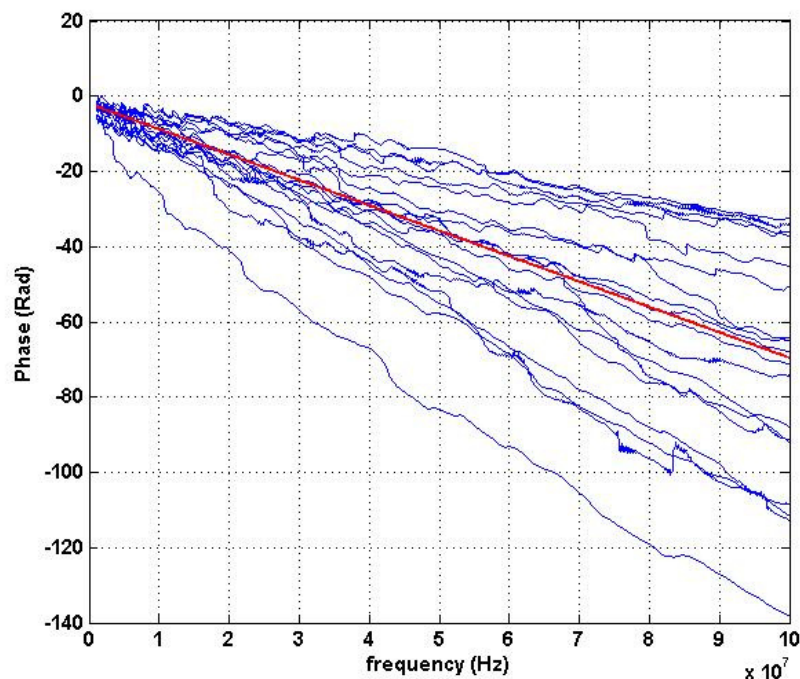


Figure 13: Phases and average phase model of class 6.

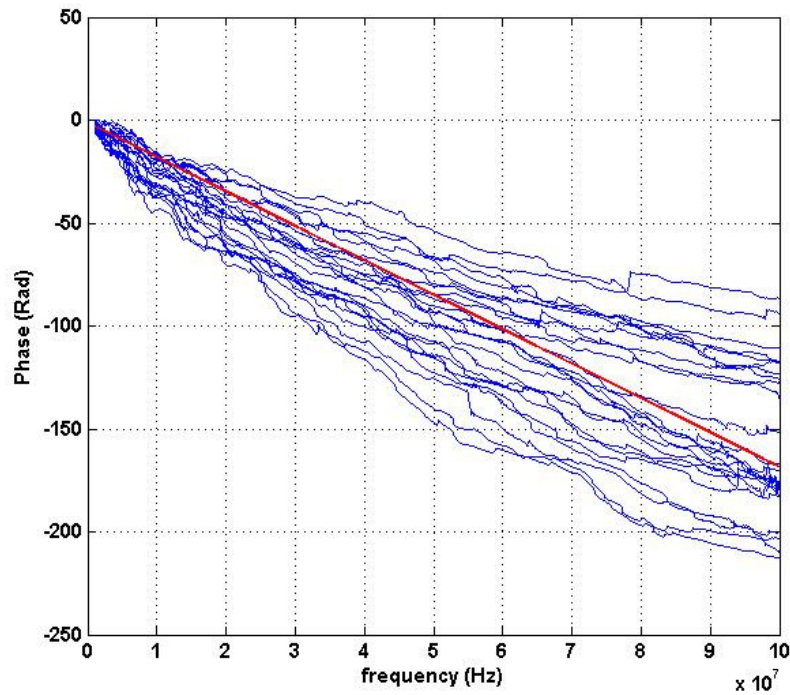


Figure 14: Phases and average phase model of class 2.

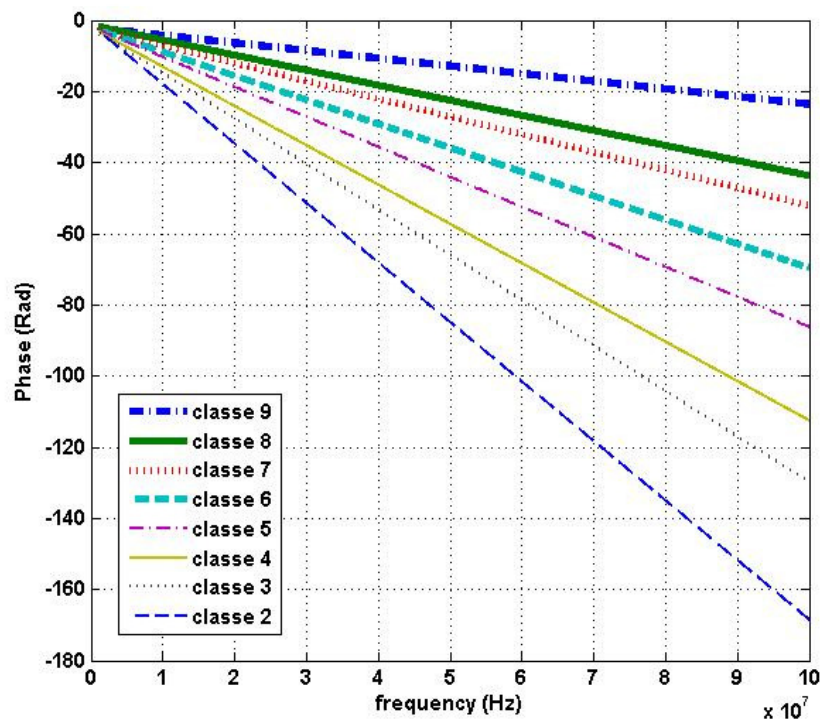


Figure 15: Gathered average phase models.

Obviously, the slopes of Figure 15 curves, which define the group delay², are inversely proportional to the class numbers. Class 9 admits the phase with least slope and group delay as it contains the "shortest" same electrical circuit channels, therefore with least propagation delays.

² The group delay τ_g (in seconds) is defined as $\tau_g = -\frac{d\varphi}{d\omega}$, where φ is the phase in rad, and $\omega=2\pi f$ is the pulsation in rad/s.

We also note that although the channels of each class have very close attenuations, their phases are rather disparate with a difference exceeding sometimes 100 Rad at 100 MHz. This is explained by the fact that in the same class, weak-sloped phases are associated to relative close Tx to Rx with a relative great number of branches. On the other hand, the steeply-sloping phases are associated to more distant Tx and Rx with fewer branches. Although the two cases could have a same attenuation, the group delay of the first case is smaller than the second one.

The class 1 average phase model isn't represented on Figure 15, and falls down to -220 Rad at 100 MHz.

The phase models of Figure 15 are deferred in Table 9, which gives their first values (at 1 MHz), their last values (at 100 MHz), and their slopes. This table contains also the group delay mean values representing the slope of the representative phase of each class.

Class	Phase at 1MHz (Rad)	Phase at 100 MHz (Rad)	Group Delay (µs)
9	-2.3543	-23.6383	0.03424
8	-1.9071	-43.8172	0.06739
7	-2.7401	-52.2321	0.07958
6	-2.7781	-69.5778	0.10742
5	-2.7968	-86.2458	0.13419
4	-3.2573	-112.5762	0.17579
3	-3.5007	-129.8406	0.20316
2	-3.0223	-168.5256	0.26613
1	-3	-220	0.34903

Table 9: Phase models and mean group delay values by class.

At this stage, the built phase models are linear and the magnitude models are smooth and don't include the multipath characteristic of the PLC channels. In the next Sections, the multipath effect is introduced. For the magnitude model, this is based on a statistical study of the measured transfer functions fluctuations around their average attenuations, which is equivalent to statistically studying their fading characteristics.

3.3 Statistical Study of the Channel Frequency Fading

The characterization and the selection of the significant peaks and notches of the measured PLC transfer functions are done in two steps:

- 1) Smoothing of order w of the measured magnitude curves $|H(f)|$. This gives a smoothed transfer function magnitude $|H_{smoothed}|$ defined by:

$$(7) \quad |H_{smoothed}(f_0)| = \sum_{l=f_0}^{f_0+w\Delta f} |H(l)|$$

Δf is the frequency measurement step (100KHz in our case).

- 2) Specification of the extrema (maxima and minima) of the smoothed transfer functions according to the following criterion: an extrema is selected only when it differs by at least 2 dB from its preceding extrema. That's why the third minimum of Figure 16 isn't selected. In case of several consecutive maxima (respectively minima), only the greatest one (respectively the smallest one) is retained: the second maximum of Figure 16 is thus rejected.

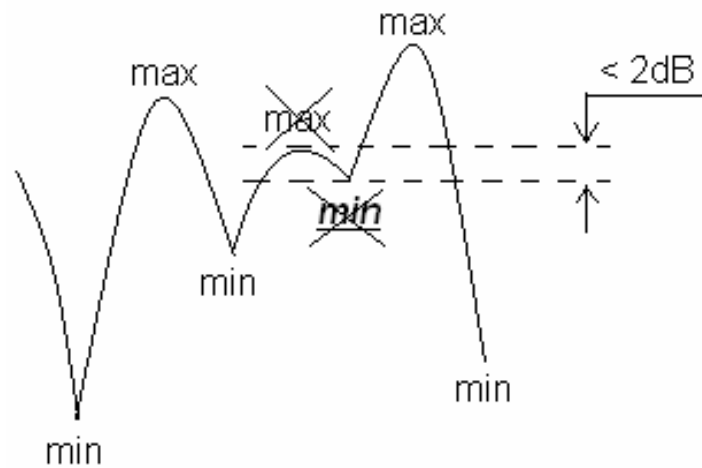


Figure 16: Specification of channel magnitude extrema.

In what follows, a statistical study is performed separately for same electrical circuit channels and different electrical circuit ones. The parameters associated to the selected peaks and notches are widths, heights, and numbers.

3.3.1 Peak and Notch Widths

In this Section, the width of a peak or notch in a CTF is analyzed. The width is defined as the frequency separation (in Hz) between two maxima (in the notch case) or between two minima (in the peak case as shows Figure 17).

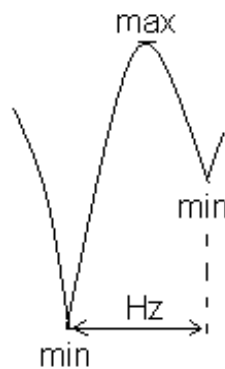


Figure 17: Peak width definition.

Figure 18 and Figure 19 represent (in blue) the widths distributions in the same electrical circuit and different electrical circuit cases, respectively.

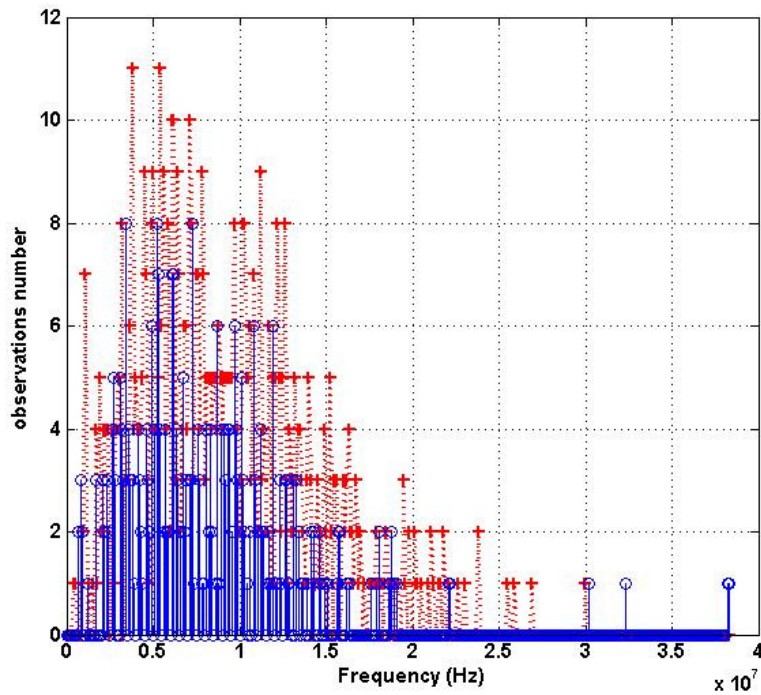


Figure 18: Peak and notch widths distribution – same electrical circuit.

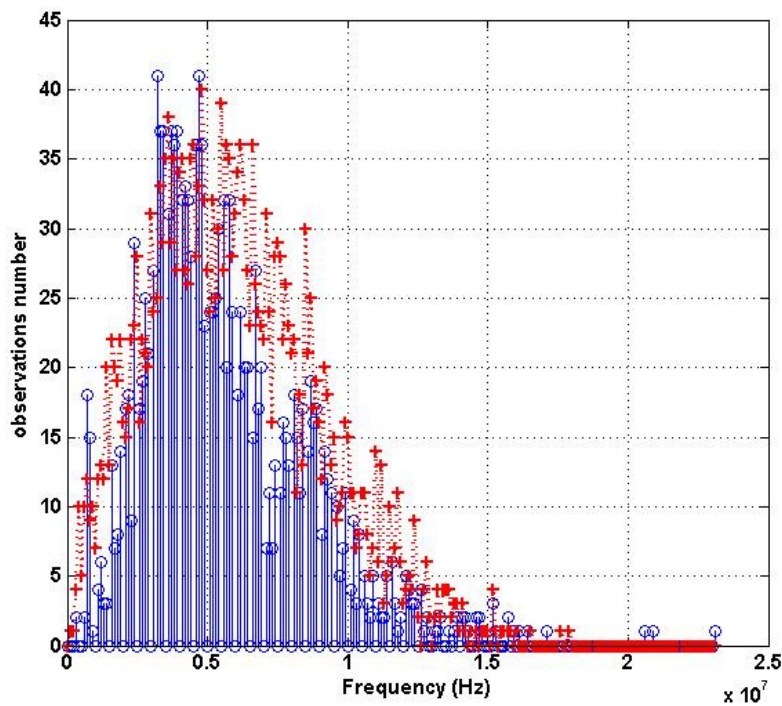


Figure 19: Peak and notch widths distribution – different electrical circuits.

Both Figure 18 and Figure 19 widths distributions could be compared to the Rayleigh distribution defined by the formula:

$$(8) \quad f(x) = \frac{x \cdot e^{-\frac{x^2}{2\sigma^2}}}{\sigma^2} \quad \text{where} \quad \sigma = \sqrt{\frac{1}{2N} \sum_{i=1}^N x_i^2}$$

where N is the number of observations, and x_i is the width of the peak or notch of the observation i .

In the same circuit case, the most representative Rayleigh distribution is defined by $\sigma = 7.1685e6$. In the different circuits case, the more likely value of σ is equal to $4.6341e6$.

Measurements demonstrated that the channel frequency responses of the same electrical circuit case present fewer notches and larger peaks than the different electrical circuit case. Not surprisingly therefore, the standard deviation of their Rayleigh distribution assumed a relatively high value.

The red curves of Figure 18 and Figure 19 represent two random drawings according to the selected Rayleigh distributions. We note that there is a good agreement between measured widths and suggested distributions.

3.3.2 Peak and Notch Heights

In this Section, the height of a peak or notch in a CTF is analyzed. The height is defined as the difference in dB between a minimum and the following maximum (in the peak case as shows Figure 20), or between a maximum and the following minimum (in the notch case).

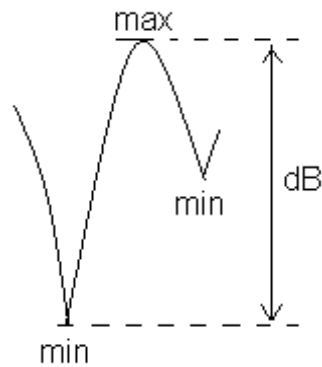


Figure 20: Peak height definition.

Figure 21 and Figure 22 represent (in blue) the heights distributions in the same electrical circuit and in different electrical circuit cases, respectively.

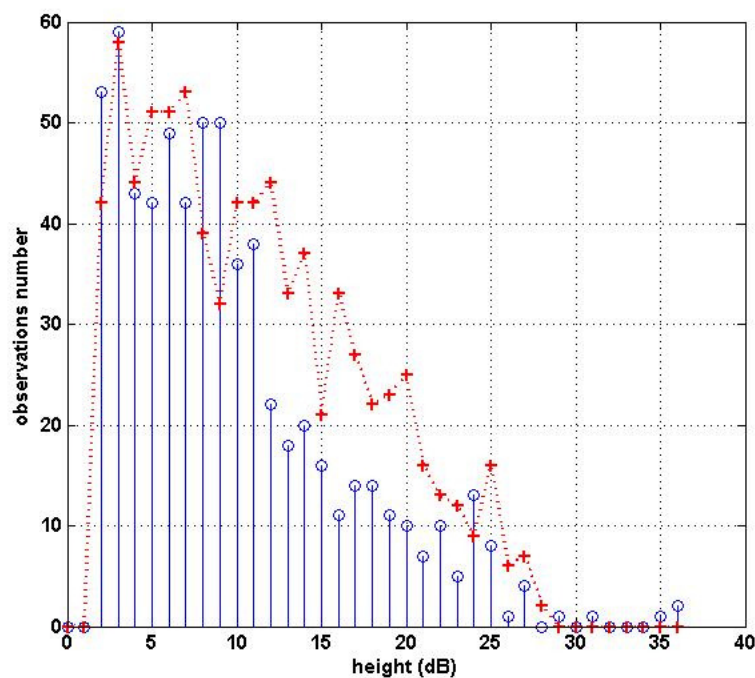
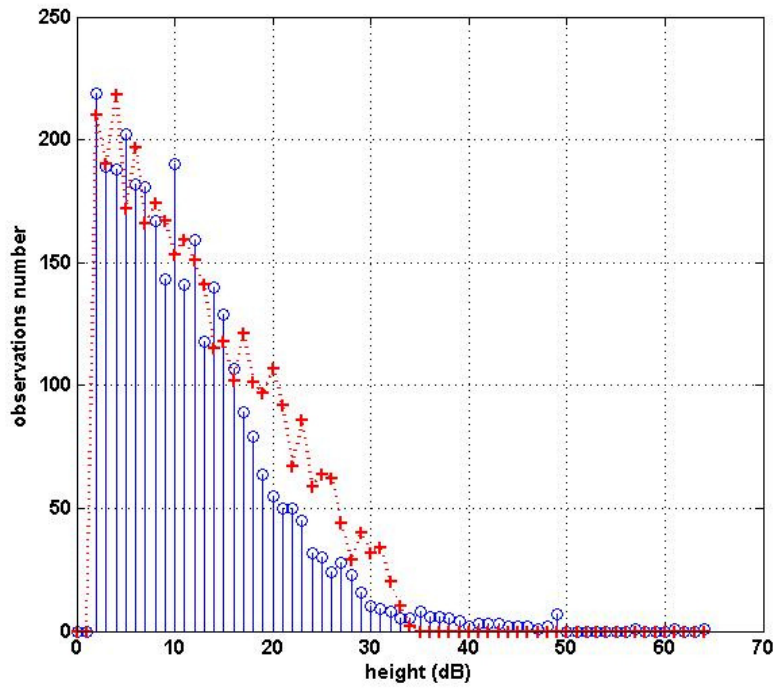


Figure 21: Peak and notch heights distribution – same electrical circuit.**Figure 22:** Peak and notch heights distribution – different electrical circuits.

Here, the suggested heights distribution is the triangular distribution defined by the formula:

$$(9) \quad f(x) = \begin{cases} \frac{2(b-x)}{(b-a)^2}, & a \leq x \leq b \\ 0 & , \text{ else} \end{cases}$$

where a and b are respectively the minimal peak-height value (most recurring one) and the maximal peak-height value (least recurring one).

In the same circuit case, the most representative triangular distribution is defined by $a = 2\text{dB}$ and $b = 30\text{dB}$. In the different circuits case, the values of a and b are respectively equal to 2dB and 35dB .

The red curves of Figure 21 and Figure 22 represent two random drawings according to the considered triangular distributions. We note, once more, a good agreement between height measurements and proposed distributions.

3.3.3 Peak and Notch Numbers

In this Section, the number of peaks or notches in a CTF is analyzed.

Figure 23 and Figure 24 represent the distributions of the number of peaks and notches in the same and in different electrical circuit cases, respectively. Although the number of observations was weak, we can observe a Gaussian distribution tendency defined by the formula:

$$(10) \quad f(x) = \frac{1}{\sigma\sqrt{2\pi}} \exp\left(-\frac{(x-\mu)^2}{2\sigma^2}\right)$$

where σ^2 and μ are respectively the variance and the mean of the observations.

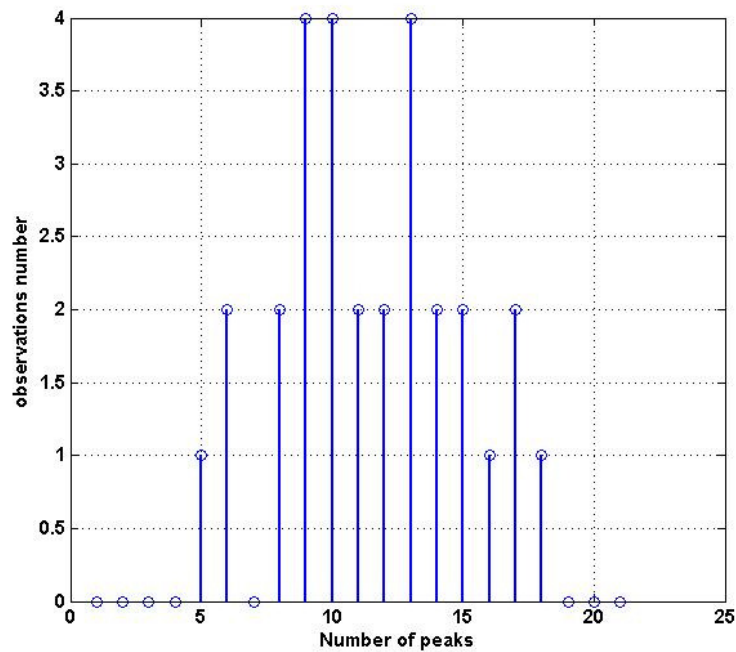


Figure 23: Number of peaks and notches distribution – same electrical circuit.

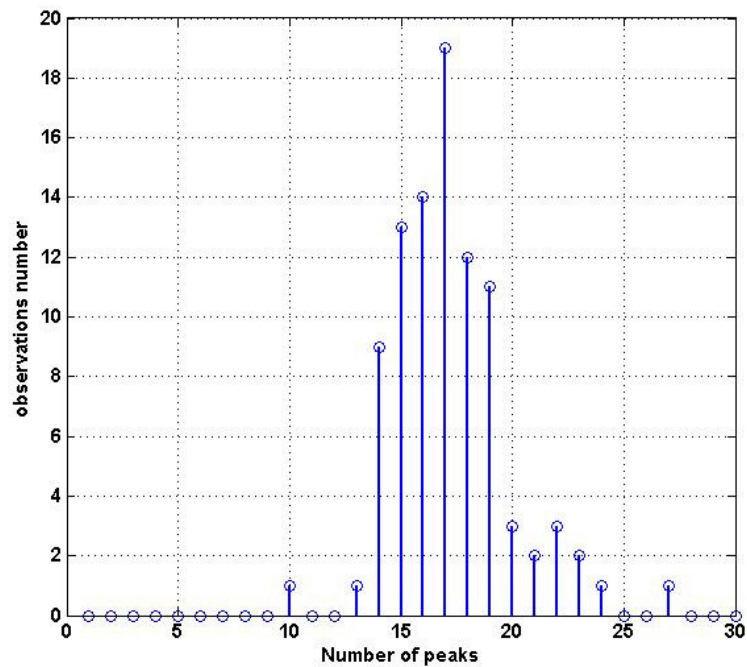


Figure 24: Number of peaks and notches distribution–different electrical circuits.

In the same circuit case, the most representative Gaussian distribution is defined by $\mu = 11.4828$ and $\sigma^2 = 11.83$; and in the different circuits case, the value of μ and σ^2 are respectively equal to 17.1848 and 6.8116. The number of peaks and notches is higher in the different circuits case, as there is more branches and then more reflexions and echoes.

For a fixed class number, the statistical results obtained above are used, in the next section, to introduce the multipath component to the average attenuation of the PLC channel to generate.

3.4 Channel Transfer Function Generator

3.4.1 PLC Magnitude Generator

After fixing the class number of the generated channel, the multipath channel magnitude generator acts into two steps: generation of peaks and notches according to the statistical results and introduction of the average attenuation of the selected class.

We note that classes 9 and 8 contain only channels where the Tx and Rx plugs are on the same electrical channel. Classes 6 to 1 are composed of different electrical circuit channels only. Class 7 is composed of an equal mixture of same circuit and different circuits channels.

3.4.1.1 Peaks and Notches Generation

In this first step, the peaks and notches are generated according to their widths and heights distributions. Here, the transfer function attenuation is considered null.

The first-stage transfer function magnitude is generated by consecutive pairs of increasing/decreasing, half-lobes generated up to the 100 MHz frequency. This leads, finally, to a succession of lobes whose shapes are depicted in Figure 25.

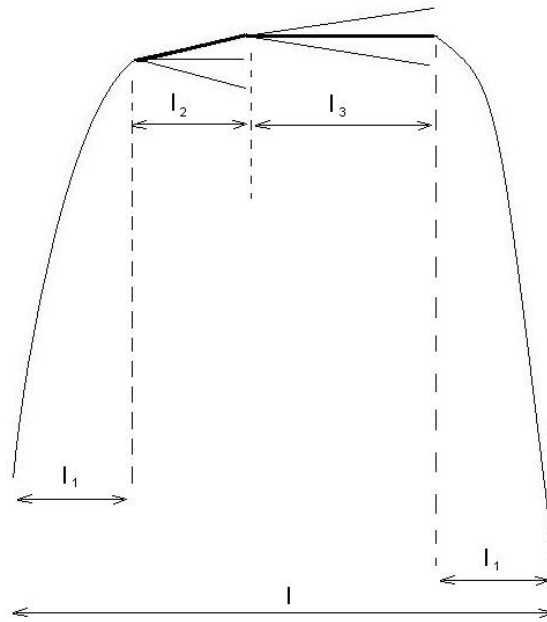


Figure 25: Lobe structure.

In order to make the generated lobe similar to measured lobes, it is divided into four sections: an l_1 wide increasing section of width l_1 , followed by two low-slope linear section (widths l_2 and l_3), followed by a decreasing section of width l_1 . The construction of the lobe is performed according to the following method.

Denoting h the height of the lobe, measured lobe observations demonstrated that the widths of the increasing and decreasing sections are inversely proportional to h . For largest values of h ($h_{\max}=30\text{dB}$ in the same circuit case, and $h_{\max}=35\text{dB}$ in the case of different electrical circuits), $2.l_1$, which is the sum of increasing and decreasing sections widths, represents only $1/4$ of the total width l of the lobe. While, for the smallest value of h ($h_{\min}=2\text{dB}$), $2.l_1$ is equal to $3/4$ of the lobe width l . Generally, l_1 is calculated according to the following formula:

$$(11) \quad 2l_1 = \frac{l}{2(h_{\max} - h_{\min})} (h - h_{\min}) + \frac{l}{4}$$

where l_2 takes a random value between 0 and $l - 2l_1$, and $l_3 = l - 2l_1 - l_2$.

In Figure 26 and Figure 27 are reported two generated 1st stage transfer functions related to the same circuit and different circuits cases, respectively.

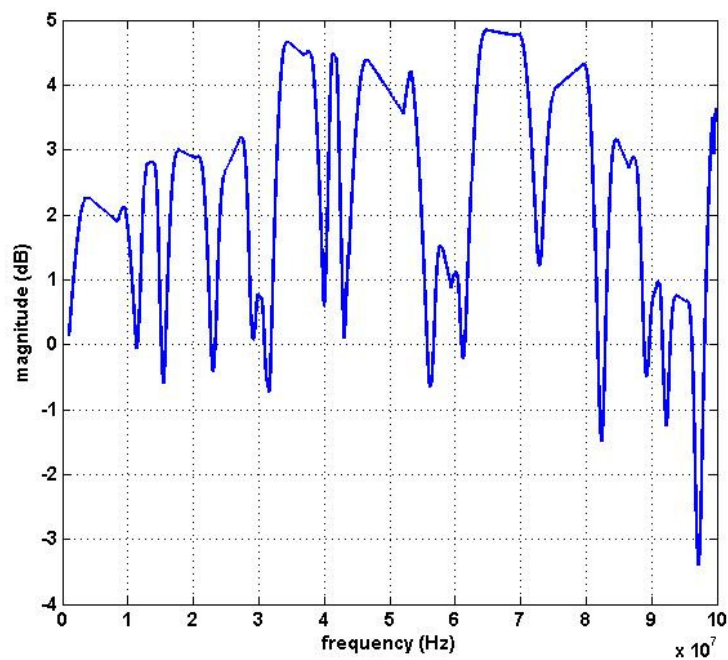


Figure 26: 1st stage magnitude generation – same electrical circuit.

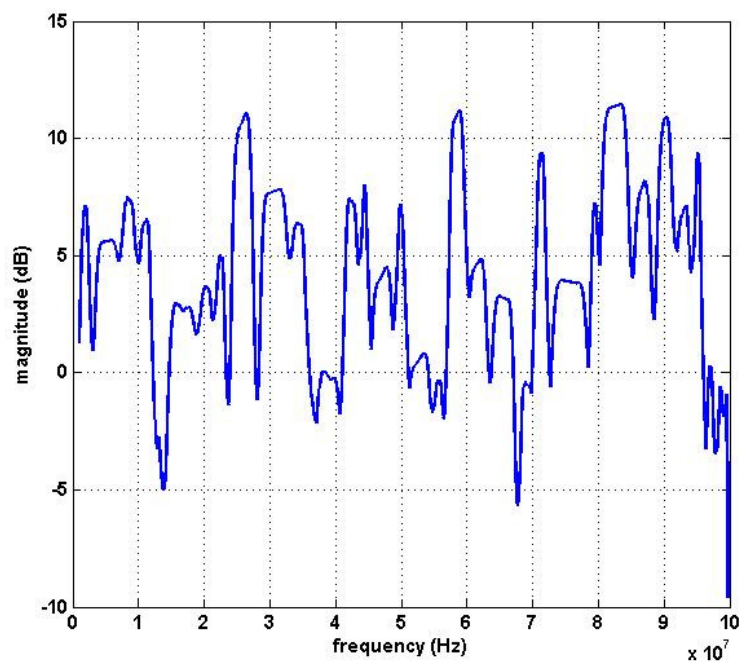


Figure 27: 1st stage magnitude generation – different electrical circuits.

3.4.1.2 Introduction of the Average Attenuation

In the second step of the magnitude generation process, we apply to the "flat" 1st step magnitude the average attenuation model of the selected class.

Figure 28 represents a class 9 generated magnitude, and Figure 29 a class 2 one.

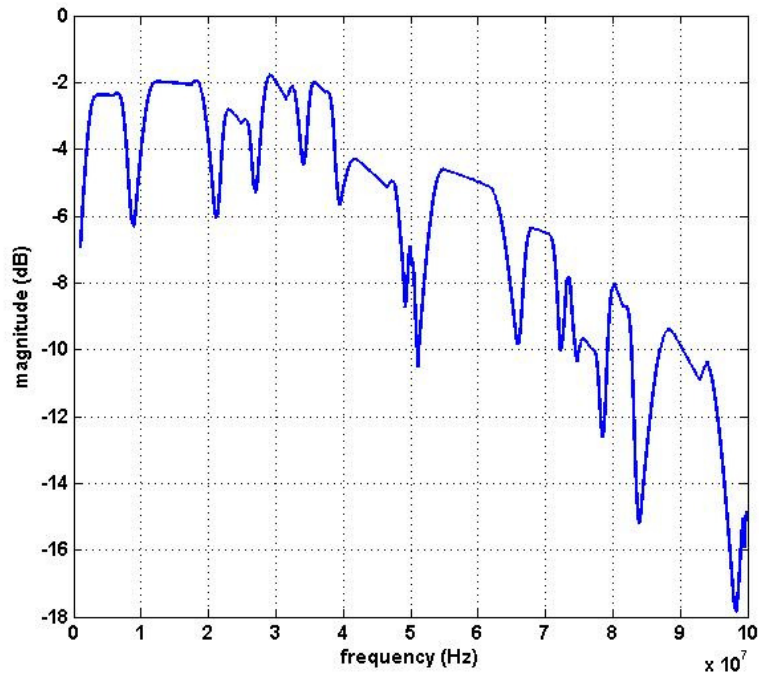


Figure 28: 2nd stage magnitude generation – class 9.

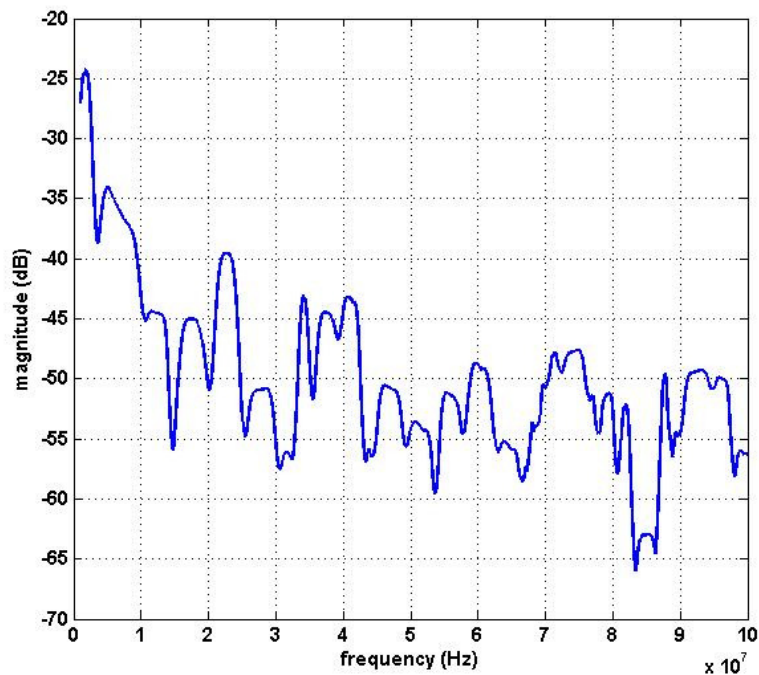


Figure 29: 2nd stage magnitude generation – class 2.

In order to validate the PLC transfer function magnitude generator, capacities are calculated for 100 generated channels per class. The distribution of the simulated class 2 channel capacities, presented on the histogram of Figure 30, is almost completely comprised between 1.2 and 1.4 Gbits/s, which corresponds to capacity interval of class 2.

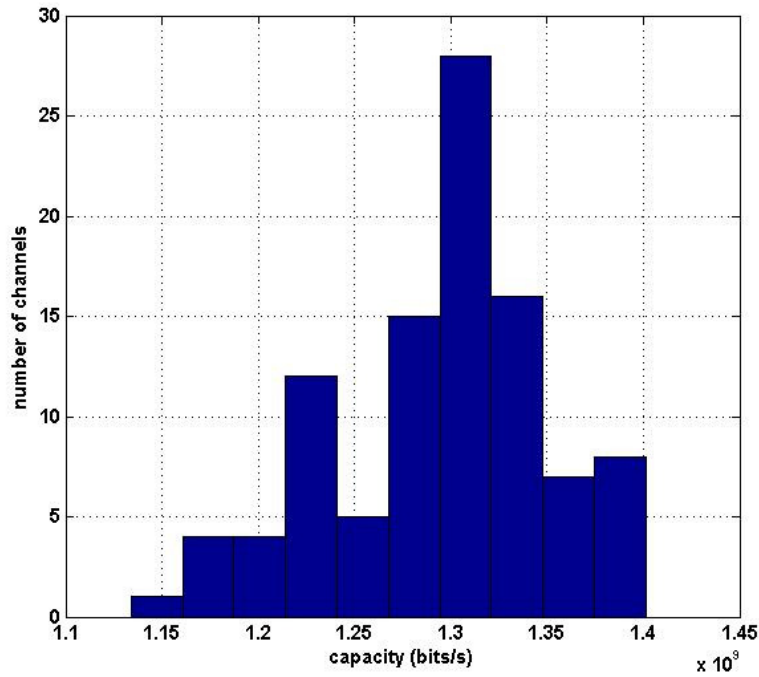


Figure 30: Histogram of the class 2 channel capacities distribution.

3.4.2 PLC Phase Generator

In Section 3.2.2, linear phase models per class were developed. In this Section, multipath is introduced. As the fluctuations brought to the phase conditions the delay spread of the resulting impulse response, this step is determinant for building PLC channels presenting impulse responses as close as possible to the measured ones.

Low numbered classes have impulse responses presenting larger maximum delay spreads and RMS delay spreads (see [27][28]). We observed that the low numbered classes present a linear phase with a larger slope than high numbered classes. However, this does not guarantee a larger delay spread: controlling the linear phase only does not accurately render the observed delay spread for each class.

To refine the model characteristics in the time domain, some global and local distortions are applied to the linear phases. Local distortions are applied around the notched frequencies of the built transfer functions.

3.4.2.1 Global Distortions Applied to the Linear Phases

Intuitively, a linear phase privileges a unique path whose delay is proportional to the slope of the phase line.

In order to create a diversity of paths, and consequently enlarge the RMS delay spread, a concavity is applied to the linear phase, as presented in Figure 31. This concavity is inversely proportional to the class number.

Table 10 reports the concavity depth C_c (see Figure 31) as a function of the class number.

We note that this concavity phenomenon is well present in the channel measures and particularly with the low numbered classes (see Figure 14).

The concavity distortion applied to the linear phase is further followed by local distortions explained in the following subsection.

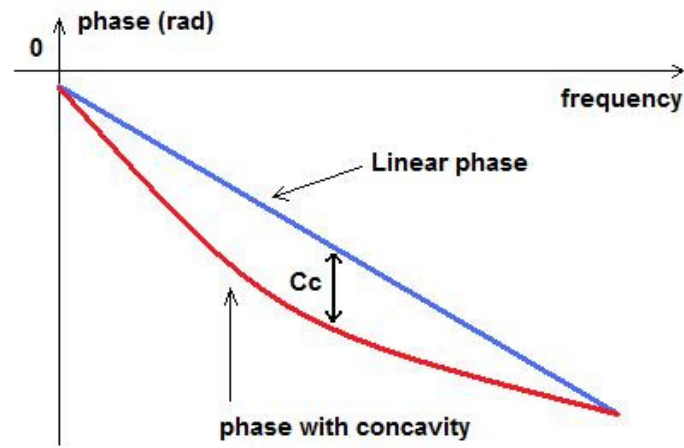


Figure 31: Concavity application to the linear phase.

Class number	Concavity Depth (Cc)
1	30
2	30
3	30
4	10
5	10
6	5
7	5
8	3
9	3

Table 10: Concavity depth Cc by class

3.4.2.2 Local Distortions Applied to the Linear Phases

Local distortions concern the non-linear behaviour of the phase at the notch frequencies. This is expressed by:

- phase shifts at the selected notch frequencies,
- phase fluctuations around these frequencies.

Phase shifts are generated so that the phase difference between frequencies just before the notch frequency and frequencies just after it takes arbitrary values between 0 and 2π .

Around notch frequencies phase fluctuations are introduced. As presented in Figure 32, increasing amplitude cosines are inserted in the left of each notch frequency, and decreasing amplitude ones are inserted on the right side. Between the two cosines an arbitrary phase difference is applied. Note that at this figure, the phase shift is almost equal to 2 rad.

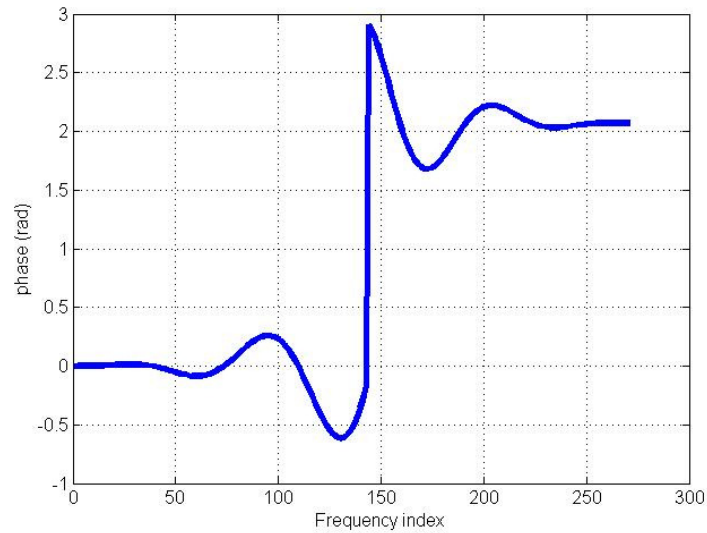


Figure 32: Local distortions applied to the linear phase.

Observing the group delay of the measured PLC channels, we distinguish peaks in the group delay measured around notch frequencies. These peaks, characterizing the phase non-linearity at these frequencies, may correspond to either positive shifts or negative shifts (see Figure 33 and Figure 34). Observations showed that group delay peaks generally correspond to negative shifts in the high numbered class channels (see Figure 34), and equitably take positive and negative shifts in the low numbered class channels case (see Figure 33).

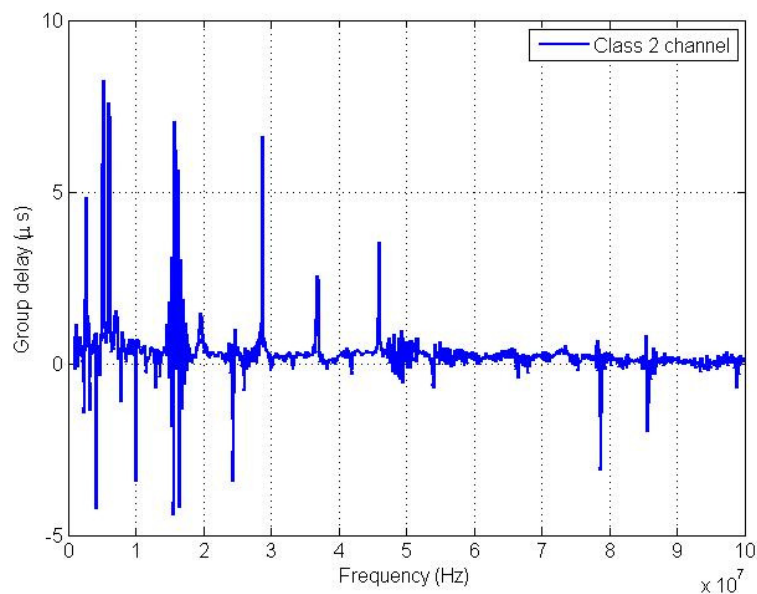


Figure 33: Class 2 channel measured group delay.

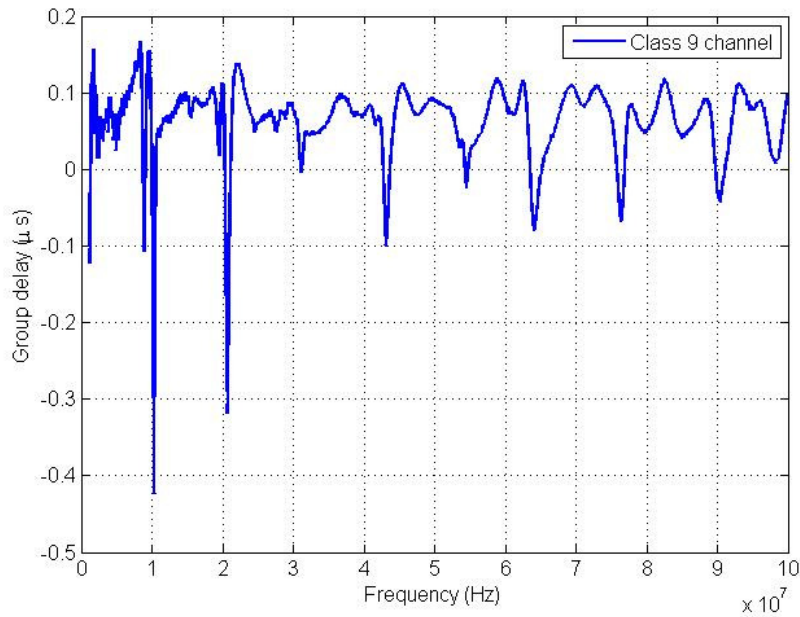


Figure 34: Class 9 channel measured group delay.

As the sign of the phase shift, at a given notch, conditions the direction of the associated group delay peak, phase shift signs are generated according to Table 11 probabilities.

Class number	Positive sign probability	Negative sign probability
1	0.5	0.5
2	0.5	0.5
3	0.4	0.6
4	0.3	0.7
5	0.2	0.8
6	0.1	0.9
7	0	1
8	0	1
9	0	1

Table 11: Phase shift signs probabilities

Classes 9, 8, and 7 group delays only present negative peaks. Classes 1 and 2 group delays present both positive and negative peaks with the same probability.

3.5 Channel Impulse Response Generator

We present in this Section different methods for the generation of a CIR, starting from the frequency response provided by the CTF generator (see Section 3.4). The following question arises: is it possible to reduce the number of coefficients of the channel response, and thus obtain a simple method approaching the best the CIR. This Section is therefore related to the analysis, development and comparison of different methods.

3.5.1 Regeneration of the Impulse Response

Figure 35 shows the CTF versus frequency. The sampling frequency is 200 MHz.

The x-axis ranges from 1 MHz to 100 MHz with a 25Khz step.

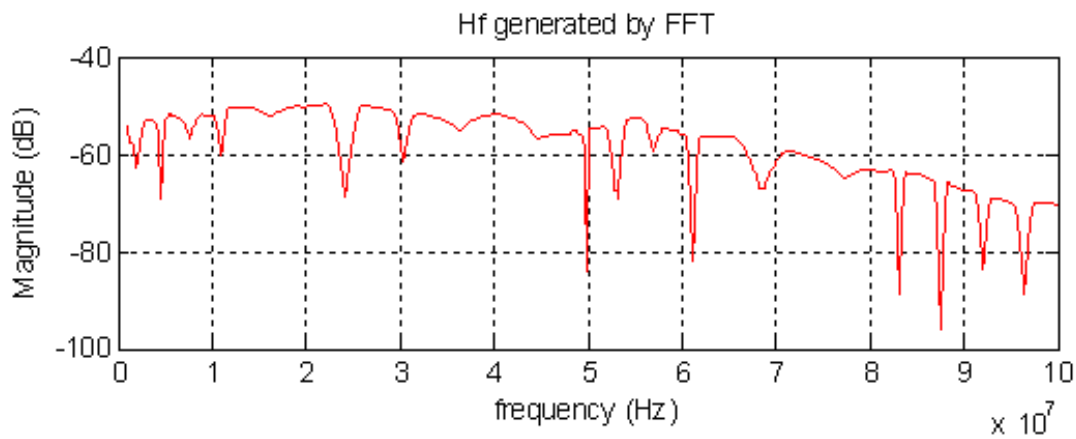


Figure 35: Generated CTF.

The following figure represents the CIR generated by the IFFT. To retrieve the CIR, one have to complete the beginning of $H(f)$ with zeros and then make a Hermitian symmetric (because $H(f)$ has been provided for the frequency band from 1 MHz to 100 MHz).

This can be done easily by typing in MATLAB the following line of code:

```
%40=1000/25
debut=zeros(40,1);
Hf=[debut;Hf];
Hf=[Hf;0;flipud(conj(Hf(2:end)))];
IR_IFTT= ifft(Hf);
```

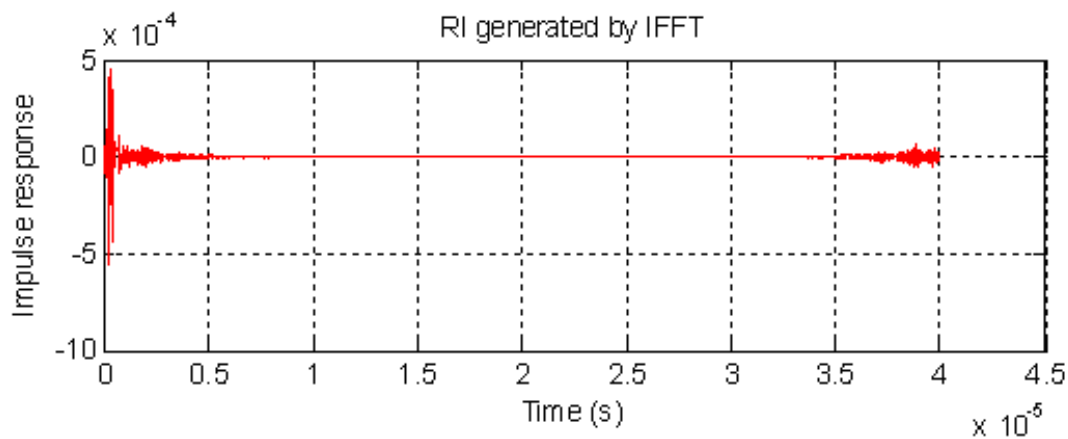


Figure 36: Generated real-valued CIR.

The generated CIR are very long (8002 points). They are not applicable in the simulation. For this reason we will propose some methods to generate the best response with a sufficient number of points. Let's note that the CIR in Figure 36 is given as an example for the comparison that will be made in the next sections, it is then not representative of all the impulse responses and does not give a statistical analysis of PLC CIR, which is given in Section 2.3.2.2, Table 4.

3.5.2 First Method: by Truncation

This method is to truncate the impulse response using a threshold.

The flowing algorithm describes this method:

- 1 - Find the index i_{\max} of the maximum magnitude of the CIR $h(i)$, i.e. $|h(i_{\max})| = \max_i |h(i)|$
- 2 - Select a threshold $ThdB$
- 3 - Calculate $w = \max_i |h(i)| - ThdB$
- 4 - Calculate $i_{\text{trunc}} = \min_i \{i, |h(i)| < w\}$
- 5 - Select the truncated impulse response as: $h(n)$, $n=1, \dots, i_{\text{trunc}}$

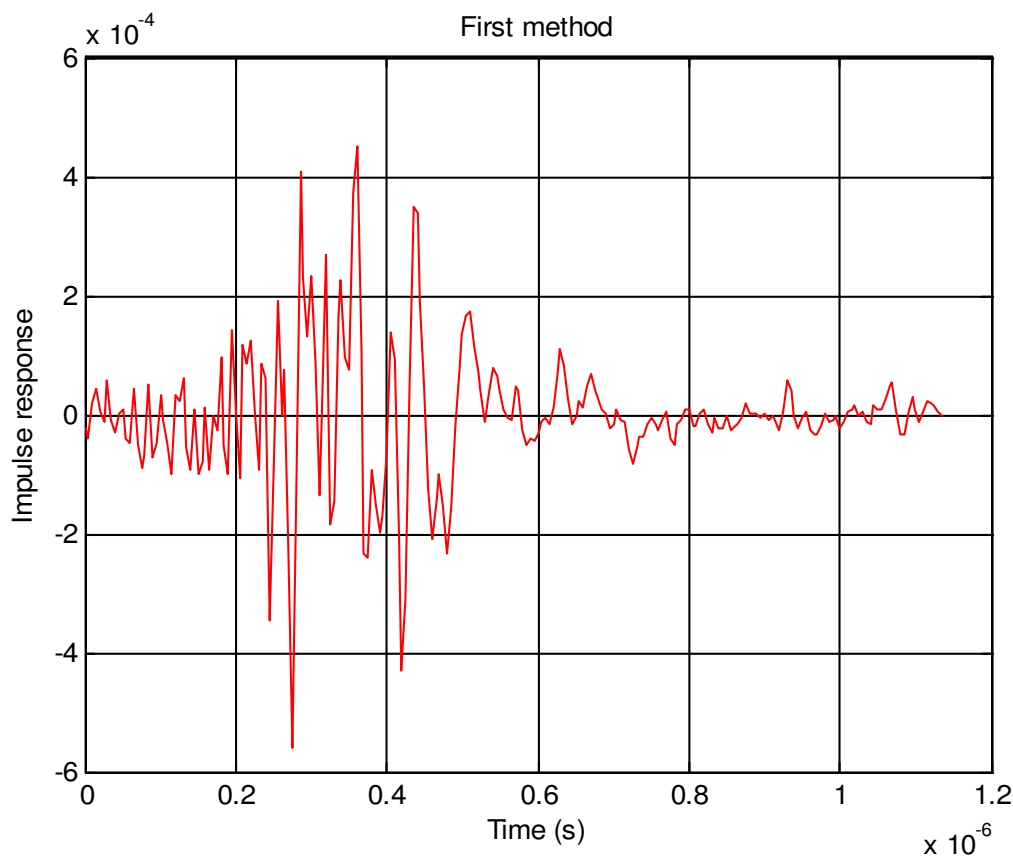


Figure 37: Illustration of the truncation method.

3.5.3 Second Method: Truncation by Windowing

This method consists in finding the maximum energy of the CIR in a rectangular sequence of size M . The maximum energy concentration within a frequency band implies minimum total energy spill outside the desired band.

The simple truncated is a rectangular window truncated. We are faced with the problem of deciding the size of the truncated window to get the best approximation of the CIR.

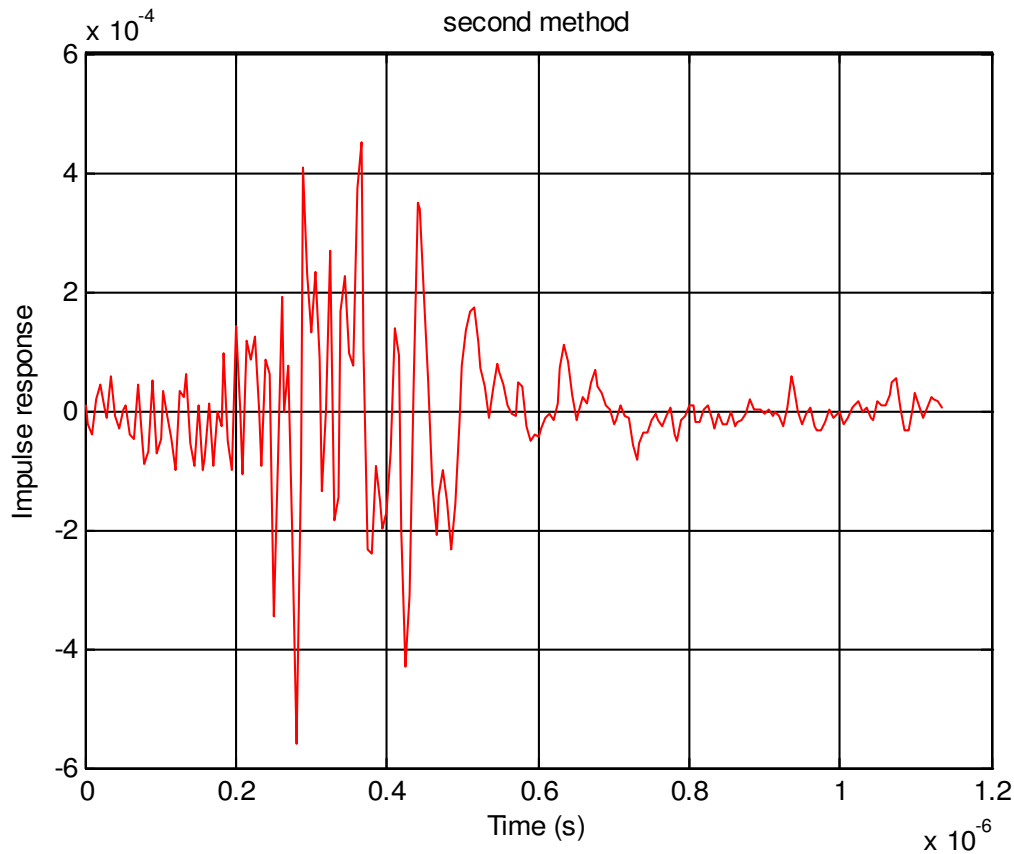


Figure 38: Illustration of the windowed truncation method.

Let $w(n)$ be a rectangular window of size M and $h(n)$ the impulse response of size L (in our case $L = 8002$).

$w(n) = 1$ for $n = 0, \dots, M-1$.

In computing the spectrum of a truncated data sequence, we multiply the data by a set of weights. This is motivated by the fact that the truncation itself corresponds to a set of weights all equal to one within the truncation range and to zero outside it.

The CIR h is divided into blocks of length $M < L$. From a block to the next, the window is shifted by one sample and we multiply $w(n)$ by $h(n)^2$, which is equivalent to a convolution of the untruncated $h(n)^2$ data with $w(n)$.

The choice of IR corresponds to the block that gives a maximum energy.

3.5.4 Third Method: with the invfreqz MATLAB Function

For more information on the invfreqz function, see the help of MATLAB.

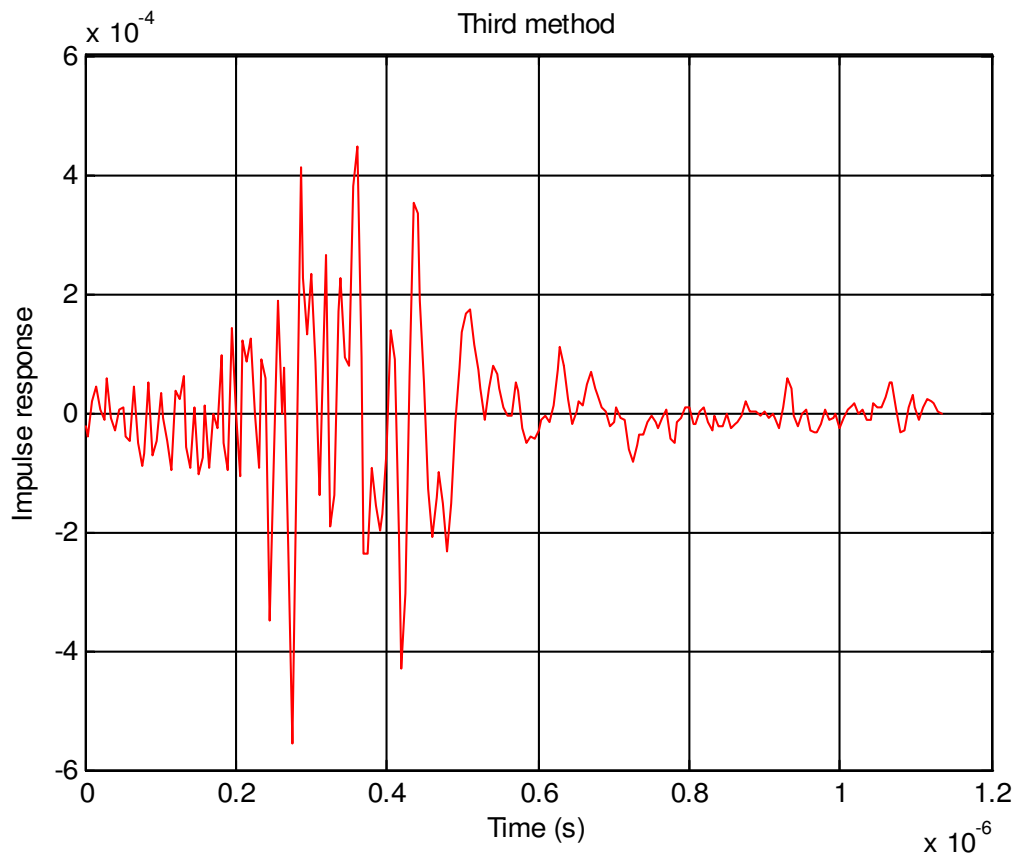


Figure 39: Illustration of the invfreqz function method.

3.5.5 Comparing the Proposed Methods

In this Section, results for the proposed methods realization are compared with the well-known original spectrum. Such comparison is difficult, and the final choice is inevitably dictated by subjective preferences. The comparison here takes into account the MSE criterion. The time domain CIR were truncated so as to have only 228 coefficients, and the resulting spectrum was computed.

The following figures represent the comparison of the CTF $H(f)$ compared to that of the reference provided by the CIR generation using one of the three previous methods.

We note that it is very difficult to see the difference between these three methods.

To compare the results obtained by these three methods, we used the mean square error criterion.

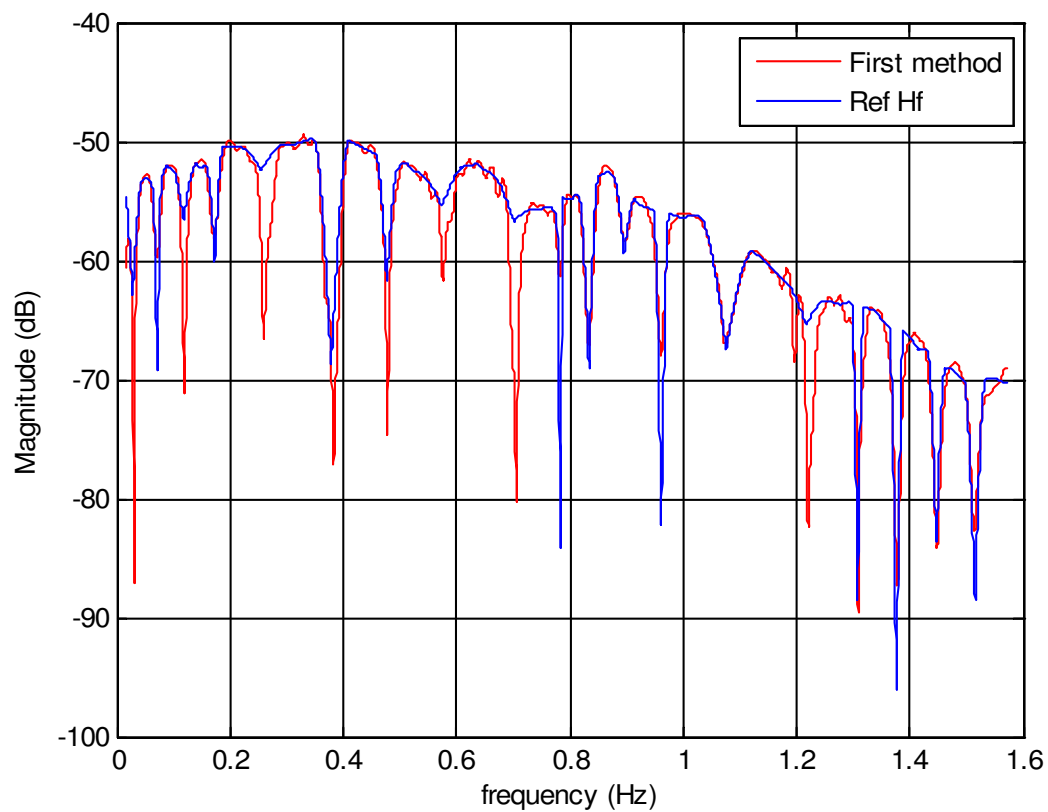


Figure 40: CTF comparison using the truncation method.

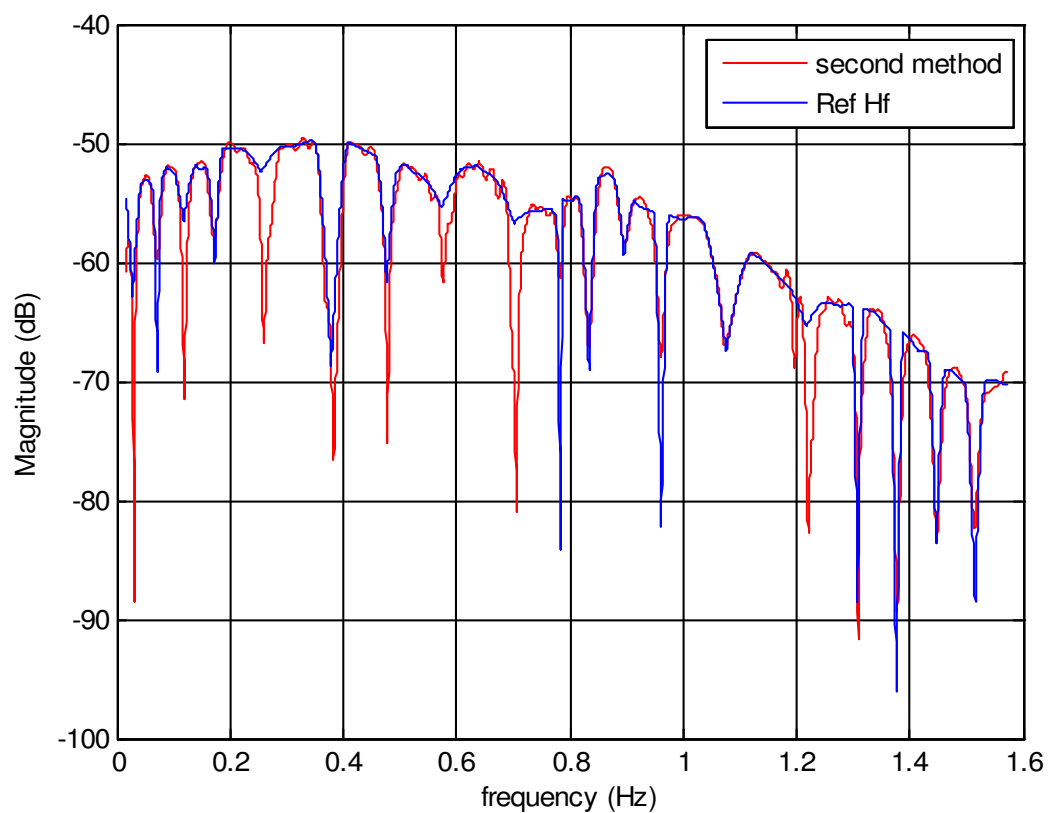


Figure 41: CTF comparison using the windowed truncation method.

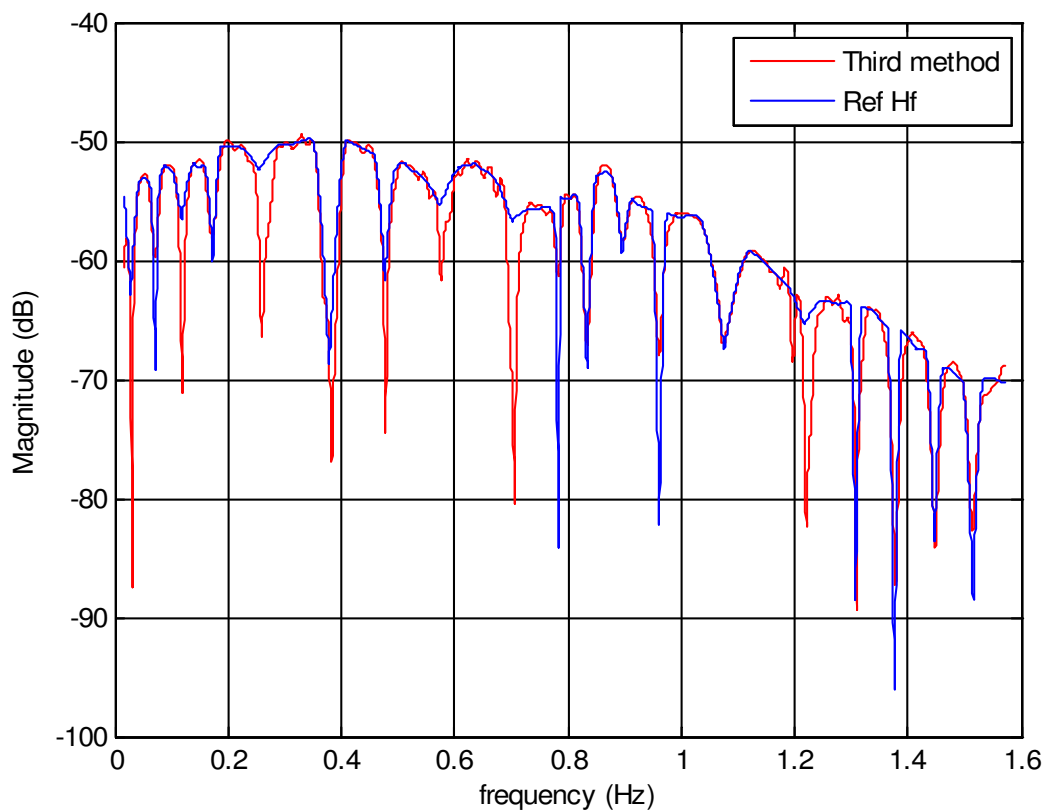


Figure 42: CTF comparison using the invfreqz method.

To compare these methods, we will calculate the mean square error (MSE):

$$(12) \quad MSE = 10 \log_{10} \frac{\sum_{k=0}^{N-1} |H_{ref}(k) - H(k)|^2}{N}$$

	First method	Second method	Third method
MSE (en dB)	-65.0110	-65.0115	-64.9968

Table 12: MSE comparison of the three proposed methods (M = 228)

Table 12 shows the representation of the MSE error for CIR designed by methods 1, 2 and 3. We note that the channel response designed by the method 2 is almost identical in terms of performance than the method 3, but more efficient compared to that of method 1. We conclude that the impulse response designed by the method 2 presents the best approximation in the direction of MSE on a size of a well defined window M (in our case M = 228).

The performance of the method 2 increases with the size of the window M.

The following table shows the results for M = 1213

	First method	Second method	Third method
MSE (en dB)	-67.6271	-73.1011	-67.5559

Table 13: MSE comparison of the three proposed methods (M = 1213)

3.5.6 Conclusion

The studied methods are very close, so what is proposed is to use the first method which is the simplest one to truncate the CIR.

3.6 Simulation Results and Model Validation

Figure 43 and Figure 44 represent respectively for the classes 2 and 9 the generated transfer function magnitudes in dB (top left curves), the generated phases in Rad (top right curves), the generated group delay in μs (bottom left curves), and the associated impulse responses (bottom right curves).

The impulse response shapes are similar to the observed measurements. Furthermore, their maximum excess delays (τ_m) are well in the range of measured maximum excess delays of the considered classes (i.e. $\tau_m \approx 0.35\mu\text{s}$ for class 9 measured channels and $\tau_m \approx 4\mu\text{s}$ for class 2 measured channels [27][28]).

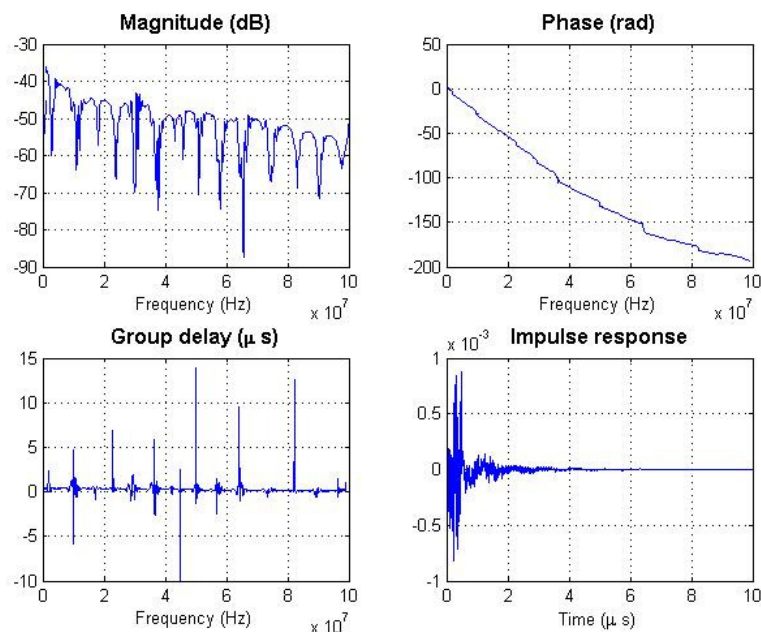


Figure 43: Magnitude and Phase generation – class 2.

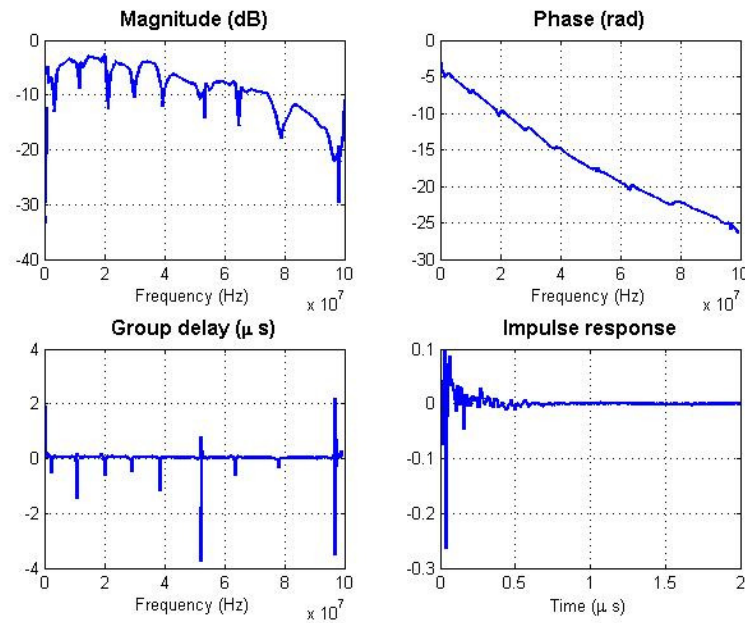


Figure 44: Magnitude and Phase generation – class 9.

In order to validate the model, 100 channels are generated by class, and the mean values of the RMS delay spread and maximum excess delay parameters are calculated for each class. The obtained mean values are then compared to those calculated for the measured channels and reported in [27]. These results are shown in Table 14.

Class number	Measured τ_m (μ s)	Model τ_m (μ s)	Measured τ_{RMS} (μ s)	Model τ_{RMS} (μ s)
1	3.31	3.42	0.31	0.51
2	3.35	3.35	0.31	0.51
3	2.83	3.32	0.27	0.45
4	2.25	2.12	0.22	0.29
5	2.14	2.41	0.21	0.32
6	1.95	2.08	0.19	0.26
7	1.18	1.21	0.16	0.14
8	0.9	0.85	0.08	0.09
9	0.6	0.35	0.07	0.04

Table 14: Model validation delay spread values

This table shows that the proposed model reasonably reflects the delay parameters as observed from the experimental data.

4 Statistical Channel Transfer Function Model Software

In order to share the proposed model of this paper with research community and industrials, a software is developed: Wideband Indoor Transmission channel Simulator for powerline (WITS). This software is based on the channel model of Section 3.

To each channel simulation is associated a workspace creation and definition (see Figure 45). The parameters of powerline channels to create are the frequency interval and step, the number of channels to generate, and the list of classes to which they belong.

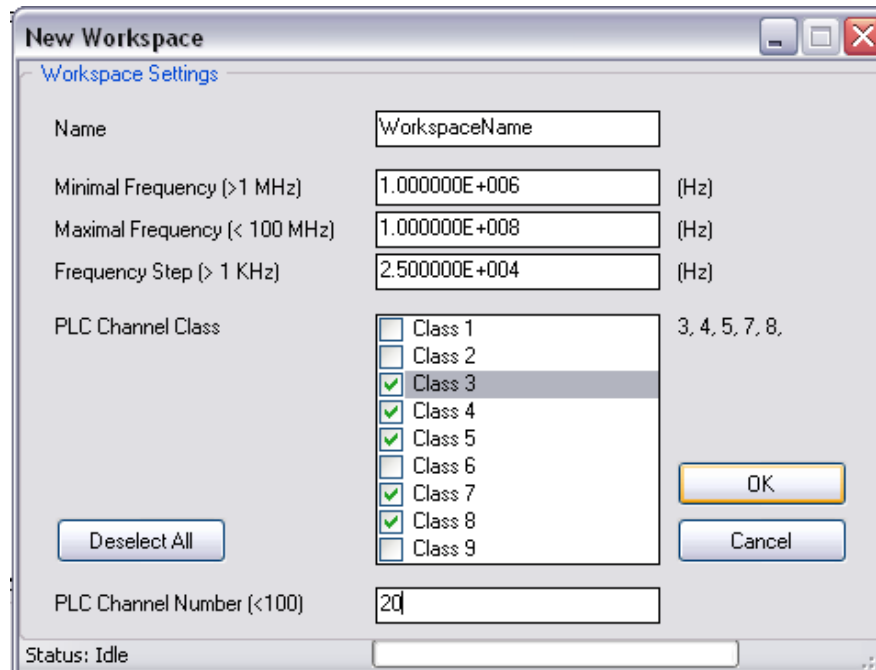


Figure 45: WITS workspace creation and definition.

An overall interface of WITS software is reported in Figure 46.

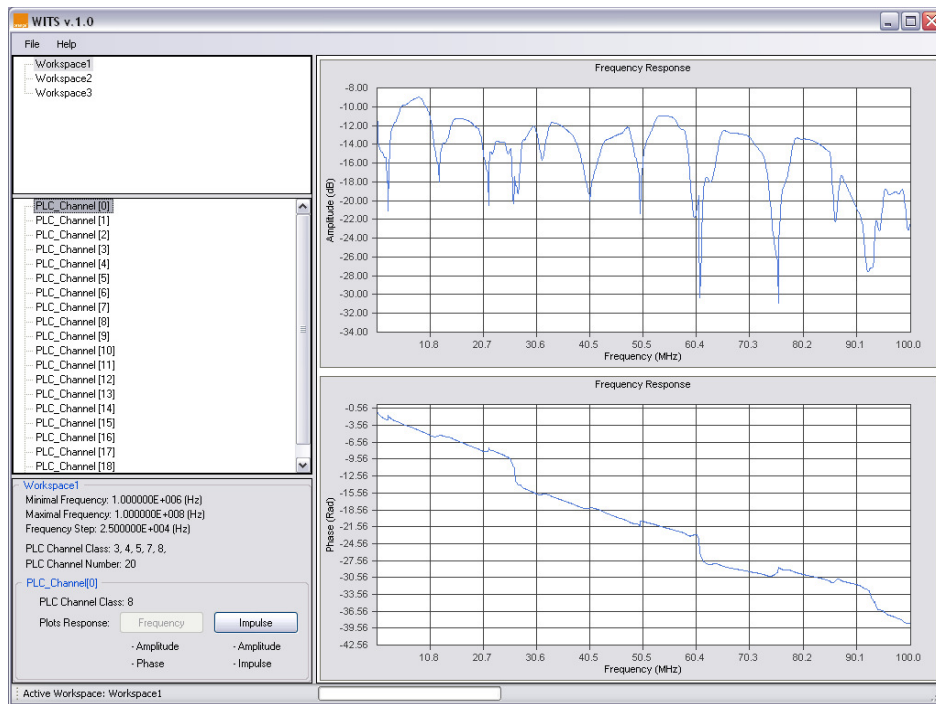


Figure 46: WITS general interface view.

This interface is divided into informational part (left side) and graphical part (right side).

- **Informational part:** in this part are given the list of created workspaces (topt panel), the list of channels of each workspace (middle panel), and information about selected workspace (minimal and maximal frequencies, frequency step, channel classes, and number of channels) and channel (its number and the class it belongs to).
- **Graphical part:** this part consists of two charts showing the frequency response of the selected channel and its unwrapped phase if the "Frequency" plot button is pressed, and its impulse response if the "Impulse" plot button is pressed.

As shown in Figure 47, two exporting options are given in the WITS software:

- Exporting a selected powerline channel.
- Exporting a whole workspace: in this case channel files (as numerous as the number of workspace channels) are created in a directory created or specified by the user.

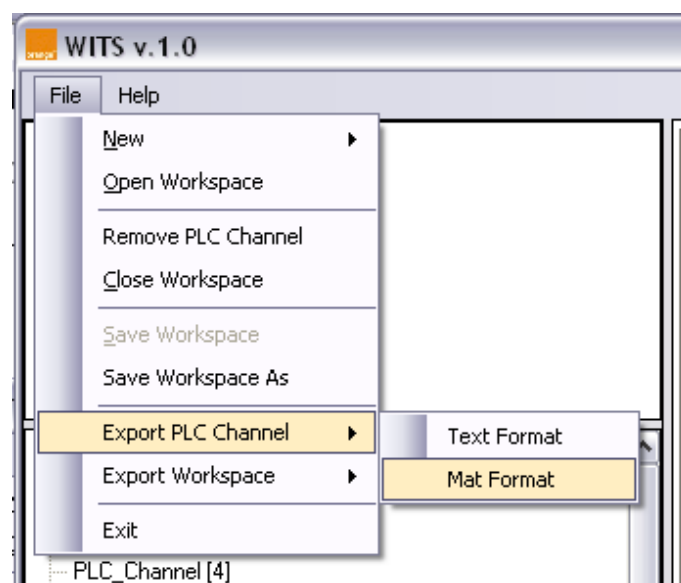


Figure 47: WITS exporting options.

Two saving formats are proposed:

- **Text format:** containing:
 - Frequency response (frequency vector, real and imaginary parts for each frequency).
 - Impulse response (time instants vector and impulse value for each time instant).
- **Mat format:** intended to Matlab users. To each created channel is associated a Matlab structure called "CHANNEL" containing:
 - Class: class number.
 - Frequency: frequency vector
 - H_{real} : real values of the frequency response.
 - H_{imag} : imaginary values of the frequency response.
 - Time: time instants of the impulse response.
 - Impulse: impulse response vector.

5 Analytical Modelling of the Channel Transfer Function

As discussed in the previous sections, it is beneficial to deal with a statistical model that allows capturing the ensemble of power line grid topologies. This is of particular importance for the design and testing of transmission and signal processing algorithms. In this section we describe another top-down approach to the statistical modelling for the channel transfer function (CTF). The approach has been firstly presented in [29] and it is herein investigated in detail. The starting point is the well-known band pass power line channel model in [6], where taking into account the multipath effect, the **frequency response** is synthesized with N_p paths as

$$(13) \quad G_{CH}^+(f) = \sum_{p=1}^{N_p} g_p(f) e^{-j \frac{2\pi d_p}{v} f} G(f, d_p), \quad 0 \leq B_1 \leq f \leq B_2,$$

where $g_p(f)$ is the transmission/reflection factor for path p that is in general complex and frequency dependent, d_p is the length of the path, and $v = c / \sqrt{\epsilon_r}$ with c speed of light and ϵ_r dielectric constant. The attenuation caused by lossy cables is represented by $G(f, d_p)$ which increases with frequency and distance. A simplified model that uses a small number of parameters can be obtained by rewriting (13) as follows

$$(14) \quad G_{CH}^+(f) = A \sum_{p=1}^{N_p} g_p e^{-j \frac{2\pi d_p}{v} f} e^{-(a_0 + a_1 f^K) d_p}, \quad 0 \leq B_1 \leq f \leq B_2,$$

where the parameter A allows adding an attenuation to the frequency response, while the parameters a_0, a_1, K, N_p are chosen to adapt the model to a specific network. This model can realistically represent a true frequency response, i.e., a measured frequency response by appropriate fitting of the parameters [6]. It should be noted that although (14) is derived from the consideration of propagation effects [6], it represents a parametric model to be used for fitting of measured frequency responses.

In order to obtain a statistical model we propose to add some statistical properties to the CTF described in (14) [29]. The idea is to assume the reflectors (that generate the paths) to be placed over a finite distance interval and to be located according to a Poisson arrival process with intensity Λ [m^{-1}]. The maximum network length is equal to L_{\max} . With this model the number of paths has a Poisson distribution with mean $L_{\max} \Lambda$, while the inter-arrival path distances are independent and exponentially distributed with mean $1/\Lambda$.

The path gains g_p are in general complex and they represent the result of the product of several transmission and reflection factors. A possibility is to model them as independent complex random variables with amplitude that is log-normal distributed and with uniform phase in $[0, 2\pi]$. The log-normality is a plausible assumption since each path gain is the product of many transmission and reflection coefficients which as a log-normal distribution as the number of factors goes to infinity. Another possible model is to consider the path gains to be real and uniformly distributed as it was done in [29].

The other parameters a_0, a_1, K are assumed to be constant. K can be chosen to be either smaller or even larger than 1. A value larger than one accounts for a higher decrease of the path loss as the frequency increases. a_0 and a_1 can be chosen to adapt the channel path loss profile such that it matches measured profiles as described in the following.

The **complex CIR** $g_{CH}^+(t)$ can be obtained by the inverse Fourier transform of (13) (or numerically via the inverse discrete Fourier transform), while the real impulse response can be obtained as follows

$$(15) \quad g_{CH}(t) = 2 \operatorname{Re}\{g_{CH}^+(t)\}.$$

It should be noted that the impulse response depends on how we band limit the CTF. That is, according to the definition in (13), the channel is filtered with a rectangular band pass filter. Other windows in frequency can be chosen. No significant differences are obtained provided that the transmitted signal has a spectrum well confined in (B_1, B_2) .

An interesting case of practical interest is when we assume $K=1$. In this case the impulse response can be obtained in closed form. This allows to easily generate a channel realization (corresponding to a realization of the random parameters N_p, g_p, d_p) as follows

$$(16) \quad g_{CH}^+(t) = A \sum_{p=1}^{N_p} g_p e^{-a_0 d_p} \frac{a_1 d_p + j2\pi(t - d_p / \nu)}{(a_1 d_p)^2 + 4\pi^2(t - d_p / \nu)^2} (e^{j2\pi B_1(t - d_p / \nu) - a_1 B_1 d_p} - e^{j2\pi B_2(t - d_p / \nu) - a_1 B_2 d_p}).$$

The impulse response can be truncated in a window that contains most of the energy, say 95%.

5.1 Statistical Characterization

We are now interested in the statistical characterization of the channel modelled as in Section 5. In particular we study the first order statistics of both the frequency response in (14) and the impulse response in (15). They clearly depend on the choice of the parameters and the distribution of the number of paths, the path gains and the path delays. In general, for N_p that goes to infinity the real and imaginary part of both the frequency response and the impulse response tend to be Gaussian distributed according to the central limit theorem.

When showing numerical results in Section 5.1, we assume that the path delays are drawn from a Poisson arrival process, i.e., the inter-arrival path delays are independent and exponentially distributed with mean $1/\Lambda$, and the path gains are independent and uniformly distributed in $[-1, 1]$. With these assumptions and the parameters used, the analysis shows that $G_{CH}^+(f)$ is (at a certain frequency f) circularly symmetric Gaussian, with amplitude that is Rayleigh distributed, and square amplitude that is exponentially distributed. Furthermore, the mean is zero, and the power is equal to the **average (expected) path loss** that is defined as follows

$$(17) \quad PL(f) = E[|G_{CH}(f)|^2].$$

It can be computed in closed form, which yields

$$(18) \quad PL(f) = A^2 \frac{\Lambda}{3} \frac{1 - e^{-2L_{\max}(a_0 + a_1 f^K)}}{(2a_0 + 2a_1 f^K)(1 - e^{-\Lambda L_{\max}})}.$$

The shape of the path loss as a function of frequency depends on the choice of the parameters a_1, K, L_{\max} . While the path loss at zero frequency $PL(0)$ depends on a_0, Λ, L_{\max} . Again, by increasing a_1 and K we can increase the concavity of the path loss profile. The remaining parameters are chosen to scale the resulting profile to the desired values.

Another interesting quantity is the **channel energy**

$$(19) \quad E_{CH^+} = \int_{B_1}^{B_2} |G_{CH}^+(f)|^2 df.$$

The channel energy represents the **average channel gain**. Assuming that the input signal and the noise have constant power spectral density respectively equal to P_x and N_0 , i.e., they are white, the channel energy is related to the **signal-to-noise ratio** as follows

$$(20) \quad SNR = E_{CH^+} \frac{P_x}{N_0}.$$

When $K = 1$ the channel energy can be computed in closed form yielding

$$(21) \quad E_{CH^+} = A^2 \sum_{p1, p2}^{N_p} g_{p1} g_{p2} e^{-a_0(d_{p1}+d_{p2})} \frac{a_1(d_{p1}+d_{p2}) + j2\pi((d_{p2}-d_{p1})/\nu)}{(a_1(d_{p1}+d_{p2}))^2 + 4\pi^2((d_{p2}-d_{p1})/\nu)^2} \\ \times (e^{j2\pi B_1((d_{p2}-d_{p1})/\nu) - a_1 B_1(d_{p1}+d_{p2})} - e^{j2\pi B_2((d_{p2}-d_{p1})/\nu) - a_1 B_2(d_{p1}+d_{p2})}).$$

The channel energy, and therefore the SNR, is a random variable that assuming the Poisson path arrival model with uniformly distributed path gains, is log-normally distributed as shown in the next section.

Now looking at the CIR, the numerical results of the next Section show that the amplitude is Nakagami distributed, the square amplitude is Gamma distributed and the phase is not referable to a known distribution.

An important “time domain” parameter is the **root mean square (rms) delay spread** σ_τ . It is defined for a given channel realization as [30]

$$(22) \quad \sigma_\tau = \sqrt{\frac{\int_0^\infty (t - m_\tau)^2 |g_{CH}(t)|^2 dt}{\int_0^\infty |g_{CH}(t)|^2 dt}} = \sqrt{\frac{\int_0^\infty (t - m_\tau)^2 |\text{Re}\{g_{CH}^+(t)\}|^2 dt}{\int_0^\infty |\text{Re}\{g_{CH}^+(t)\}|^2 dt}},$$

where the **mean excess delay** is

$$(23) \quad m_\tau = \frac{\int_0^\infty t |g_{CH}(t)|^2 dt}{\int_0^\infty |g_{CH}(t)|^2 dt} = \frac{\int_0^\infty t |\text{Re}\{g_{CH}^+(t)\}|^2 dt}{\int_0^\infty |\text{Re}\{g_{CH}^+(t)\}|^2 dt}.$$

Since the channel is statistical, the delay spread is also a random variable. The numerical results of the next section show that it is log-normally distributed for the given statistics of the path delays and path gains.

Finally, the numerical results will show that those realizations that are characterized by a high delay spread are also characterized by a low channel energy therefore by a higher attenuation. This is confirmed also by measurements.

5.2 Channel Generation and Numerical Characterization

The freedom in choosing the parameters allows obtaining channels with different statistics. The approach herein followed is to first fix the maximum path length and path arrival rate to a certain reasonable value. Then, we fix the parameter K which mostly determines the shape (concavity) of the average path loss and the path loss slope at high frequencies. Then, we fix the remaining two parameters a_0, a_1 to obtain the desired path loss at zero frequency and at the stop frequency. In particular, we can normalize the channel such that the average path loss at zero frequency is equal to one. The parameter a_0 can therefore be chosen to satisfy the following relation

$$(24) \quad \sqrt{\frac{\Lambda (1 - e^{-\Lambda L_{\max}})}{3 \cdot 2a_0}} (1 - e^{-2L_{\max} a_0}) = 1.$$

Then, we can offset it by a factor A to obtain the desired average path loss at zero frequency and fit values obtained from measurements [31]-[32].

As stated in Section 5.1, we assume that the path delays are drawn from a Poisson arrival process, i.e., the inter-arrival path delays are independent and exponentially distributed with mean $1/\Lambda$, and the path gains are independent and uniformly distributed in $[-1, 1]$.

An example of significant practical relevance is obtained by considering the band 0-100 MHz, that is the one considered in the OMEGA project. So we have $B_1 = 0$ and $B_2 = 100$ MHz. Then we choose $K = 1$, Λ equal to $0.2 \text{ [m}^{-1}\text{]}$, maximum network length L_{\max} equal to 800 m. Then, to obtain path losses similar to those of classes 2-5 of Section 3.1, we set $a_0 = 0.3 \times 10^{-2}$, and $a_1 = 4 \times 10^{-10}$. Finally, the CTF is further attenuated such that the path loss, at zero frequency, is equal to the desired value, e.g. -40 dB.

In Figure 48 we report an example of CIR and frequency response for the parameters above listed. The impulse response obtained in closed form is truncated to $5.56 \mu\text{s}$.

The statistical characterization of the frequency and impulse response has been done over 1000 realizations generated with the above parameters. Regarding the frequency response, in Figure 49 and Figure 50 we report the probability density function (PDF) and the cumulative distribution function (CDF) of the frequency response amplitude for a given frequency f_0 . The amplitude is well fitted with a Rayleigh distribution that has PDF equal to

$$(25) \quad p_{|G(f_0)|}(a) = \frac{a}{b_0^2} e^{-\frac{a^2}{2b_0^2}},$$

where the parameter b_0 is linked to the path loss, i.e. $PL(f_0) = 2b_0^2$.

In Figure 51 and Figure 52 we show the PDF and CDF of the square amplitude of the frequency response for a given frequency f_0 . It is exponentially distributed.

In Figure 53 we show the expected path loss obtained by the Monte Carlo simulation and the analytical one computed according to (18).

In Figure 54 and Figure 55 we report the PDF and the CDF of the channel energy. As it can be seen it is log-normal.

Regarding the impulse response, in Figure 56 and Figure 57 we report the PDF and the CDF of the impulse response amplitude for a given time instant t_0 . It is well fitted by a Nakagami distribution. In Figure 58 and Figure 59 we show the PDF and the CDF of the square amplitude of the impulse response. It is Gamma distributed.

The mean value of the delay spread (averaged over the realizations) equals 81.56 samples ($0.41 \mu\text{s}$) while the standard deviation is $0.06 \mu\text{s}$ (the channel impulse response is sampled at 200 MHz). Figure 60 and Figure 61 show its PDF and CDF respectively. It can be described by a lognormal distribution. As it can be seen, σ_τ spans from 49 samples ($0.25 \mu\text{s}$) to 123 samples ($0.62 \mu\text{s}$). As illustrated in Section 2.3.2 and in [32], similar values of σ_τ have been obtained by indoor measurement campaigns.

Finally in Figure 62 we report one hundred realizations of the normalized delay spread (normalized with respect to its maximum value) and the normalized channel energy. The figure shows that those realizations that are characterized by a high delay spread are also characterized by a low channel energy therefore by a high attenuation.

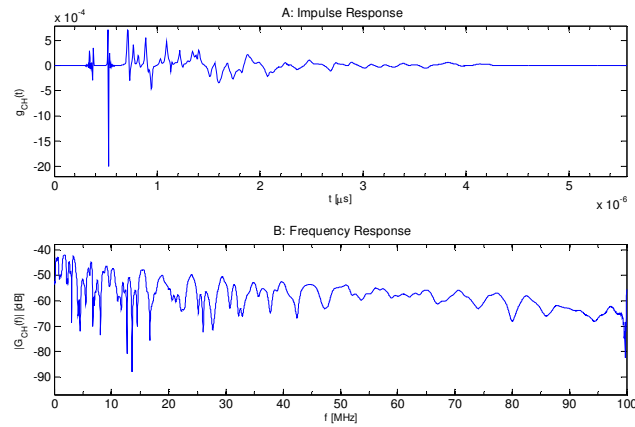


Figure 48: Realization of a PLC channel impulse response and frequency response.

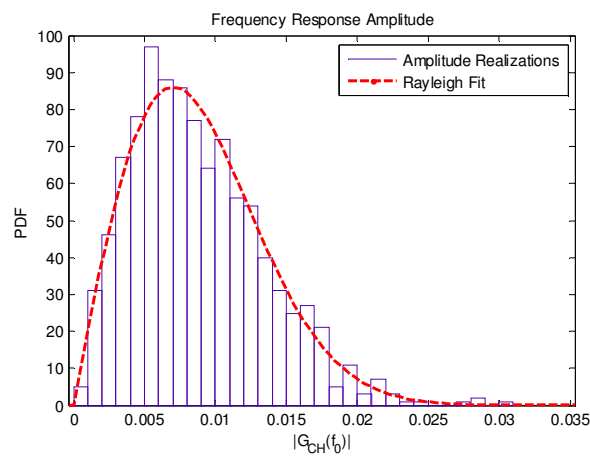


Figure 49: PDF of the frequency response amplitude for a given frequency f_0 .

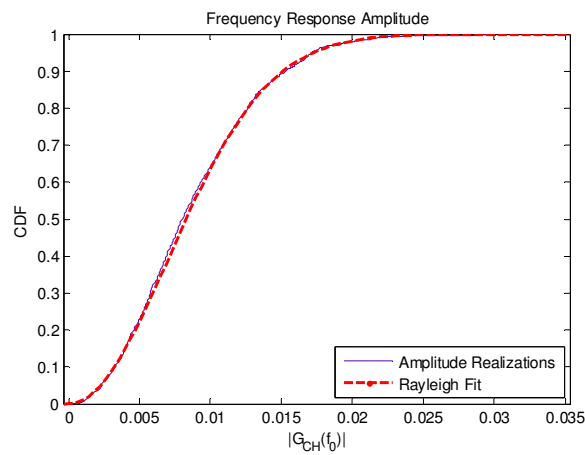


Figure 50: CDF of the frequency response amplitude for a given frequency f_0 .

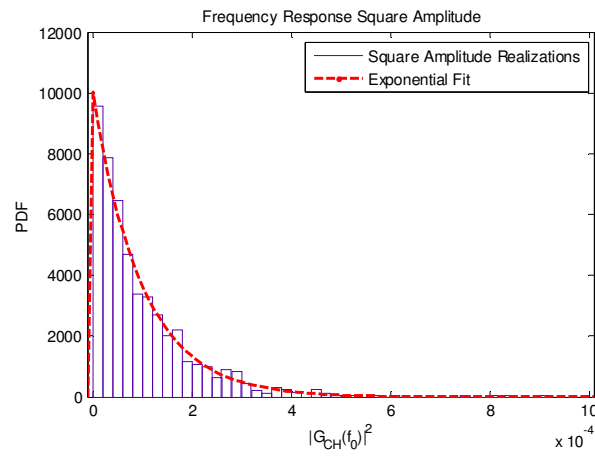


Figure 51: PDF of the frequency response square amplitude for a given frequency f_0 .

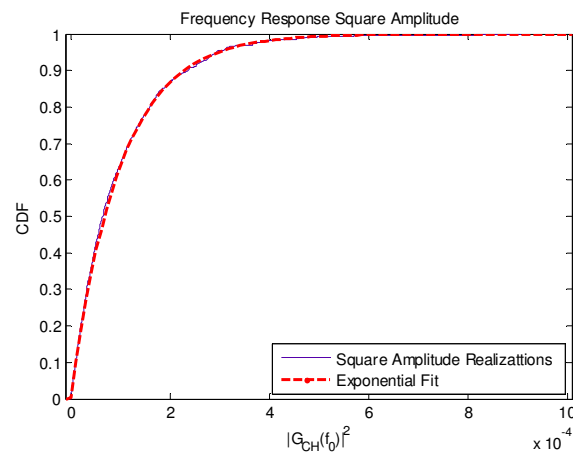


Figure 52: CDF of the frequency response square amplitude for a given frequency f_0 .

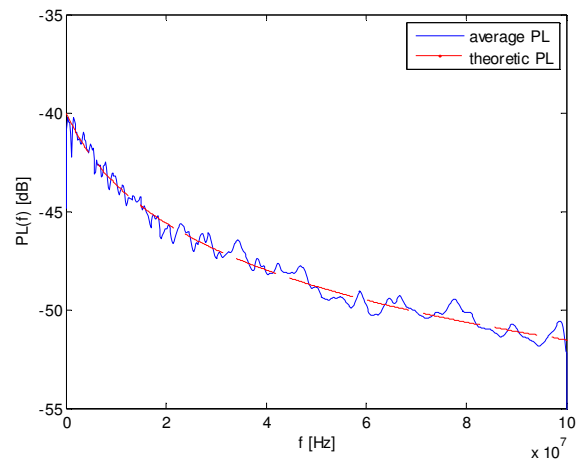


Figure 53: Theoretical and simulated expected path loss.

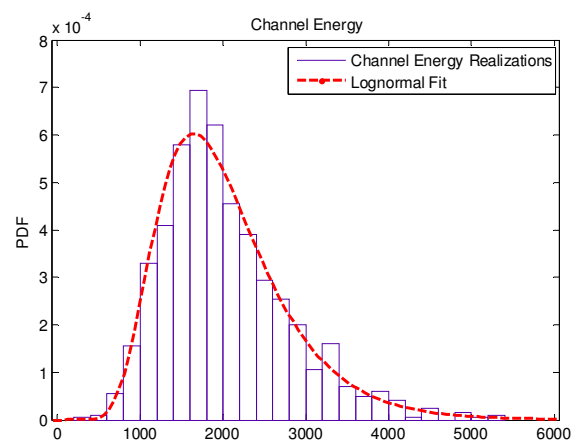


Figure 54: PDF of the channel energy.

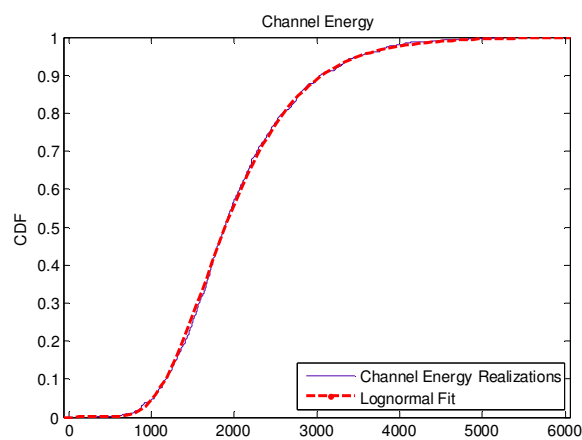


Figure 55: CDF of the channel energy.

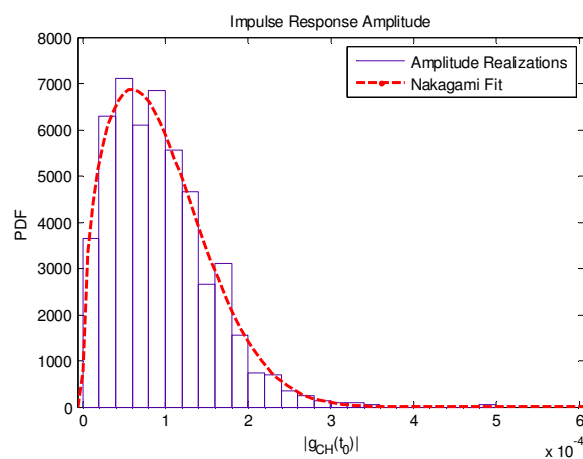


Figure 56: PDF of the impulse response amplitude for a given time instant t_0 .

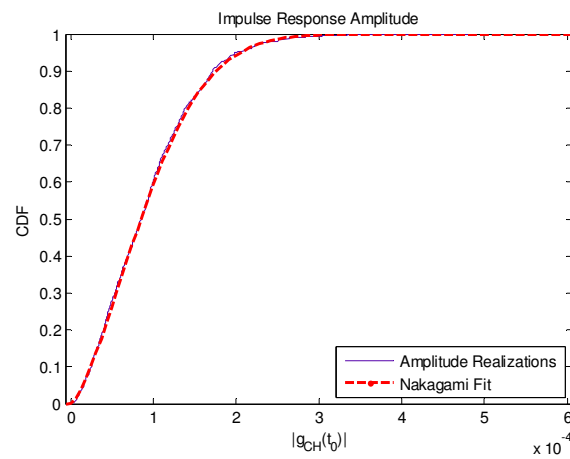


Figure 57: CDF of the impulse response amplitude for a given time instant t_0 .

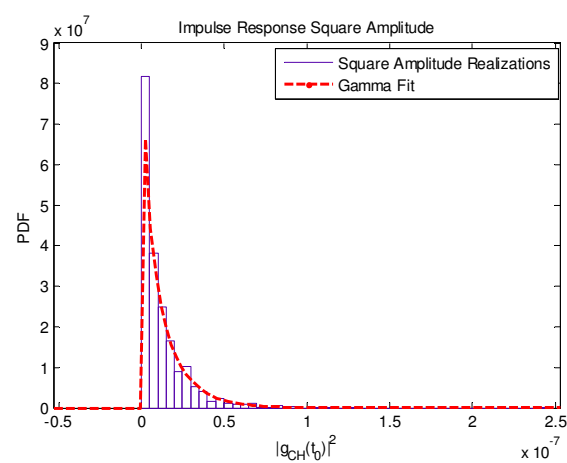


Figure 58: PDF of the impulse response square amplitude for a given time instant t_0 .

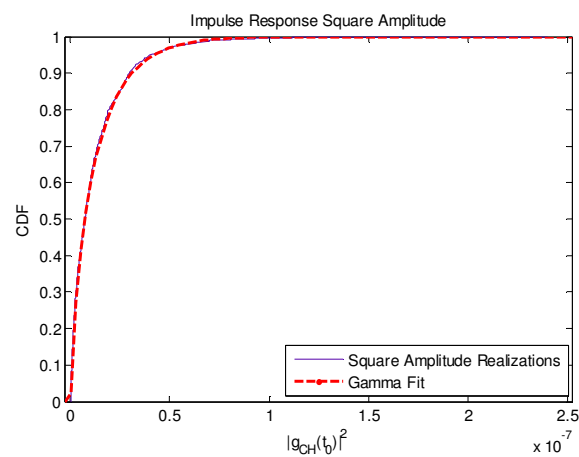


Figure 59: CDF of the impulse response square amplitude for a given time instant t_0 .

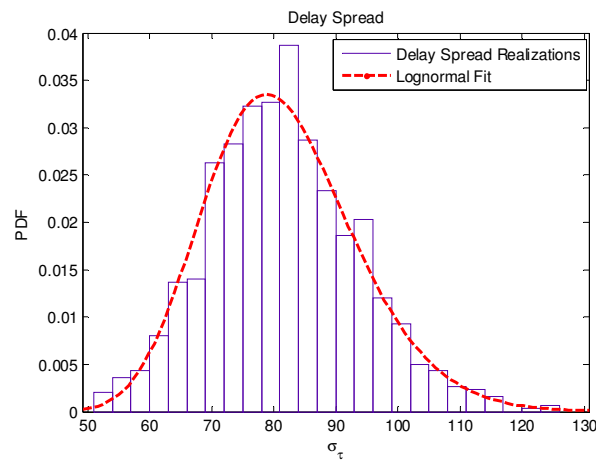


Figure 60: PDF of the delay spread

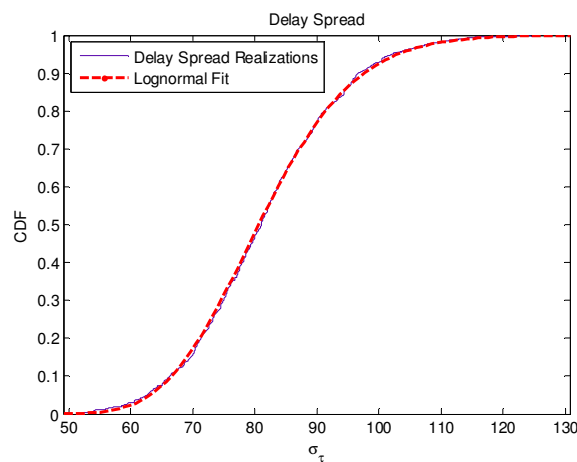


Figure 61: CDF of the delay spread.

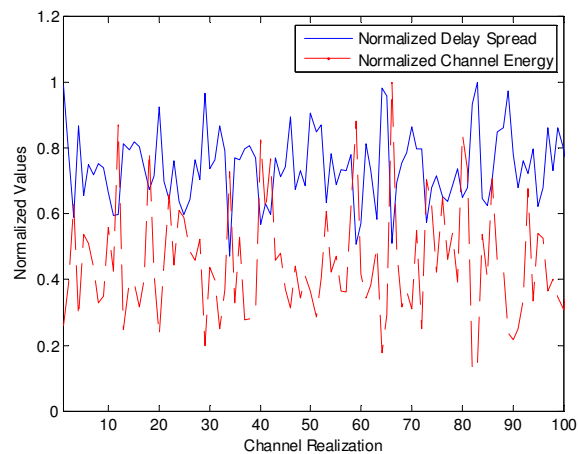


Figure 62: Normalized delay spread and channel energy for one hundred channel realizations.

5.3 Matlab Code

The statistical channel model herein described that starts from an analytical expression of the CTF can be easily realized by a computer simulation. MATLAB functions that implement the model as well as updates can be downloaded from <http://www.diegm.uniud.it/tonello>.

Below we report the source code for the simplest case herein described that assumes the parameter $K=1$. An impulse response for the parameters used in Section 5.2 can be generated by calling the function as follows

```
[g_ch C0]= GEN_PLC_CHAN(100e6, 0.3e-2, 4e-10, 0.2, 800, 5.56e-6);
```

With this choice of the parameters we can realize path loss profiles similar to those of Class 2-5 of Section 3.2.1.

```
% -----
% [g_ch C0]=GEN_PLC_CHAN(B2,a0,a1,lambda,LMAX,CHANNEL_DURATION)
% -----
% Copyright:      Andrea M. Tonello - tonello@uniud.it
%                Dipartimento di Ingegneria Elettronica, Gestionale e Meccanica
%                Università degli Studi di Udine - Udine - Italy
% Release:       1.0
% Date:          December 15, 2008
%
% Updates can be downloaded from www.diegm.uniud.it/tonello
%
% Copyright Notice: This software is freely usable for non commercial activities provided that Reference 1 is cited. Any use has
% to comply with the copyright terms. Any modification and/or commercial use has to be authorized by the copyright owner.
%
% Reference 1:    A.M. Tonello, "Wideband Impulse Modulation and Receiver Algorithms for Multiuser Power Line
%                Communications," EURASIP Journal on Advances in Signal Processing, vol. 2007, pp.1-14.
%
% -----
% Accepts as inputs:
%
% 1) B2          : Stop frequency in Hertz. B1 is set to 0.
% 2) a0, a1      : Parameters of the frequency dependent attenuation portion. k is set to 1.
% 3) lambda      : Intensity of the Poisson arrival process in 1/meters.
% 4) LMAX        : Maximum path distance in meters.
% 5) CHANNEL_DURATION : Channel duration in seconds with maximal value of 10 micro seconds. The returned CIR is
%                truncated by finding the highest energy window of duration CHANNEL_DURATION.
%
% Returns as outputs:
% 1) The complex CIR g_ch(nTc) with a sampling period equal to Tc=1/(2*B2). The channel is normalized such that the PL [dB]
%    at zero frequency is zero.
% 2) If C0==1 the generated impulse response is not valid. Otherwise if C0==0 the CIR is valid.
%
% -----

function [g_ch C0]= GEN_PLC_CHAN(B2,a0,a1,lambda,LMAX,CHANNEL_DURATION)

    if CHANNEL_DURATION > 10e-6, error('maximal channel duration 10us'), end

    B1 = 0; C0 = 0; Tc = 1/(2*B2); epsr = 1.5; c = 3e8;

    % The CIR is initially generated between -TchL and TchR
    TchL = ceil(10e-6/Tc)*Tc; TchR = ceil(10e-6/Tc)*Tc; t = [-TchL:Tc:TchR];

    % First ray is set at d0 with exponential distribution
    d0 = -1/lambda*log(rand); dist_r = d0;

    n = 1;
```

```

while ( dist_r < LMAX )

    d(n) = dist_r; dist_r = dist_r-1/lambda*log(rand); n = n+1;

end

Np = length(d);

if Np==0, C0 = C0+1, end

d = sort(d); tau = d/c*epsr;

% Path gains are uniformly distributed
g = (2*rand(1,Np))-1;

% If k==1 the CIR is generated in the time domain
g_ch = zeros(1,length(t));

for n=1:Np

    g_ch = g_ch+g(n)*exp(-a0*d(n)).*(a1*d(n)+j*2*pi*(t-tau(n)))./(a1^2*d(n)^2+4*pi*pi*(t-tau(n)).^2 ).*...
        (exp( j*2*pi*B1*(t-tau(n))-a1*B1*d(n) )-exp( j*2*pi*B2*(t-tau(n))-a1*B2*d(n) ) );

end

% Normalization factor derived from average path loss at zero frequency
K = (1/3*lambda)*(1-exp(-lambda*LMAX))./(2*a0).*(1-exp(-2*LMAX*(a0)));

K = 1/sqrt(K);

g_ch = K*g_ch*Tc;

% Windowing the impulse response to obtain a CIR with duration CHANNEL_DURATION
w = ceil(CHANNEL_DURATION/Tc); tmp = abs(g_ch).^2; MAX_IST = length(tmp)-w+1; clear tmp;

Energy = zeros(1,MAX_IST);

for n=1:MAX_IST,Energy(n)=g_ch(n:n+w-1)*g_ch(n:n+w-1)'; end

[maxx pos]=max(Energy);

g_ch=g_ch(pos: pos + w - 1);

end

```

6 Channel Transfer Function Model based on Transmission Line Theory

6.1 Introduction

Transfer function of an electrical system is the ratio between voltage at the output and the voltage at the input of the electrical system, when the input voltage has **sinusoidal** form. It tells us the level of attenuation or amplification of the electrical system (i. e. amplitude response) and the delay of change of the output voltage according to the input voltage (i. e. phase response). Transfer function is frequency dependant, therefore it has to be calculated or measured for each frequency in the desired frequency range.

6.2 Power Cable

Standard three conductor cable NYM as shown in figure Figure 63 was evaluated.

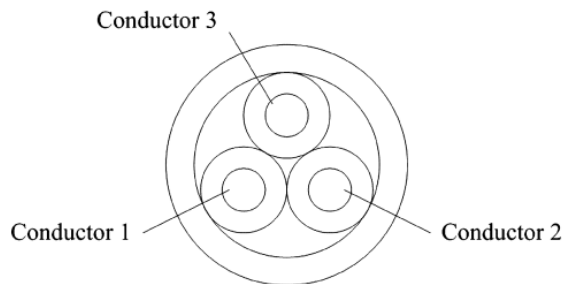


Figure 63: Evaluated cable.

Cable properties:

- conductor material: copper
- insulating material: PVC
- conductor cross-section: 2.5 mm²
- cable length: 10 m

6.3 Electrical Model of the Cable

The cable is treated as a transmission line since its length is much larger than 1/4 of minimal wavelength of the electrical signals conducted by the cable.

$$\text{maximal frequency} = 100 \text{ MHz}$$

$$\text{minimal wavelength} = \frac{\text{speed of light}}{\text{maximal frequency}} = \frac{3 \cdot 10^8 \text{ m/s}}{100 \cdot 10^6 \text{ 1/s}} = 3 \text{ m}$$

The cable is modeled as a cascade of cable segments (see Figure 64). A distributed parameter model from the article [34] is used.

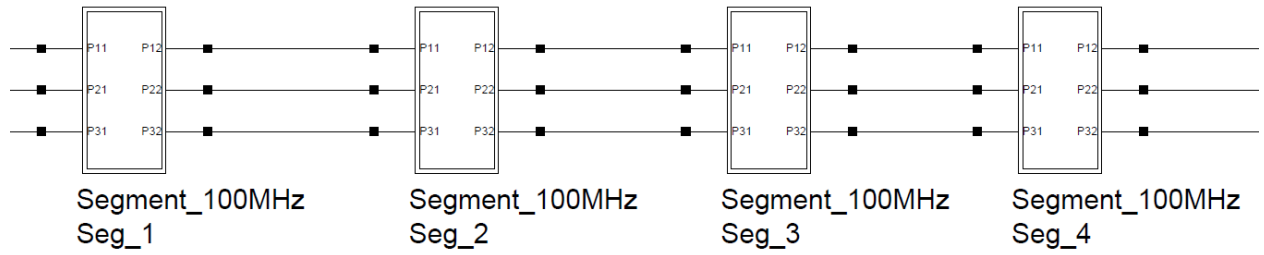


Figure 64: Evaluated cable.

Cable segment model is shown in Figure 65. The length of each cable segment is 1/100 of the minimal wavelength, that is 0.033 m. The cable segment model is valid for frequencies up to 100 MHz.

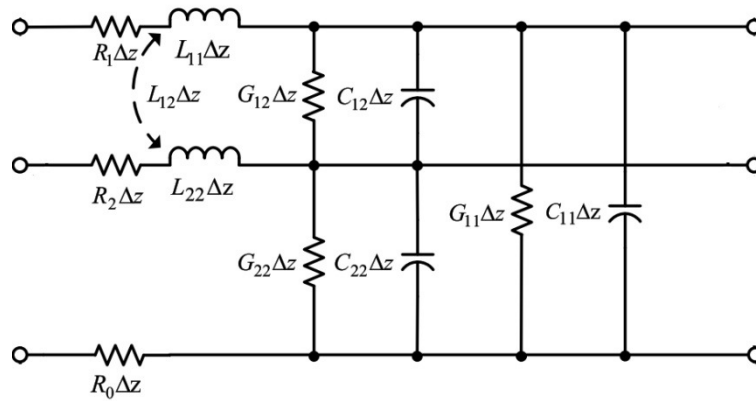


Figure 65: Cable model.

The distributed per unit length parameters R , L , C and G are calculated from the equations and measurements from articles [33], [34], [35]. For further explanation of the equations see the articles.

a) Resistivity per unit length (Ω/m)

$$(26) \quad R_w = \frac{1}{2\pi r_w \sigma \delta} \quad \text{resistivity per unit length}^3 [34]$$

$$(27) \quad \delta = \frac{1}{\sqrt{\pi f \mu \sigma}} \quad \text{skin effect contribution [32]}$$

b) Inductance per unit length (H/m)

$$(28) \quad L_{ii} = \frac{\mu}{2\pi} \ln \left(\frac{d_{i0}^2}{r_{wi} r_{w0}} \right) \quad \text{self inductance of a wire [32]}$$

$$(29) \quad L_{ij} = \frac{\mu}{2\pi} \ln \left(\frac{d_{i0} d_{j0}}{d_{ij} r_{w0}} \right) \quad \text{mutual inductance between two wires [32]}$$

³ Resistivity per unit length is multiplied by factor 1.3 to obtain results given in [35]

c) Capacitance per unit length (C/m)

$$(30) \quad C_{pair} = \frac{\pi \varepsilon}{\ln \left[(D/2a) + \sqrt{(D/2a)^2 - 1} \right]} \quad \text{capacitance between two wires [32]}$$

Relative dielectric constant: $\varepsilon_R = 3$ [33]

d) Conductance per unit length (S/m)

Conductance between two wires per unit length is calculated from the data from article [33]. Conductance is approximated with linear function and extrapolated to the frequency of 100 MHz.

6.3.1 Calculated Cable Parameters

The following figures present calculated per unit length parameters:

- resistance of the conductor (R_w),
- self inductance of the conductor (L_{11}),
- mutual inductance between conductors (L_{12}),
- capacitance between a pair of wires (C_{10})
- conductance of the insulator between a pair of wires (G_{10}),

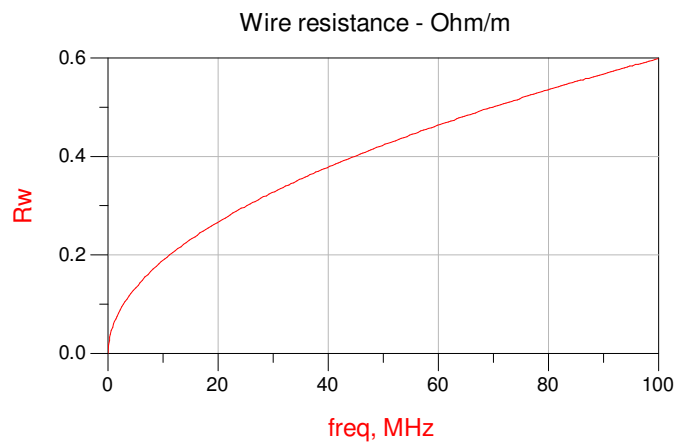


Figure 66: Wire resistance per unit length.

Wire resistance per unit length is frequency dependant because of the skin effect. The proximity effect is not taken into account.



Figure 67: Self inductance of a wire per unit length.

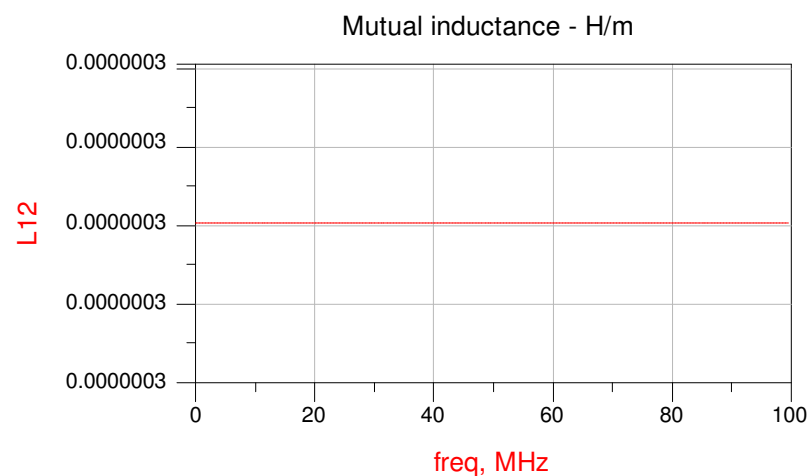


Figure 68: Mutual inductance between wires 1 and 2 per unit length.

The inductances are modeled as independent of frequency. The actual inductance increases at frequencies lower than 5 MHz according to the results from articles [33][35], for higher frequencies remains constant through the whole frequency band. The same holds true for the capacitance between wires.

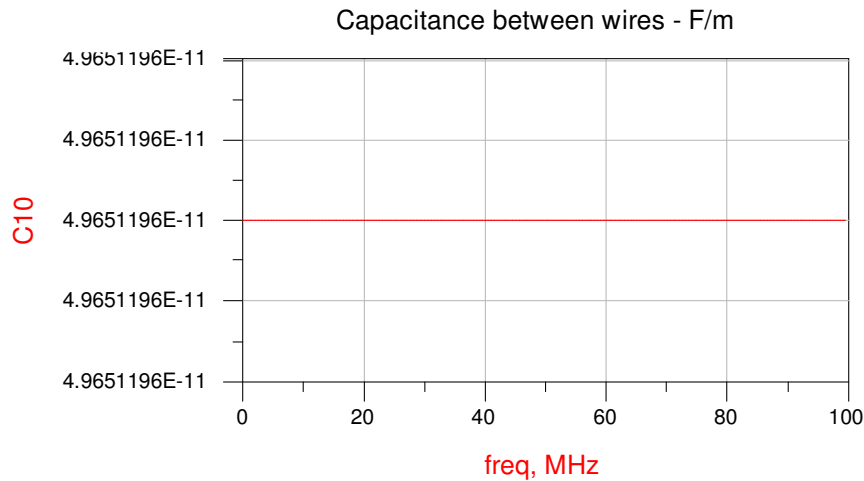


Figure 69: Capacitance between two wires per unit length.

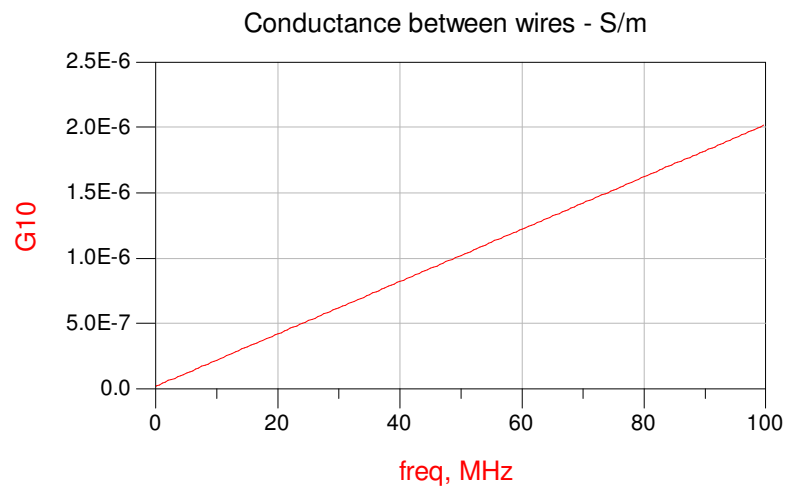


Figure 70: Conductance between two wires per unit length.

Loss of the insulation is modeled as linear function of the frequency according to the article [33] and extrapolated to the frequency of 100 MHz.

6.4 Simulated Results

The calculation was made with the Agilent ADS 2008 computer software. The transfer function is always calculated for one pair of wires, the third wire is grounded. The pair of wires is terminated at both ends with the $50\ \Omega$ resistance. In addition, surge protection device model is added and new transfer function is calculated.

The S-parameter analysis is used. S parameters are calculated and the amplitude of S21 parameter is plotted versus the frequency.

Model of a segment used in ADS 2008 computer software is shown in Figure 71.

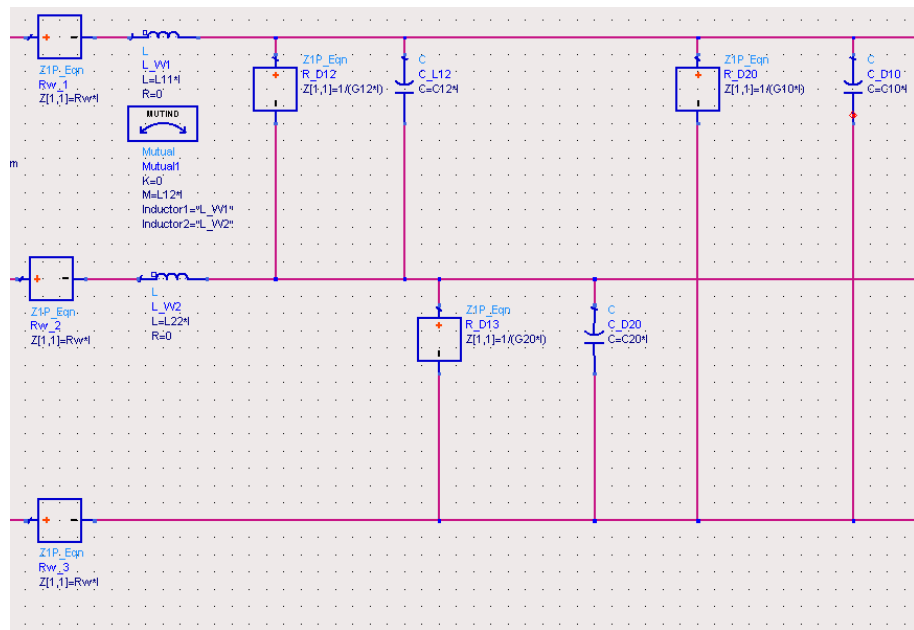


Figure 71: ADS 2008 computer software model

The transfer function following setups were analyzed:

- cable, length 1m and 10m
- cable with surge protection devices attached to both ends, length 1 m and 10 m,
- typical wiring setup without and with surge protection device attached to one end.

6.4.1 Transfer Function of the Cable Without and With Surge Protection Device (SPD)

Two cable lengths, 1 m and 10 m, without and with surge protection devices attached to both ends were analyzed. Surge protection devices were modeled as capacitors, with capacitance 1.95 nF and 14.30 nF. The setup is shown in Figure 72 – capacitance C7 and C8 present surge protection device.

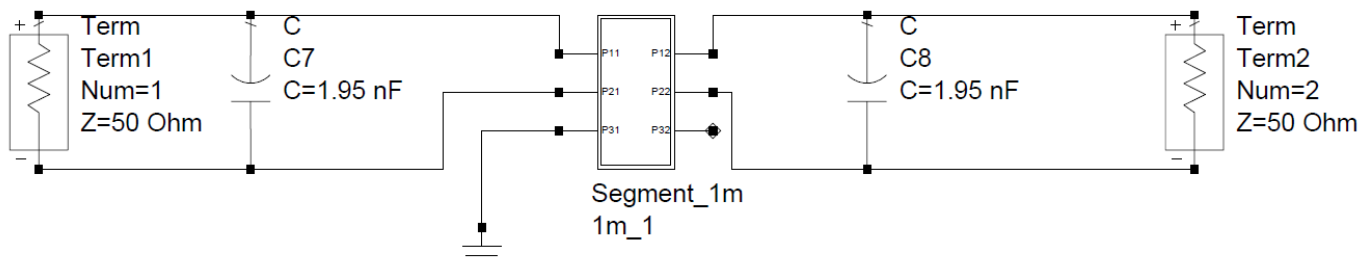


Figure 72: Cable with surge protection devices and PLC modems

Figure 73 to Figure 76 present the calculated results for four setups. Significant distortion of transfer function can be seen when the surge protection devices are attached in comparison with the transfer function without the

attached surge protection devices, which is almost flat and has very small attenuation. It can be seen in Figure 11 that the larger the capacitance of the surge protection device, the higher is the attenuation of the amplitude. The same can be seen in Figure 13 for the 10 m cable setup.

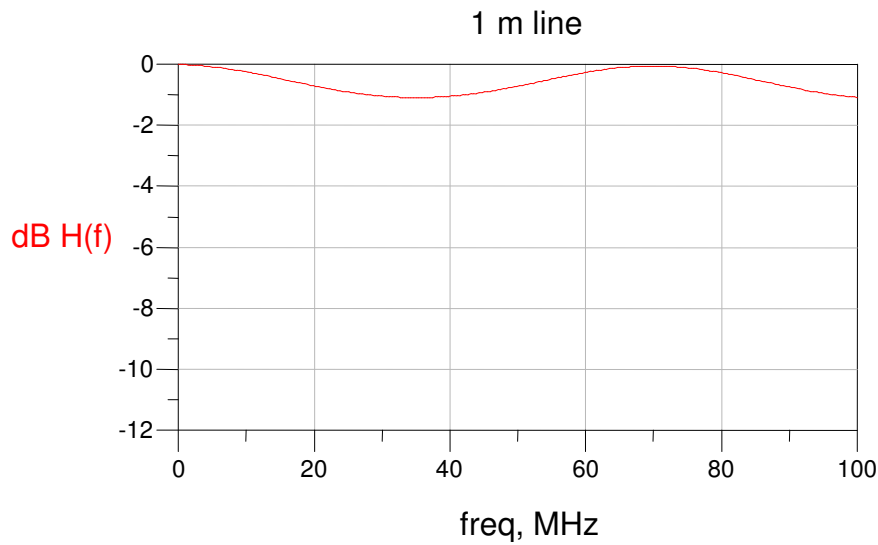


Figure 73: Amplitude response of 1 m cable without surge protection devices

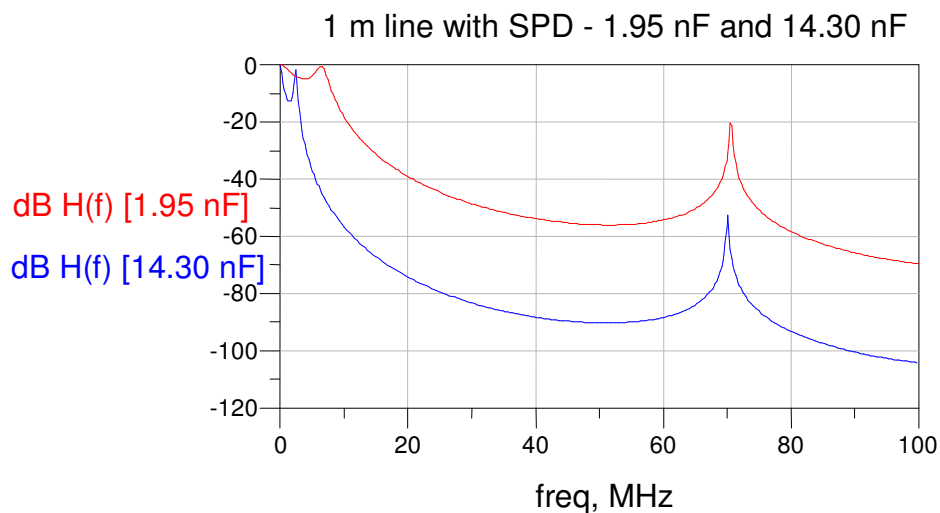


Figure 74: Amplitude response of 1 m cable with surge protection devices

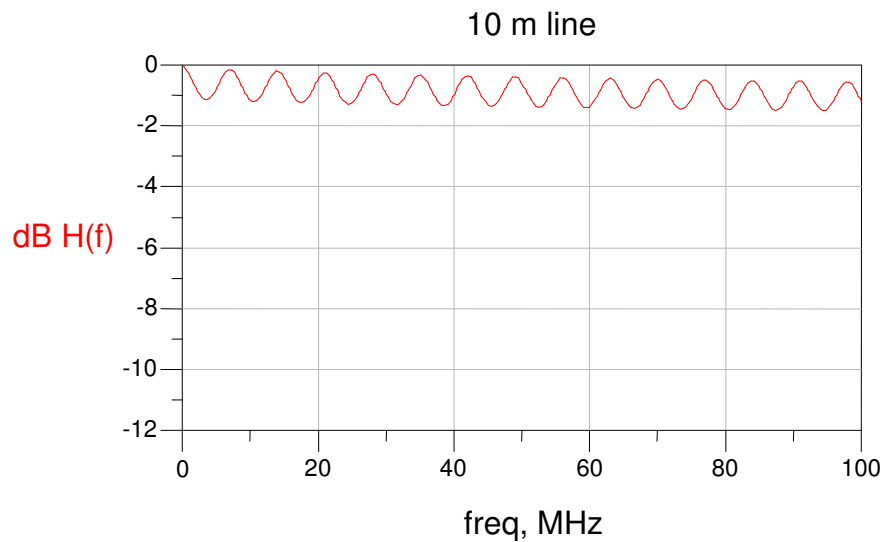


Figure 75: Amplitude response of 10 m cable without surge protection devices

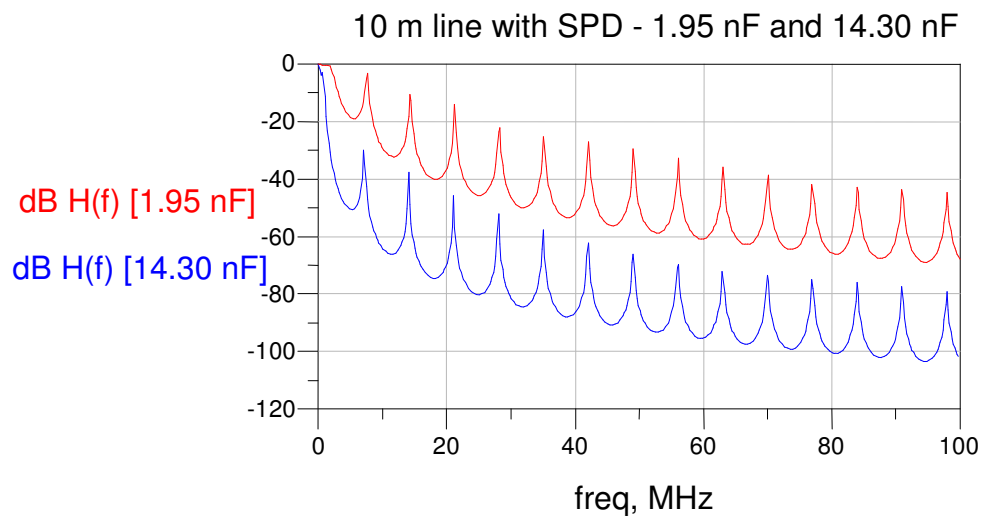


Figure 76: Amplitude response of 1 m cable with surge protection devices

6.4.2 Transfer Function of Typical Wiring

Typical wiring model was analyzed containing three branches, seven power outlets, two lamps, three PLC modems and one typical load. The wiring is presented in Figure 77. The loads were modeled as follows:

Load	Impedance
Lamp	114 Ω
PLC modem	50 Ω
Typical load	12 k Ω + j ω (0.6 mH)

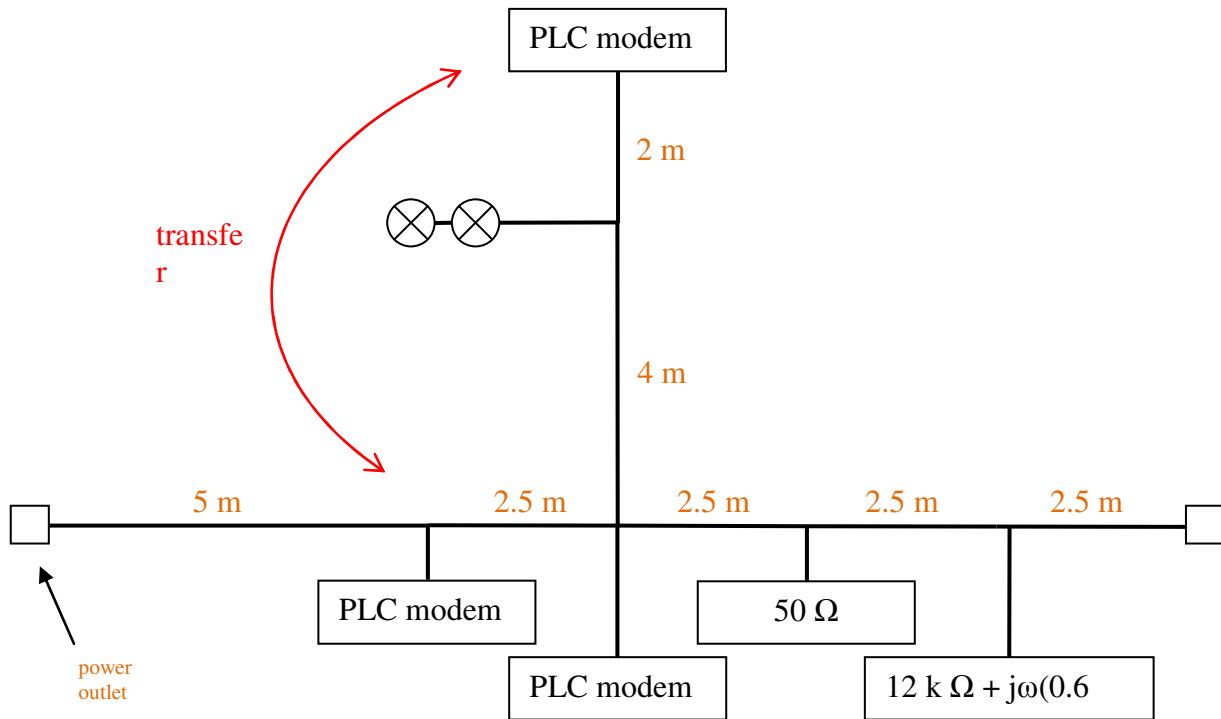


Figure 77: Wiring model

Transfer function is calculated between PLC modem 1 and PLC modem 2 (see Figure 78); without SPD devices (blue graph), with one SPD device attached to the PLC modem 1 (red graph). Yet again can be noticed the distortion and attenuation of the transfer function with the presence of surge protection device even though it is attached only at one end of the path.

Note that the angles and junctions in the wiring introduce reflections. The model used for calculation is simplified and **does not** include the reflections due to the angles and junctions in the wiring. Power outlets are modeled as open line.

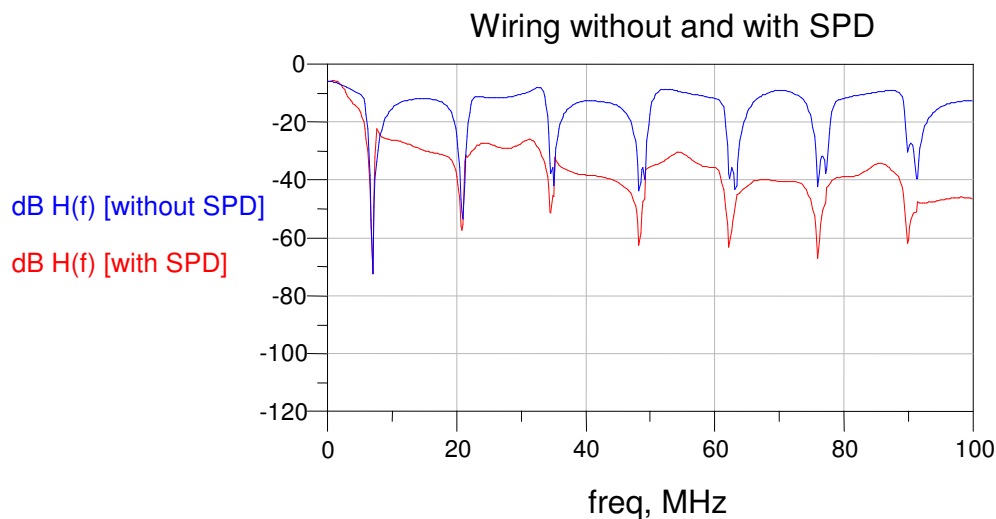


Figure 78: Amplitude response of the wiring without and with surge protection device

The transfer function of the wiring cannot be easily determined since it is dependent of various parameters i.e.:

- length of wires,
- number of branches,
- number of junctions,
- number and degree of angles,
- number and type of loads.

Not only that transfer functions differ in different wiring they also differ between different nodes in the very same wiring. The above figure therefore presents only one possible transfer function of one path, i. e. between PLC modem 1 and PLC modem 2. It is presented only to illustrate the complicated not easily determinable amplitude response.

6.5 Conclusions

Transfer functions are calculated with the data from the literature ([33], [34], [35]). To validate the calculated result a **measurement** of transfer function has to be made as a further study. The measurement has to take into account various types of cables and wiring configurations together with various matched and non-matched loads. A representative wiring has to be determined and its transfer function has to be calculated and measured.

Surge protection devices can significantly distort the transfer function. The main factor is the capacitance of varistors, therefore varistors with small capacitances have to be used.

7 Impulsive noise characterization and modelling

Noise characteristics of an indoor powerline network strongly influence the link capability to achieve high data rates. The appliances shared with PLC modems in the same powerline network generate noises which are stationary, cyclo-stationary or impulsive [36].

Impulsive noise is the main source of interference which causes signal distortions leading to bit errors during data transmission. Origins of impulsive noises are multiple: power switches, power supplies, and generally speaking domestic appliances.

7.1 State of the Art

Several approaches have been followed for characterizing the PLC impulsive noise. In [37][38][39] the proposed models are based on noise classification according to different criteria: duration, bandwidth and inter-arrival between impulses.

The proposed models share the same impulsive noise definition: “unpredictable noises **measured at the receiver side**”. Authors are, consequently, confronted to model thousands of impulsive noises whose plurality would very likely come from the diversity of paths that the original impulsive noise took.

In this section, an innovative modelling approach is applied to impulsive noises which are henceforth studied directly at their sources outputs. Noise at receiver is considered as the noise model at the source filtered by the powerline channel [25][26].

Measuring impulsive noises at source has many advantages:

- Much less noises types are observed.
- Ability to correlate signatures with source generators.
- Much easier classification.

7.2 Impulsive Noise Measurement Campaign

Here, we firstly outline what impulsive noises are measured for the considered domestic devices. Then, the impulsive noise sounder design and the devices used in the measurements are presented.

7.2.1 Measurement Description

The PLC impulsive noises study presented hereby relates to 23 different domestic appliances. The list of studied devices is reported in Table 15.

For each device, different functioning states are first identified, directed arcs are made between connectable statuses, and the impulsive noise associated to each arc (or transition) is measured. Table 15 shows the list of studied devices and their functioning states.

Device name	Statuses
Vacuum cleaner	Off – Soft – High - Turbo
Electric kettle	Off – On
Coffee maker	Off – On
Electric heating	Off – On
Electric carving knife	Off – On
Paint burner	Off – Soft – High
Computer screen	Off – On
Iron	Off – On
Refrigerator	Off – On – Open/Close door
Incandescent lamp	Off – On
Fluorescent and Neon lights	Off – On
Residential Gateway	IP Phone pick up – IP phone put down
Washing machine	Off – On – Washing cycle start – Washing cycle stop – Rinsing start
Videorecorder (VCR)	Off – On
Microwave	Off – On
Can opener	Off – On
Laptop	PC turn off – PC turn on
Induction hob	Off – On
Food processor	Off – Soft – High
Hair dryer	Off – Soft – High - Turbo
Set-top-box	No Impulsive noises
Hair clippers	Off – On – Height change
TV	Off – On
Computer case	Off – On

Table 15: List of devices and states generating by impulsive noise

Note that this table only reports states that lead to impulsive noise apparition. For example, for the case of the Residential Gateway, only statuses related to the IP Phone connected to it are considered as they are the only ones likely to generate impulsive noises. Other statuses such as starting period, active, or stand by modes are omitted as not accompanied by impulsive noises.

Impulsive noises for Off→On and On→Off states transitions respectively correspond to electric switch activation and deactivation. Electrical switches appear in various forms:

- Electrical switch on the wall.
- Off/On electrical switch on the device.
- Security pushbutton on the device.

Other impulsive noises that can be generated by any electrical device, but do not refer to any state transition, are those associated to plugging in or unplugging electrical plugs into network sockets. These noises are frequently present in the powerline network and are also considered and analyzed.

It remains to be mentioned that for certain devices, such as refrigerator and electric heating appliance, the On→Off and Off→On transitions are also activated by internal thermostatic control. These types of thermostat-generated impulsive noises are studied too.

7.2.2 Measurement Hardware

Impulsive noise measurements were carried out in the time domain, by means of a digital oscilloscope, as shown in the block diagram of the Figure 79.

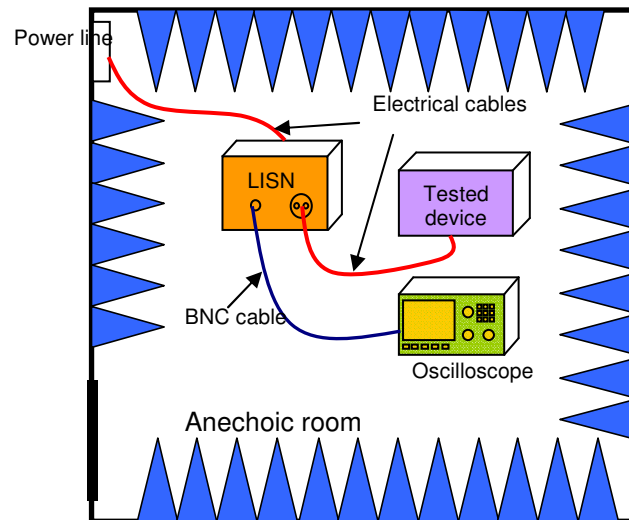


Figure 79: Measurement hardware of impulsive noise at source.

The Device Under Test (DUT), is isolated from the remaining electrical network by means of a Line Impedance Stabilization Network (LISN). The complete experimental setup is put into an anechoic room in order to avoid external radio coupling.

For each device, impulsive noises are recorded over a 50 ms duration when their amplitudes exceed the trigger level. This level depends on the amplitude of the device stationary noise, and thus varies from one device to another.

The noise is recorded on two scope channels with different sensitivities. This made it possible to have, simultaneously, a good sensitivity for the low-amplitude noises and not to clip the strong-amplitude ones.

As for the sampling rate, it was fixed to 250 Msamples per second, leading to an observed frequency band of 125 MHz.

7.3 Impulsive Noise Characterization

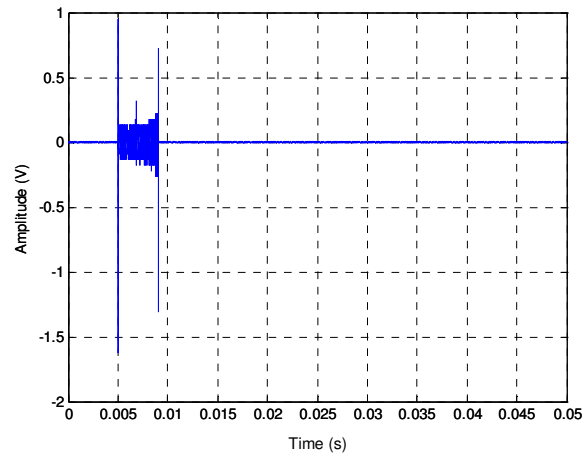
In this section, general observations on measured impulsive noises at source are firstly presented. After that, an impulsive noise classification scheme is proposed according to their in-device generator.

7.3.1 General Observations

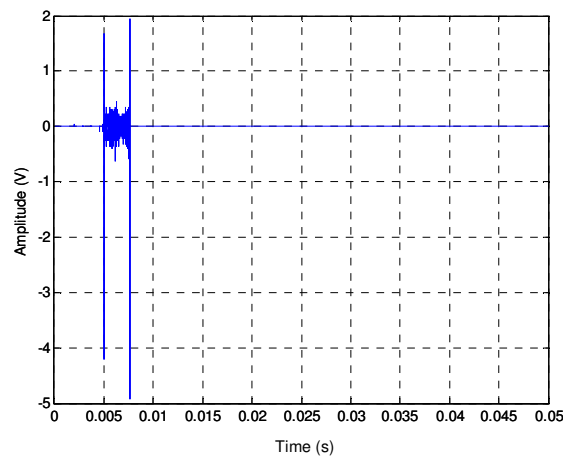
In this section a set of observations and remarks gathered during measurements are listed:

- Any given event (state transition) generating impulsive noise always corresponds to the same signature with small amplitude and total duration⁴ variations. Figure 80 illustrates three measured impulsive noises associated to a same turning off event (electric switch On→Off) with the coffee maker, electric heating, and vacuum cleaner devices.

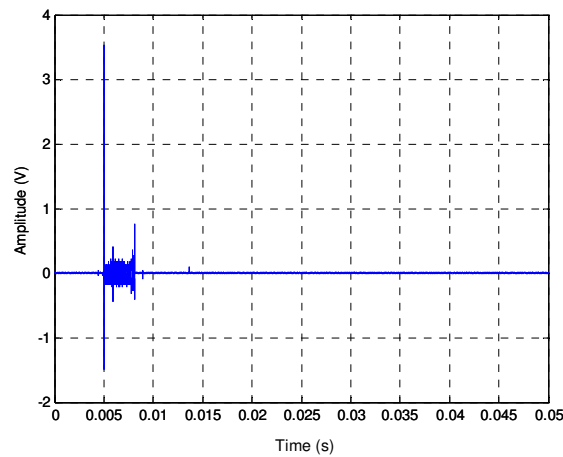
⁴ The total duration of an impulsive noise is the duration from the first time sample of its first impulse to the last time sample its last impulse.



(a) Coffee maker turning Off event



(b) Electric heating turning Off event

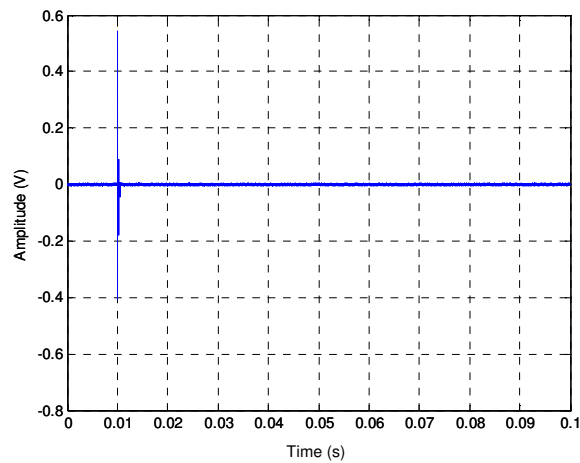
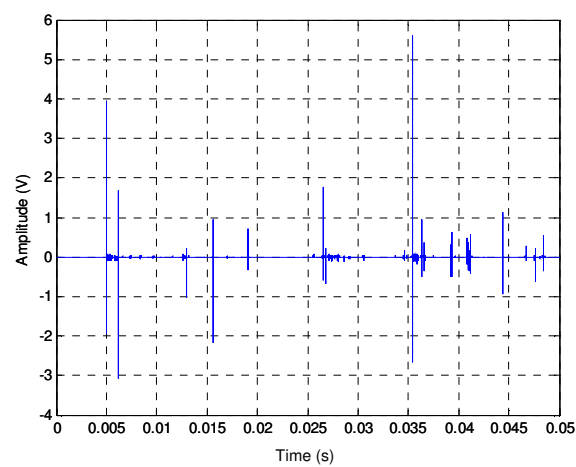
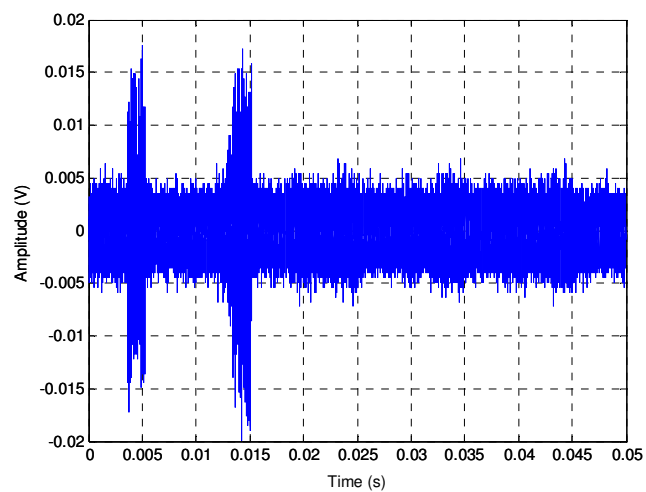


(c) Vacuum cleaner turning Off event

Figure 80: Turning Off event impulsive noises for different devices:

(a) Coffee maker, (b) Electric Heating, (c) Vacuum cleaner.

- Depending on the source, measured impulsive noises contained short as well as long impulse bursts (see Figure 81 and Figure 82), weak and strong impulse magnitudes (see Figure 83 and Figure 84), as well as scattered and dense noise bursts (see Figure 84 and Figure 85).

**Figure 81:** Washing machine turning On event.**Figure 82:** Can opener tuning On event.**Figure 83:** Flat TV turning On event.

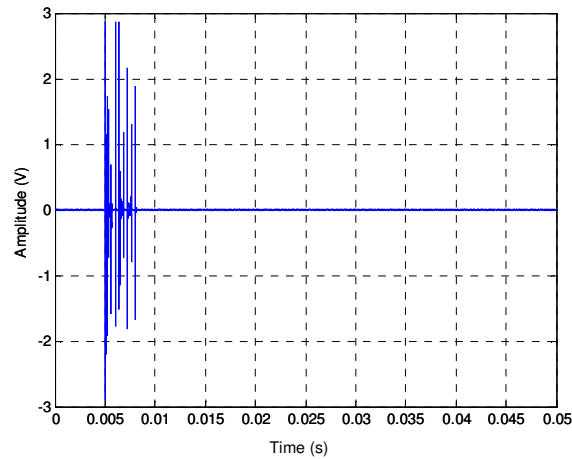


Figure 84: Iron thermostat On event.

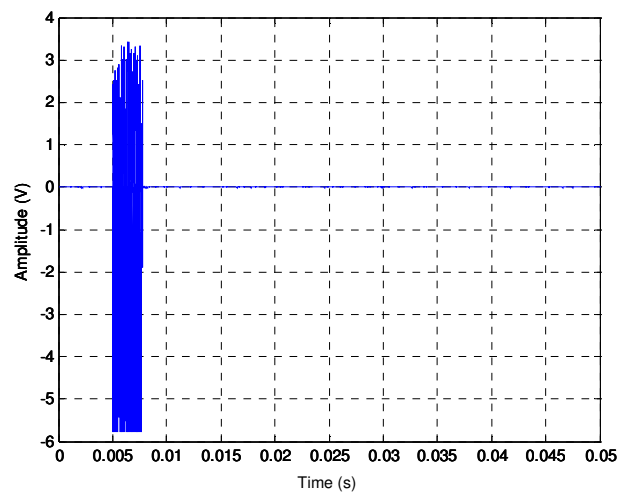


Figure 85: Refrigerator door closing event.

- The shape of an impulsive noise doesn't depend on the device that generates it, but on its in-device source. In particular, events that have similar time signatures are:
 - Electrical switch On events (see Figure 86) as well as thermostat On events (see Figure 84).

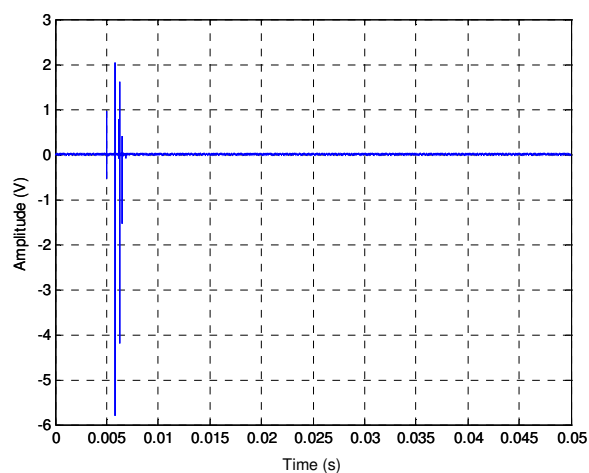


Figure 86: Coffee maker turning On event.

- Electrical switch Off events (see Figure 80) as well as thermostat Off events (see Figure 87).

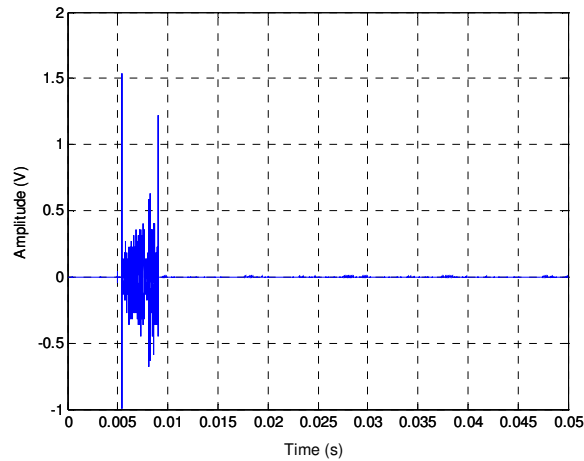


Figure 87: Electrical heating thermostat Off event.

- Electrical plug plugging and unplugging events (see Figure 88 and Figure 89).

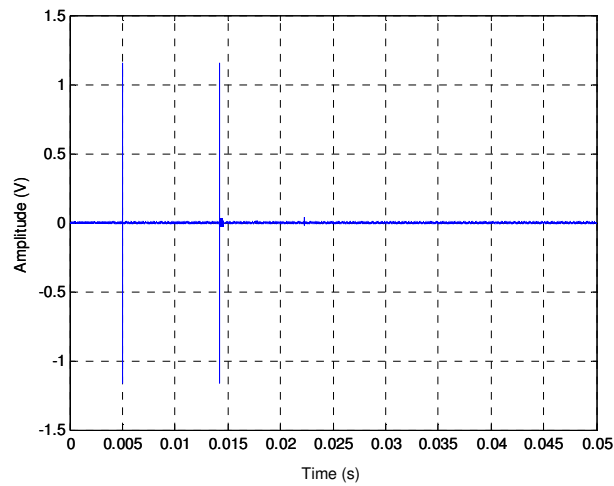


Figure 88: Laptop plug plugging event.

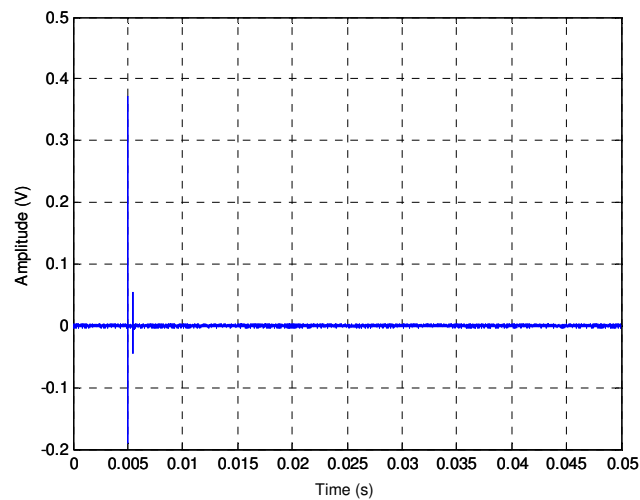


Figure 89: Laptop plug unplugging event.

- Electrical engine start events (by electrical switches), see Figure 82.

These observations lead to the classification of impulsive noises according to their in-device generator.

7.3.2 Noise Classification

Based on the last observation, measured impulsive noises are classified according to their direct generators. Identified direct in-device generators are: electrical switches, thermostats, electrical plugs, and electrical engines.

Six classes of impulsive noises are distinguished:

- Class 1: Electrical switch and thermostat On event.
- Class 2: Electrical switch and thermostat Off event.
- Class 3: Electrical plug plugging.
- Class 4: Electrical plug unplugging.
- Class 5: Electrical engine start.
- Class 6: Diverse weak noises.

Below are detailed the characteristics of each class.

7.3.2.1 Impulsive Noise Class 1

This class includes the impulsive noises generated by the electrical switches and thermostats On events. A characteristic form is reported in Figure 86.

The impulsive noises of this class are strong (high amplitude), composed of a unique burst and characterized by successive and disjointed little impulses. Short impulsive noise bursts belong to this class (see Figure 81), as well as long bursts (see Figure 84).

Amplitude and duration statistics about impulsive noises of this class are reported in Table 16.

	Min	Max	Mean	Std
Amplitude (V)	0.0778	5.6569	3.9958	1.9132
Duration (ms)	0.0001	14	1.3045	2.2113

Table 16: Amplitude and duration statistics of the class 1 impulsive noises

7.3.2.2 Impulsive Noise Class 2

This class includes the impulsive noises generated by the electrical switches and thermostats Off events. Characteristic form is reported in Figure 80 and Figure 87.

The impulsive noises of this class are of strong amplitude, and characterized by two successive short bursts separated by dense noise.

However, pushing down an electrical switch to its Off position could generate harsher impulsive noises (one dense burst), as in the Figure 85 associated to a refrigerator door closing event.

Let's call class 2-2 (for 2 impulses) the class name of the conventional form of the impulsive noises belonging to this class (i.e. that of Figure 80 and Figure 87), and class 2-1 (for 1 impulse) the class name of the remaining impulsive noises (i.e. resembling to that of Figure 85 with a given density).

For the class 2-2 impulsive noises (representing almost 50% of the class 2 noises), amplitude and duration statistics in are shown in Table 17.

	Min	Max	Mean	Std
Amplitude (V)	1.1314	5.6569	2.7832	1.3864
Duration (ms)	0.4500	9	5.0020	2.6225

Table 17: Amplitude and duration statistics of the class 2-2 noises

The same statistics for the class 2/O noises are reported in Table 18.

	Min	Max	Mean	Std
Amplitude (V)	1.1314	5.6569	5.0205	1.3477
Duration (ms)	0.1000	6	1.8750	1.4709

Table 18: Amplitude and duration statistics of the class 2-1 noises

7.3.2.3 Impulsive Noise Class 3

This class includes the impulsive noises generated by the electrical plug plugging events. These noises are gathered in a same class because of their same generator and resemblance, but also because they are linked to a very recurrent domestic event. A characteristic form is reported in Figure 88.

The impulsive noises of this class are of strong magnitude, and characterized by successive two distant short bursts not separated by impulsive noise. Sometimes these two bursts are very close (separated by few μ s).

Amplitude and duration statistics are reported in Table 19.

	Min	Max	Mean	Std
Amplitude (V)	0.8485	5.6569	3.6062	2.1059
Duration (ms)	0.0060	11	2.9732	3.4483

Table 19: Amplitude and duration statistics of the class 3 impulsive noises

7.3.2.4 Impulsive Noise Class 4

This class includes the impulsive noises generated by the electrical plug unplugging events. As for the class 3 noises, these noises are gathered in a same class, among others, because they are linked to a very recurrent domestic event. A characteristic form is reported in Figure 89.

The impulsive noises of this class are weaker than those of the last class. As for the plug plugging event, they are composed of two bursts not separated by impulsive noise, except that in this case the two burst are much closer. Amplitude and duration statistics are reported in Table 20.

	Min	Max	Mean	Std
Amplitude (V)	0.7071	1.4142	0.9899	0.2582
Duration (ms)	0.0120	0.8000	0.3703	0.3398

Table 20: Amplitude and duration statistics of the class 4 impulsive noises

7.3.2.5 Impulsive Noise Class 5

This class includes impulsive noises generated by the electrical engine start events. These events are also generated by an in-device electrical switch. The generated noises, in this case, appear as a strong, low density (scattered), and very long impulsive noises. A characteristic form is reported in Figure 82.

Fluorescent lamp starting event (see Figure 90) is included in this class as generating impulsive noises of the same amplitude, duration, and scattering characteristics.

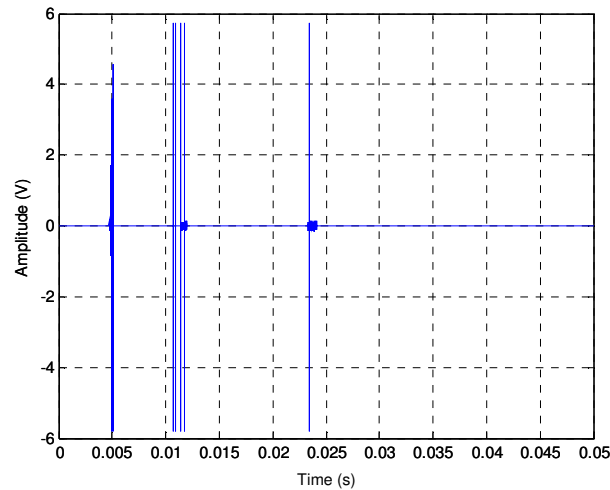


Figure 90: Fluorescent lamp turning on event.

Amplitude and duration statistics about impulsive noises of this class are reported in Table 21.

	Min	Max	Mean	Std
Amplitude (V)	4.2426	5.6569	5.4801	0.5000
Duration (ms)	18	47	30.3750	9.3341

Table 21: Amplitude and duration statistics of the class 5 impulsive noises

7.3.2.6 Impulsive Noise Class 6:

This class includes a diversity of weak impulsive noises. These noises are characterized by their very weak amplitude. Generally appearing in two principal behaviours: short isolated impulse (see Figure 91 for a Residential Gateway IP Phone pick up event) or two (or more) larger impulses (see Figure 83 for a flat TV starting event), these events are also generated by an in-device electrical switch.

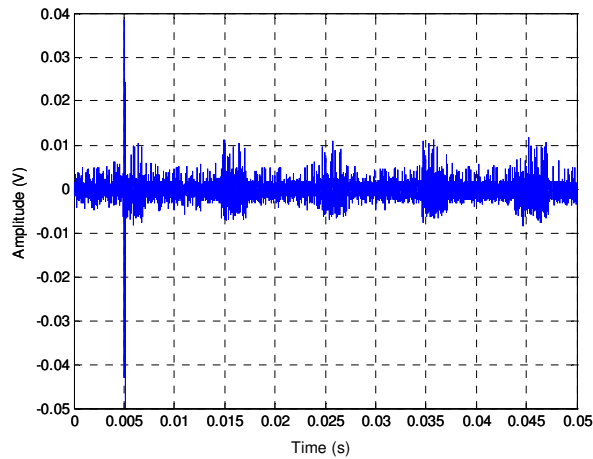


Figure 91: Residential Gateway IP Phone pick up event.

The percentages of the first form appearance and the second one are respectively 69 % and 31 %.

For the first form (weak isolated impulse) called class 6-S (“S” for Short), amplitude and duration statistics are reported in Table 22.

	Min	Max	Mean	Std
Amplitude (V)	0.0099	0.2546	0.0854	0.0710
Duration (ms)	0.0001	0.4500	0.1834	0.1227

Table 22: Amplitude and duration statistics of the class 6/S noises

For the second form (weak two or more separated bursts) called class 6-L (“L” for Long), amplitude and duration statistics are reported in Table 23.

	Min	Max	Mean	Std
Amplitude (V)	0.0141	0.0495	0.0301	0.0133
Duration (ms)	12	50	22.8462	15.4534

Table 23: Amplitude and duration statistics of the class 6/L noises

7.4 Impulsive Noise Modelling

7.4.1 Noise Modelling at Source

In accordance with the statistical analysis of amplitudes and durations of the impulsive noises of each class as detailed in Table 16 to Table 23, three impulsive noises are selected to model each noise class. For each class, the selected noises are:

- The median noise: its duration represent the median value of the impulsive noises durations. 50 % of the noises have durations greater than this median noise duration.
- The short noise: a noise whose duration is inferior to 90 % of the whole noise durations (10th percentile).
- The long noise: a noise whose duration is greater than 90 % of the noises durations (90th percentile).

Table 24 gives the 10th percentile, the median and the 90th percentile of all recorded noise durations, for each class.

	10 th percentile	Median	90 th percentile
Class 1	0.001 ms	0.24 ms	2.98 ms
Class 2 – 1	0.13 ms	2 ms	3.2 ms
Class 2 – 2	1.05 ms	4.25 ms	8.25 ms
Class 3	0.01 ms	1.2 ms	7.5 ms
Class 4	0.012 ms	0.27 ms	0.73 ms
Class 5	18 ms	27 ms	39.8 ms
Class 6 – S	0.003 ms	0.3 ms	0.18 ms
Class 6 – L	12 ms	13 ms	48.1 ms

Table 24: Duration and amplitude statistics by class

The amplitudes of the representative noises are chosen to be as close as possible to the mean amplitude values.

The chosen representative noises are reported in Appendix 11.2. Their durations are reported in Table 25.

	short case	long case	mean case than
Class 1	0.003 ms	3.1 ms	0.3 ms
Class 2 – 1	1.44 ms	8.6 ms	4.12 ms
Class 2 – 2	0.16 ms	3.1 ms	1.8 ms
Class 3	0.006 ms	6.8 ms	2 ms
Class 4	0.012 ms	0.73 ms	0.52 ms
Class 5	18 ms	36 ms	26 ms
Class 6 – 1	0.01 ms	0.29 ms	0.17 ms
Class 6 – 2	same as mean case	48 ms	12 ms

Table 25: Durations of the representative noises

In this section, impulsive noise modelling was performed in the source of the measured noises. Next, a noise model is given in the receiver side.

7.4.2 Impulsive Noise Modelling at the Receiver

The impulsive noise at the receiver is the impulsive noise at the source filtered by the channel H between the source and receiver points (see Figure 92).

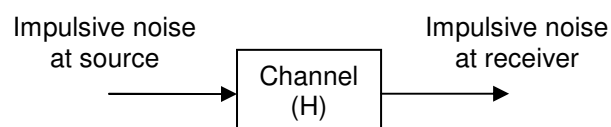


Figure 92: Impulsive noise at receiver – general model.

Thus, realizing an impulsive noise model at the receiver side needs noise knowledge at source (done in previous section) as well as powerline channel modelling.

7.4.2.1 Powerline Channel Model

The channel model considered here is detailed in Section 3. Channels are classified into 9 classes per ascending order of achievable rates. Only the channel class number needs to be fixed. The transfer function (magnitude and phase) is generated statistically. An example of a class 2 and class 9 transfer function magnitudes are given in Figure 93.

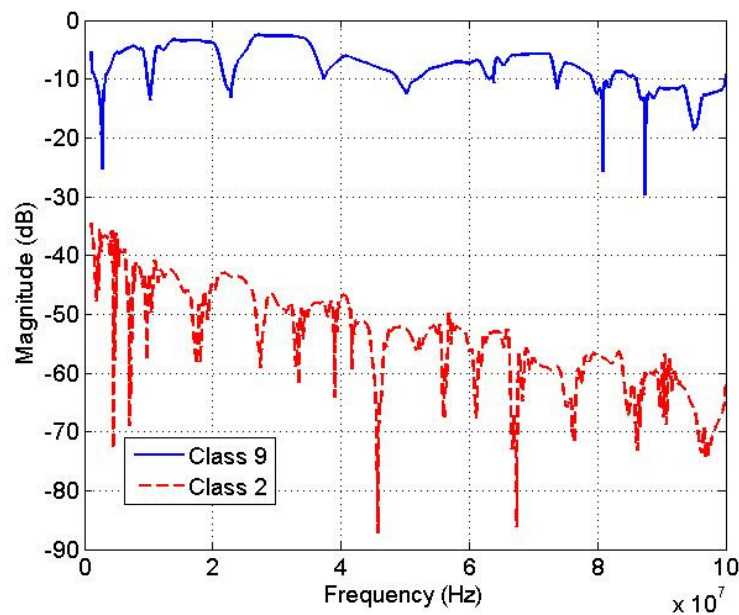


Figure 93: Class 2 and Class 9 magnitude examples.

7.4.2.2 Impulsive Noise at Receiver

As explained earlier, impulsive noise at receiver is the impulsive noise at source filtered by the channel response.

This section gives two examples of impulsive noises at the receiver. Figure 94 presents the impulsive noise of Figure 84 filtered by the class 9 and class 2 channels given in Figure 93. Figure 95 provides a frequency domain representation of the same impulsive noise at the output of the two considered channels.

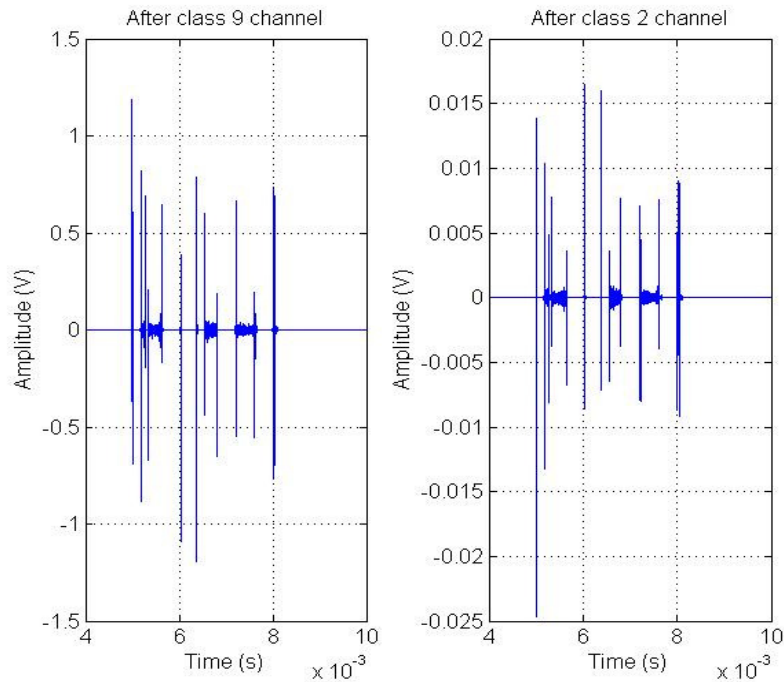


Figure 94: Impulsive noise after class 9 and class 2 channels – time domain representation.

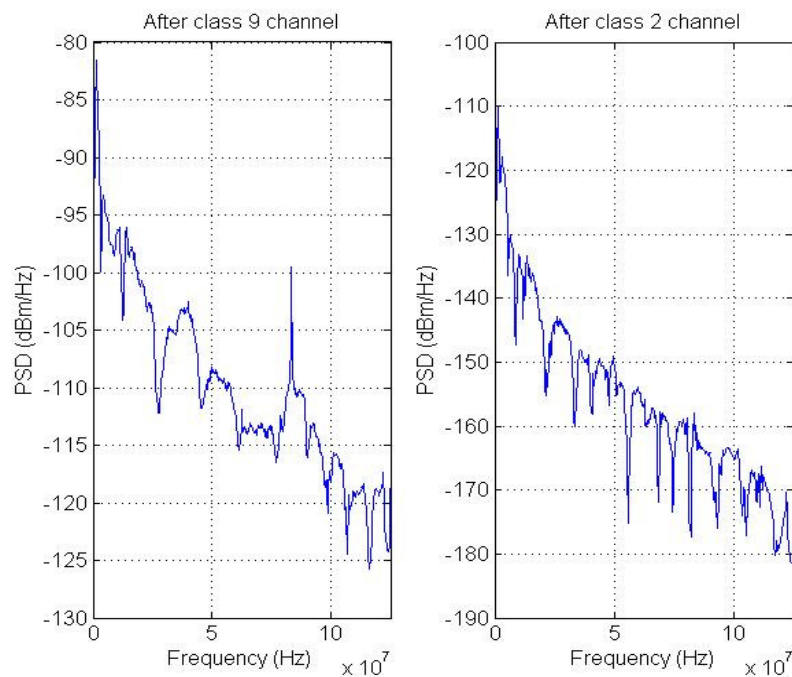


Figure 95: Impulsive noise after class 9 and class 2 channels – frequency domain representation.

Figure 94 demonstrates that, macroscopically, impulsive noise at the receiver keeps a similar shape as at the source. Nevertheless, amplitude attenuation is applied due to channel propagation. The channel impulsive response effect could also be highlighted microscopically as each peak at source is replicated and delayed [36][27] at the receiver.

Figure 95 further highlights the channel affect in the frequency domain. In fact, the spectrum of the impulsive noise at the receiver strongly follows that of the channel.

Characterizing impulsive noise at source permits two different approaches for receiver side modelling:

- impulsive noise modelling by electrical device,
- and random generator of impulsive noise at receiver.

7.4.2.3 Impulsive Noise Modelization by Electrical Device

As mentioned in Section 7.2.1, the PLC impulsive noises study presented in this paper relates to 23 domestic appliances. The list was reported in Table 15. In that Table, functioning states are identified for each device. An impulsive noise is generated (at source) for each transition from one state to another.

Device name	Impulsive noise model at source	Channel classes
Vacuum cleaner	Class 3 – Class 4 Class 1 – Class 2-2	1 to 9
Electric kettle	Class 1 – Class 2-2	1 to 6
Coffee maker	Class 1 – Class 2-2	1 to 6
Electric heating	Class 1 – Class 2-2	1 to 9
Electric carving knife	Class 3 – Class 4 Class 1 – Class 2-1	1 to 6
Paint burner	Class 3 – Class 4 Class 1 – Class 2-2	1 to 6
Computer screen	Class 1 Class 6-S	7 to 9
Iron	Class 3 – Class 4 Class 1 – Class 2-2	1 to 9
Refrigerator	Class 1 – Class 2-1/2	1 to 6
Incandescent lamp	Class 1 – Class 2-2	1 to 6
Fluorescent and Neon lights	Class 5 – Class 2-1	1 to 6
Residential Gateway	Class 6-S	7 to 9
Washing machine	Class 1 – Class 2-1	1 to 6
Videorecorder (VCR)	Class 3 – Class 4	7 to 9
microwave	Class 1 – Class 2-2	1 to 6
Can opener	Class 3 – Class 4 Class 5 – Class 2-1	1 to 6
Laptop	Class 3 – Class 4 Class 6-L	7 to 9
Induction hob	Class 6-S	1 to 6
Food processor	Class 3 – Class 4 Class 1 – Class 2-1	1 to 6
Hair dryer	Class 3 – Class 4 Class 1 – Class 2-2	1 to 6
Set-top-box	No Impulsive noises	7 to 9
Hair clippers	Class 3 – Class 4 Class 6-S	1 to 6
TV	Class 1 – Class 2-2 Class 6-S/L	7 to 9
Computer case	Class 6-S	7 to 9

Table 26: List of devices and states accompanied by impulsive noises

In this Section, an impulsive noise model at receiver is proposed for each device. This model consists in the association of a source noise model and its adequate channel class. The adequate channel class is the class of the channel most likely to connect the electrical device to the receiver. Here, the receiver is supposed to be located close to the TV or PC for video and internet reception. In [26], it was shown that channel classes 9, 8, and 7 are associated to the case where the transmitter and the receiver pertain to the same electrical circuit. The remaining classes (e.g. 6 to 1) are for different electrical circuit paths.

Table 26 depicts, for each device, its impulsive noise models at source and its adequate channel classes.

For certain devices (as coffee makers), plugging or unplugging electrical plugs events are not considered as the devices are supposed to be already plugged.

Some other devices (as vacuum cleaner and electric carving knife), although embedding electrical engines, have starting impulsive noises of class 1 (Electrical switch On event) and not class 5 (Electrical switch and thermostat ON event). Vacuum cleaners and irons are generally plugged anywhere in a home, so channels to PLC receiver are classed from 1 to 9.

For the paint burner and food processor devices, the transitions from Off to Soft and from Soft to High, as well as from High to Soft are class 1 impulsive noises.

In computer screens, impulsive noises are only detected for turning on events. Cathodic screen noises are class 1, while flat screen ones are class 6/S as they are very weak.

Iron impulsive noises are generated by thermostat On (class 1) and Off (class 2-2) events, as well as by plugging and unplugging plugs events (classes 3 and 4).

Refrigerator impulsive noises are generated by thermostat On and Off events (classes 1 and 2-2), and by opening and closing its door (class 1 and class 2-1 respectively).

Incandescent lamps On/Off impulsive noises are generated by electrical switches. For the fluorescent and neon lamps, On events are accompanied by class 5 impulsive noises (see Figure 90), and Off ones by class 2-1 noises.

Residential gateway events are only those associated to IP phone pick up and put down and are rather weak (class 6 noises). As a results of the channel attenuation, these noises are almost always below the stationary noise at the receiver.

Washing machine On events are machine activation (by electrical switch) and washing/rinsing cycle starting. Associated impulsive noises are class 1. Off events result from electrical switch deactivation and washing cycle stopping, and are short class 2-1 events.

The can opener starting noise is a class 5 noise (see Figure 82), and Off event noise is a class 2-1 dense noise.

For the laptop impulsive noises, class 3 and 4 noises correspond to plugging or unplugging the charger plug. Laptop turning On and Off impulsive noises are class 6.

Only On event is accompanied by impulsive noise in induction hob device. Its class is 6.

The switching Off impulsive noise in food processor device is a class 2-1 noise.

The hair dryer Off to Soft impulsive noise is a conventional class 1 noise. Nevertheless, the remaining transitions between Soft, High, Turbo, and Off states have particular impulsive noises: succession of conventional class 2-2 ones. An example is given in Figure 96. The observed number of class 2-2 noise replicas varies between 1 and 18.

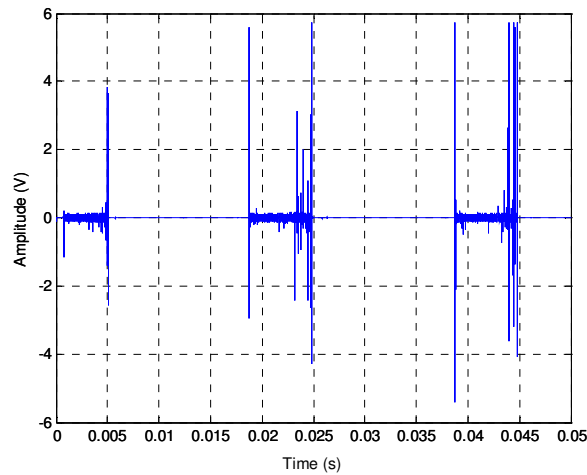


Figure 96: Hair dryer high to soft event.

The electric hair clippers impulsive noises (On-Off-Height change) are class 6 ones.

For the TVs, cathodic ones have class 1 impulsive noises for turning On events and class 2-2 for turning Off events. Flat TVs turning On events are short class 1 and class 6-S. Turning Off events are not accompanied by impulsive noise.

Computer screen events are only turning On ones and are class 6-S.

7.4.2.4 Random Generator of Impulsive Noise at Receiver

A second approach for impulsive noise modelling at receiver side could be used for PLC channel simulations. It consists of randomly generating impulsive noise from a set of source impulsive noise models and PLC channel models.

This approach is device and channel independent. A generated noise at receiver is simply a random impulsive noise at source associated to a random channel.

This approach makes it possible to build a random impulsive noise database at receiver side for PLC system robustness tests.

8 Stationary noise characterization and modelling

This Section focuses on the stationary noise observed on the PLC channel. After a literature survey on the characterisation of stationary noise, general observations about measured stationary noises in frequency domain are given, and a frequency domain noise model is proposed up to 100MHz.

8.1 State of the art

The background noise in low voltage power line is colored and significantly increases toward lower frequency. This noise varies slowly over time and is caused by summation of numerous noise sources of low power such as universal motors, light dimmers, television receivers which can be characterised individually [40], [41]. The narrow band noise, mostly amplitude modulated sinusoidal signals caused by ingress of radio broadcasting stations is included in background noise since it varies slowly over time.

From the literature, the background noise is mainly modeled in the frequency domain and there are two methods. The first one is the spectrum fitting method where the measured noise PSD or voltage spectrum density is fitted into certain functions of frequency. In this case the noise is approximated by several sources of Gaussian noise in non-overlapping frequency bands with different noise powers given by the PSD. Contrary to first method, the second one provides information on the random behaviour of the noise at each individual frequency by statistical analysis. In [42], authors considered that Gaussian approximation is not a good approximation in higher frequency bands. In order to find the relation between the observed random characteristics of the noise and the inherent physics mechanism of the noise induces by the electric system, the chaos theory is also investigated [43].

The high frequency low power density measurement began in 1972 with the work of Smith [44]. The noise power density level depends on location type: building, laboratory, business office, residential house, and more than 60 dB of difference can be obtained. Lots of measurement campaigns have been made in laboratory. Whereas in [45] the background level in residential falls under the bound measurement of -130 dBm/Hz above 500 kHz and in [44] the background noise level equals the thermal noise level above 50 MHz, the level of the PSD in high frequency can reach high values.

In [3] the power spectrum density expressed in dBm/Hz is given by $N=a+bf^c$ with f in MHz. The parameters of this model are obtained by curve fitting. This model is used by [46] and [47]. The measurement was made in a Canadian building in [3] and in Finland [46] over 100 MHz bandwidth. The noise is modelled as colored Gaussian noise with PSD given in the next figure.

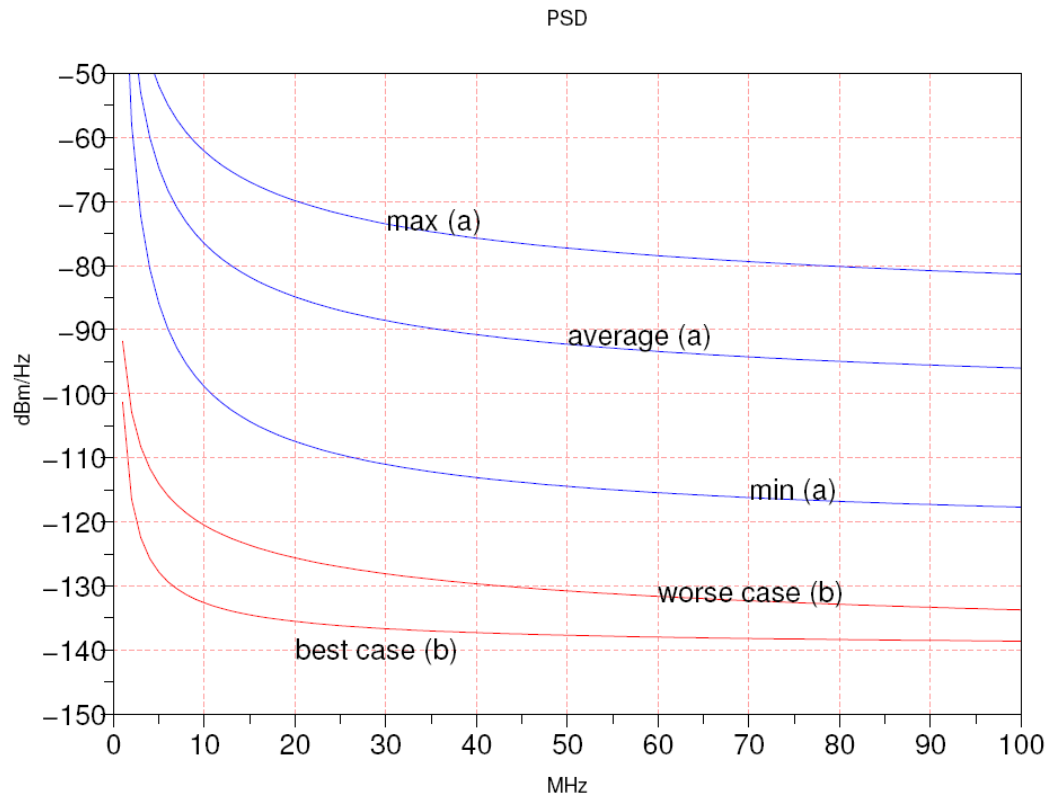


Figure 97: Background noise PSD in dBm/Hz. (a) in Finland [46], (b) in Canada [3].

As the noise power spectrum density depends on the measurement environment, the parameters of the model can be given by random variables. In [48], the PSD in W/kHz is:

$N = 10^{\{K - 3.95 \cdot 10^{-5} f\}}$, with f in Hz, K constant for long periods of time and approximated by Gaussian distribution with average of -5.64 and standard deviation of 0.5. The parameters of the model proposed in [49] where $N = N_0 + N_1 e^{\{f/f_1\}}$ in dBm/Hz, are given in [50] where N_0 follows normal distribution, N_1 follows uniform distribution and f_1 follows shifted exponential distribution in office and residential buildings. The random characteristic of the parameters induces possible very high PSD level.

The Nakagami model is often used to represent wireless fading signals in multipath scattering environment with relatively large delay-time spreads, and with different clusters of reflected waves. In the power line network, the average amplitude of the noise coming from a single source remains mostly unchanged, but due to the complex scattering in the network, the resultant noise at the receiver can be roughly regarded as Rayleigh distributed. Since the background noise is a combination of Rayleigh distributed noises from multiple sources, it is reasonable to use the Nakagami probability density function to represent the noise amplitude distribution [51]. A closed-form expression for the real part of background noise is also derived [52].

The noise levels found in the literature are expressed in a large variety of units (dBW/Hz, dBV²/Hz...) and unit conversions are not always possible. All conversions become feasible if the measurement method and the input impedance of the measurement network given in [53] are respected.

8.2 Stationary Noise Measurement Campaign

Measurements of stationary noise were carried out in 6 different sites, in the frequency domain, and by means of a spectrum analyzer, as illustrated in Figure 98.

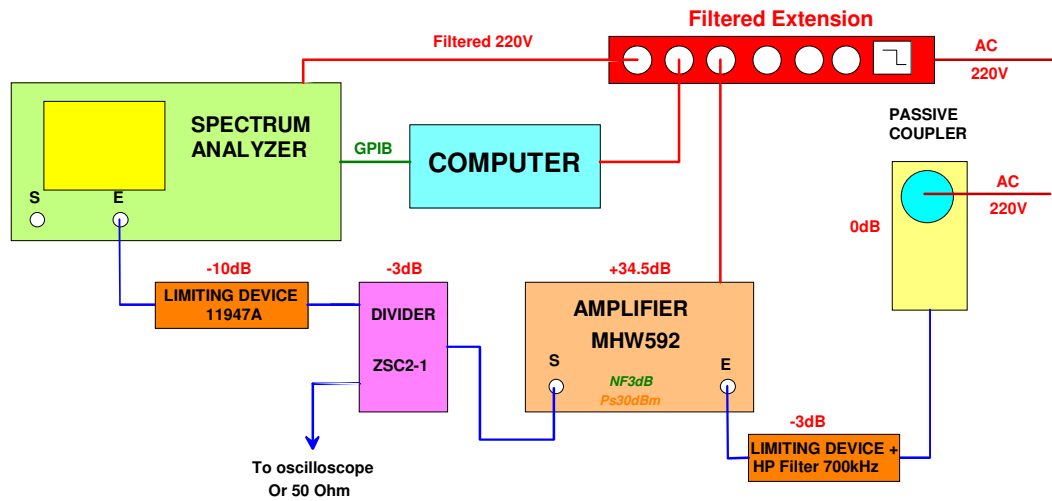


Figure 98: Stationary noise measuring hardware

The stationary noise present on the electrical support is measured via a passive coupler in the frequency band 30 kHz – 100 MHz, connected to an electrical outlet. This coupler is followed by a high-voltage limiter and a high-pass filter whose cut-off frequency is equal to 700 KHz. This filter makes it possible to isolate the experimental setup from high-level noises present at low frequencies.

The signal is then amplified (MHW592 amplifier) by 34.5 dB. The resulting signal power is divided between a scope, for possible temporal acquisitions, and a spectrum analyzer. The entry of the spectrum analyzer is protected by a second high-voltage limiter.

The whole of the measurement material is connected to the power supply through a filtered extension, which makes it possible to isolate the experimental device from the electrical supply network.

The collected data is recorded on PC, connected to the spectrum analyzer by a GPIB bus and controlled by a specific measurement software.

Stationary noise measurements were carried out by 3 different spectrum analyzer configurations, as reported in Table 27.

	Configuration 1	Configuration 2	Configuration 3
Min frequency	1 MHz	1 MHz	1 MHz
Max frequency	100 MHz	100 MHz	100 MHz
Resolution band	3 kHz	3 kHz	300 kHz
Detection	RMS	RMS	Peak
Trace mode	Power AVG	Power AVG	Maxhold
Number of bands	4	4	1
Number of points per band	8192	8192	401
Measurements Type	Punctual, principal outlets	Cyclic, 1 outlet, every hour	Cyclic, 1 outlet, every 15min

Table 27: Stationary noise measurements configuration

Configurations 1 and 2 allow a measurement of the effective power of the stationary noise. These measurements are precise enough because they are taken with a resolution bandwidth of 3 kHz for a total number of points of

32768 on the whole of the band [1MHz - 100MHz]. In fact, punctual measurements on various site outlets (configuration 1) and cyclic measurements, over 24 hours with a one hour frequency, in only one outlet (configuration 2) are carried out.

Configuration 3 is characterized by a greater resolution band (300 KHz) and a reduced number of points. The sweeping time is thus shorter. The acquisition frequency is equal to 15 min for this configuration.

In next sections, general observations on measured stationary noises are firstly presented. After that, a frequency domain noise model is proposed.

8.3 Stationary Noise Characterization

The measured stationary noises examination in frequency domain showed that a $\frac{1}{f^2}$ decreasing shape is noticeable. An example is given in Figure 99.

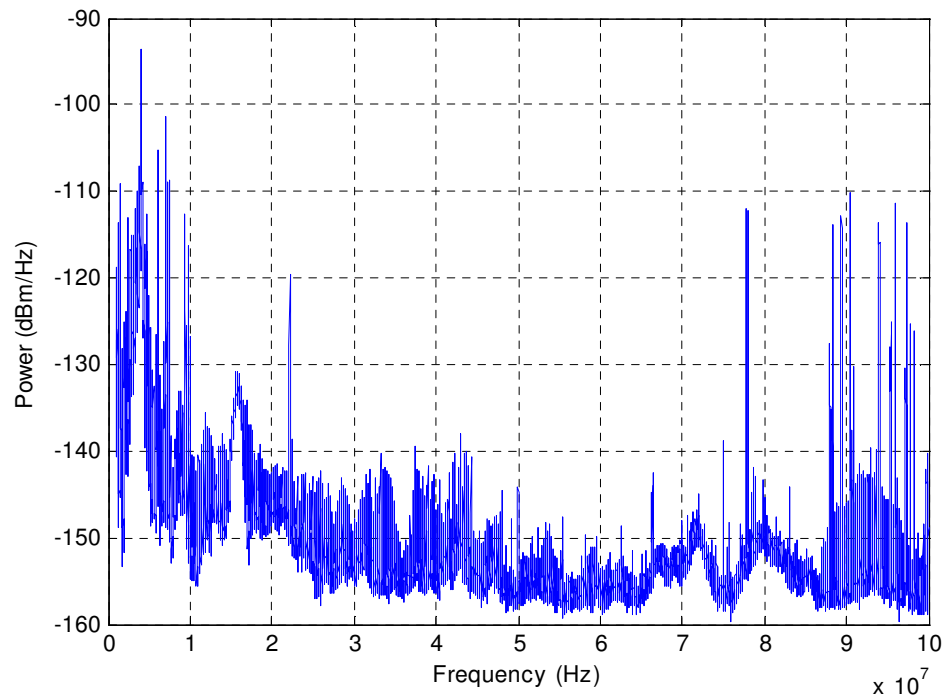


Figure 99: measured stationary noise

Particular high noise levels are noticed in low frequencies (up to 10 MHz) as well as in high frequencies (FM band starting from 88 MHz).

Field measurements showed also that a stationary background noise exists at a level of between -155 and -145 dBm/Hz that is 15 to 25 dB above the thermal noise floor of about -170 dBm/Hz. This noise level is further highlighted in [54].

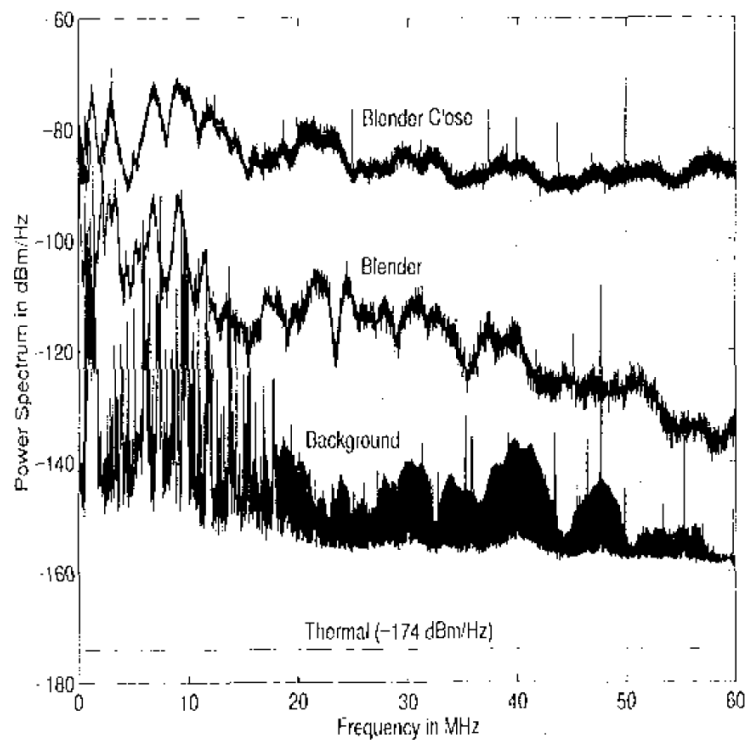


Figure 100: Stationary noise levels from [54]

Figure 100 (from [54]) shows the thermal noise level (-174dBm/Hz) as a reference, background noise level in an unloaded powerline, and the noise levels produced by a blender connected at outlet close to principal coupler (labelled as Blender Close), and far from it (labelled as Blender), respectively. This figure confirms indeed the -155 dBm/Hz background noise level.

Above the background noise, ingress noise from radio sources can be observed. Some other ingress noises are leakages from nearby electrical or industrial equipment. Other ingress noises are from radio stations. Radio station ingresses are characterized by a narrow bandwidth and a high intensity. Depending on its distance, a radio station ingress noise can be 30 to 40 dB above the background noise. Their intensities also vary depending on the time of the day (with the worst ingresses occurring during the late night and early morning when the ionosphere provides the best conditions for radio transmission).

8.4 Stationary Noise Modelling

The noise model proposed in this Section is derived from that explained in [55] for coaxial cable noise environment model.

The measured stationary noise environment can be modelled using controlled random variables. This noise environment is a combination of:

- the background noise floor at a level of about -155 dBm/Hz ;
- strong radio interference carriers within short-wave radio frequency bands ;
- a frequency-dependent radio background noise ;
- and randomly distributed interference carriers.

In the implementation of this stationary noise model, a mask for short-wave radio frequency bands is first established according to Table 28.

TYPE	BAND	Fmin KHz	Fmax kHz
LONG WAVE	GO	151	281
MEAN WAVE	OM	531	1 602
SHORT WAVE	120m	2 340	2 400
SHORT WAVE	90m	3 200	3 400
SHORT WAVE	75m	3 900	4 000
SHORT WAVE	60m	4 750	5 060
SHORT WAVE	49m	5 950	6 200
SHORT WAVE	41m	7 100	7 300
SHORT WAVE	31m	9 500	9 900
SHORT WAVE	25m	11 650	12 050
SHORT WAVE	21m	13 600	13 800
SHORT WAVE	19m	15 100	15 450
SHORT WAVE	16m	17 550	17 900
SHORT WAVE	13m	21 450	21 850
SHORT WAVE	11m	25 600	26 100
FM BAND	-	87 500	100 000

Table 28: Radio broadcasting frequency limits up to 100MHz

In addition, eight groups of random interference frequencies, each of which contains 30 random frequencies, are generated representing eight different interference magnitudes. These additional 240 random interference frequencies are incorporated into the short-wave radio mask.

Random numbers are then generated representing amplitudes of potential interference carriers at every (discrete) frequency point. These random amplitudes are then applied to the 240 random interference carriers. A background noise floor level of -155 dBm/Hz, with a $\frac{1}{f^2}$ decreasing shape, is after that applied to the obtained mask. And the result is further filtered to emulate the bandwidth of interference carriers.

Figure 101 shows a generated $\frac{1}{f^2}$ decreasing stationary noise model (blue curve). In red is reported the $\frac{1}{f^2}$ decreasing curve it follows. This red curve $C(f)$ is linearly defined by the formula:

$$(31) \quad C(f) = \frac{1}{f^2} + 10^{-155/10}$$

It should be noted that the described model is a first proposal designed to fit the experimental observations carried out in the project. This model will be used as a first input for the sake of communication system simulations and performance evaluation. It will be refined at a later stage in the course of the project as further investigation will be performed on this topic.

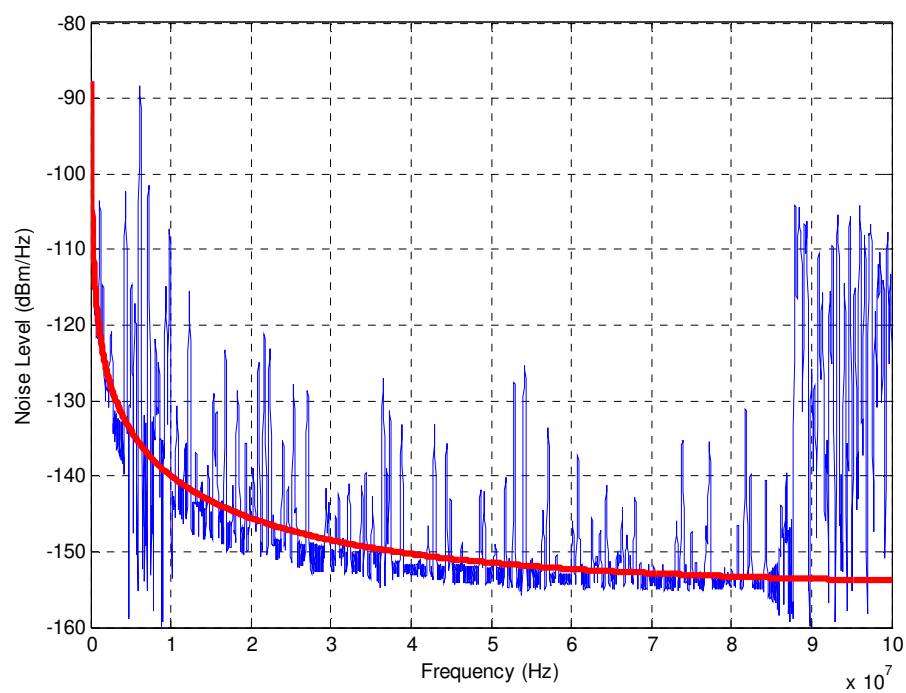


Figure 101: Stationary noise model - $\frac{1}{f^2}$ decreasing shape

9 Conclusion and Future Work

This document presents the studies conducted within WP3 of the OMEGA project on the characterization and modelling of the PLC channel. A measurement campaign covering a frequency band up to 100 MHz is presented and the main channel parameters are evaluated. Statistical models are proposed for the PLC channel transfer function. Firstly, an empirical model of the CTF is given to reflect the experimentally observed channel characteristics. Secondly, a model is presented in an analytical form, allowing for close form computation of the channel characteristic parameters. Finally, a study of the CTF is provided based on the transmission line theory.

The impulsive noise generated by different electrical appliances is experimentally characterized. From these observations, a model of impulsive noise at the source is proposed, which can be used to build a model applicable at the receiver. Stationary noise is finally investigated by both literature overview and experimental observations, and a simple model is provided.

The models proposed in this deliverable will be used as a starting point for the future WP3 studies on digital communications. In particular, the different proposals for advanced signal processing for PLC communications will be assessed through link level simulations. The proposed models will ensure that the simulations reflect operation in a realistic PLC environment.

However, further research will be conducted on the topic of PLC channel characterization and modelling. The following perspectives are envisioned for this work:

- Different approaches of the PLC CTF statistical modelling have been presented. A first, empirical approach (Sections 3) consists in an accurate rendering of the observed PLC CTF characteristics in the frequency domain, based on a large set of experimental measurements. A complementary, analytical approach (Section 5) consists in describing the PLC CTF in the form of a tractable analytical expression using network topology considerations. As a future work, the advantages of these two approaches could be linked to provide a model describing in closed form the various channel classes that have been experimentally observed.
- The deterministic approach of CTF modelling based on the transmission line theory is a useful tool to understand the underlying physics of wire transmission. The effect of connecting different devices on a particular network topology is of particular interest. In order to calibrate the proposed model, measurements of an experimental topology should be performed, with various load configurations.
- A complete model of impulsive noise at the source has been proposed. As a basis of this model, specific noise signatures have been selected as references. A further step would consist of deriving a general mathematical description of the observed impulsive noise for the purpose of noise synthesis.
- Various observations of the stationary noise have been reported in the literature, generally implying different experimental setups. The model proposed in this deliverable is a first approach designed to fit our observations, and could be refined as more investigation will be performed in this field.
- It will be interesting, in the PLC context, to complete this study with an analysis of the channel time variation, e.g. AC line synchronous noise, CTF cyclo-stationary.
- An analysis from an information theory point of view of the channel characterizations derived from the measurements campaign described in Section 2 can be envisaged. Indeed, as it is the case for the Ultra Wide Band (UWB) channel [56], a Maximum Entropy Method (MEM) can provide good indications whether, if yes or not, a multiband approach can be of interest for PLC transmission.

10 References

- [1] K. Dostert, "Telecommunications over power distribution grid: Possibilities and limitations," ISPLC'1997, Essen Germany, 1997.
- [2] M. Zimmermann, K. Dostert, "A multi-path signal propagation model for the powerline channel in the high frequency range," ISPLC'1999, pp. 45-51, Lancaster U.K., 1999.
- [3] T. Esmailian, P.G. Gulak, and F.R. Kschischang, "A discrete multitone power line communications system," in IEEE International Conference on Acoustics, Speech, and Signal Processing, vol. 5, Istanbul, Turkey, June 2000, pp. 2953-2956.
- [4] E. Liu, Y. Gao, G. Samdani, Omar Mukhtar, and T. Korhonen, "Broadband powerline channel and capacity analysis," ISPLC 2005, pp.7-11, April. 2005.
- [5] H. Philipps, "Modeling of Power Line Communications Channels", ISPLC'99, Lancaster, UK, April 1999.
- [6] M. Zimmermann, K. Dostert, "A Multipath Model for the Power Line Channel", IEEE Trans. Commun., vol. 50, no. 4, pp.553-559, April 2002.
- [7] H. Philipps, "Development of a Statistical Model for Power Line Communications Channels", Proceedings of ISPLC 2000, Limerick, Ireland, April 2000.
- [8] O.G. Hooijen, "On the Relation Between Network Topology and Power Line Signal Attenuation", ISPLC'98, Tokyo, Japan, March 24-26, 1998.
- [9] P. Amirshahi and M. Kavehrad, "Transmission Channel Model and Capacity of Overhead Multi-conductor Medium-Voltage Powerlines for Broadband Communications", ISPLC 2004, Zaragoza Spain, March-April 2004.
- [10] S. Galli, T. C. Banwell, "Modeling the Indoor Power Line Channel: New Results and Modem Design Considerations", Consumer Communications and Networking Conference, 2004. CCNC 2004, Telcordia Technol USA, January 2004.
- [11] H. Heng, S. Chen, Y. L. Guan, C. L. Law, "Modeling of Transfer Characteristics of the Broadband Power Line Communication Channel" IEEE Transactions on Power delivery, Vol. 19, No. 3, July 2004.
- [12] V. Degardin, M. Lienard, A. Zeddani, F. Gauthier, and P. Degauque, "Classification and characterization of impulsive noise on indoor power lines used for data communications". IEEE Transactions on Consumer Electronics, Vol. 48, November 2002.
- [13] T. Esmailian, F. R. Kschischang, and P. Glenn Gulak, "In-building power lines as high-speed communication channels: channel characterization and a test channel ensemble", Int. J. Comm. Sys. 2003.
- [14] T. V. Prasad, S. Srikanth, C. N. Krishnan, and P. V. Ramakrishna, "Wideband Characterization of Low Voltage outdoor Powerline Communication Channels in India", International Symposium on Power-Line Communications and its Applications (ISPLC'2001), Sweden, April 2001.
- [15] R. Bultitude, S. Mahmoud, and W. Sullivan, "A comparison of indoor radio propagation characteristics at 910MHz and 1.75 GHz", IEEE J. Sel. Areas Commun., January 1989, 7, (1), pp. 20-30.
- [16] R. Bultitude, R. Hahn, and R. Davies, "Propagation considerations for the design of indoor broadband communications system at EHF", IEEE Trans. Veh. Technol., February 1998, 47, (1), pp. 20-30.
- [17] Yang Xiaoxian, Zheng Tao, *et al.*, "Investigation of Transmission Properties on 10-kV Medium Voltage Power Lines—Part I: General Properties", IEEE Transactions on Power delivery, Vol. 22, Issue. 3, pp. 1446-1454, July 2007.
- [18] R. Aquilué de Pedro, "Power line communications for the electrical utility: physical layer design and channel modeling", Ph.D. thesis, Ramon Llull University, Barcelona, Spain, 2008
- [19] R. J. C. Bultitude, "Estimating frequency correlation functions from propagation measurements on fading radio channels: a critical review", IEEE Journal on Selected Areas in Communication, vol. 20, num. 6, p. 1133-1143, August 2002.
- [20] J. S. Bendat, A. G. Piersol, *Measurement and analysis of random data*, Wiley, New York, 1966.
- [21] IntuiLink Connectivity Software, <http://www.home.agilent.com/agilent/product.jsp?nid=-536902427.536882050.00&cc=CA&lc=fre>.

- [22] L. H.-J. Lampe and J. B. Huber, "Bandwidth Efficient Power Line Communications Based on OFDM", *International Journal of Electronics*, Vol. 54, Issue 1, pp. 2-12, 2000.
- [23] D. C. Cox, and R. P. Leck, "Correlation bandwidth and delay spread multipath propagation statistics for 910-MHz urban mobile radio channels", *IEEE Trans. Commun.*, Nov. 1975, 23, pp. 1271-1280.
- [24] P. Sutterlin, "A Power Line Communication Tutorial: Challenges and Technologies", *ISPLC'98*, Tokyo Japan, March 1998.
- [25] M. Tlich, A. Zeddami, F. Moulin, F. Gauthier, and G. Avril, "A broadband Powerline Channel Generator", *Proceedings of the IEEE International Conference on Power Line Communications and Its Applications*, *ISPLC'07*, pp. 505-510, Pisa, Italy, March 26-28, 2007.
- [26] M. Tlich, A. Zeddami, F. Moulin, and F. Gauthier, "Indoor Powerline Communications Channel Characterization up to 100 MHz – Part I: One-Parameter Deterministic Model", *IEEE Transactions on Power delivery*, Vol. 23, Issue. 3, pp. 1392-1401, July 2008.
- [27] M. Tlich, A. Zeddami, F. Moulin, and F. Gauthier, "Indoor Powerline Communications Channel Characterization up to 100 MHz – Part II: Time-Frequency Analysis", *IEEE Transactions on Power delivery*, Vol. 23, Issue. 3, pp. 1402-1409, July 2008.
- [28] M. Tlich, G. Avril, A. Zeddami, "Coherence bandwidth and its relationship with the RMS delay spread for PLC channels using measurements up to 100 MHz", *1st International Home Networking Conference (IHN 2007)*, Paris – France, 10-12 December 2007.
- [29] A. M. Tonello, "Wideband Impulse Modulation and Receiver Algorithms for Multiuser Power Line Communications," *EURASIP Journal on Advances in Signal Processing*, vol. 2007, Article ID 96747, 14 pages, 2007. doi:10.1155/2007/96747.
- [30] G. L. Stuber, *Principles of Mobile Communications*, Kluwer, 1996.
- [31] M. Tlich et al., "A Broadband Powerline Channel Generator," *Proc. of Int. Symp. Power Line Communications 2007*, Pisa, pp. 505-510, March 2007.
- [32] J. Cortés, F. Cañete, L. Díez, and J. Entrambasaguas, "Characterization of the Cyclic Short-Time Variation of Indoor Power-line Channel Response," *Proc. of Int. Symp. Power Line Communications*, Vancouver, pp. 326-330, April 2005.
- [33] G. T. Andreou, D. P. Labridis, "Experimental Evaluation of a Low-Voltage Power Distribution Cable Model Based on a Finite-Element Approach", *IEEE Transactions on Power delivery*, Vol. 22, Issue. 3, pp. 1455-1460, July 2007.
- [34] T. S. Pang, P.L. So, A. Kamrul, "Common-mode current propagation in power line communication network using multi-conductor transmission line theory", *International Symposium on Power-Line Communications and its Applications (ISPLC'07)*, Pisa, Italy, pp. 517-522, March 2007.
- [35] G. T. Andreou, D. P. Labridis, "Electrical Parameters of Low-Voltage Power Distribution Cables Used for Power-Line Communications", *IEEE Transactions on Power delivery*, Vol. 22, Issue. 2, pp. 879-886, April 2007.
- [36] G. Avril, M. Tlich, F. Moulin, A. Zeddami, F. Nouvel, "Time/Frequency analysis of impulsive noise on powerline channels", *First International Home Networking Conference (IHN 2007)*, Paris – France, December 2007.
- [37] M. Zimmermann, K. Dostert, "An analysis of the broadband noise scenario in Powerline networks", *ISPLC'00*, Limerick, Ireland, April 2000.
- [38] V.B. Balakirsky, A. J.H. Vinck, "Potential limits on powerline communication over impulsive noise channels", *ISPLC'03*, Kyoto, Japan, March 2003.
- [39] V. Degardin, M. Lienard, P. Degauque, A. Zeddami, F. Gauthier, "An analysis of the broadband noise scenario in Powerline networks", *IEEE International Symposium on Electromagnetic Compatibility EMC 2003*, Istanbul, Turkey, May 2003.
- [40] R. Vines, H. Trissell, L. Gale, and J. B. O'neal, "Noise on residential power distribution circuits," *IEEE Transactions on Electromagnetic Compatibility*, vol. EMC-26, no. 4, pp. 161-168, Nov. 1984.
- [41] G. Mambayashi, "Noise measurements of the residential power line," in *IEEE International Symposium on Power Line Communications and Its Applications*, 1997.

- [42] Y. Hirayama, H. Okada, T. Yamazato, and M. Katayama, "Noise analysis on wide-band PLC with high sampling rate and long observation time," in IEEE International Symposium on Power Line Communications and Its Applications, Kyoto, Japan, Mar. 2003, pp. 142--147.
- [43] Z. Wang, H. Hou, and Y. Gan, "Feature extraction of the noise in L-PLC," in IEEE International Conference on Automation and Logistics, Aug. 2007, pp. 1341--1346.
- [44] A. Smith, "Power line noise survey," IEEE Transactions on Electromagnetic Compatibility, vol. EMC-14, no. 1, pp. 31--32, Feb. 1972.
- [45] M. Tanaka, "High frequency noise power spectrum, impedance and transmission loss of power line in japan on intrabuilding power line communications," IEEE Transactions on Consumer Electronics, vol. 34, no. 2, pp. 321--326, May 1988.
- [46] E. Liu, Y. Gao, G. Samdani, O. Mukhtar, and T. Korhonen, "Broadband characterization of indoor powerline channel and its capacity consideration," in IEEE International Conference on Communications, vol. 2, May 2005, pp. 901--905.
- [47] R. Pighi and R. Raheli, "Linear predictive detection for power line communications impaired by colored noise," EURASIP Journal on Applied Signal Processing, vol. 2007, p. 12 pages, 2007. [Online]. Available: <http://www.hindawi.com/GetArticle.aspx?doi=10.1155/2007/32818>
- [48] S.-Y. Jung, "A channel model for power line communication in home network," in Proceedings on the 15th CISL Winter Workshop, Koshu, Japan, Feb. 2002.
- [49] H. Philipps, "Performance measurements of powerline channels at high frequencies," in IEEE International Symposium on Power Line Communications and Its Applications, 1998, pp. 229--237. [Online]. Available: <http://www.isplc.org/docsearch/>
- [50] D. Benyoucef, "A new statistical model of the noise power density spectrum for powerline communication," in IEEE International Symposium on Power Line Communications and Its Applications, 2003, pp. 136--141.
- [51] H. Meng, Y. Guan, and S. Chen, "Modeling and analysis of noise effects on broadband power-line communications," IEEE Transactions on Power Delivery, vol. 20, no. 2, pp. 630--637, Apr. 2005.
- [52] Y. Kim, S. Choi, and H.-M. Oh, "Closed-form expression of Nakagami-like background noise in power-line channel," IEEE Transactions on Power Delivery, vol. 23, no. 3, pp. 1410--1412, July 2008.
- [53] ETSI TS 102 447, Powerline Telecommunications (PLT); Programmable PSD Mask; Specifications for Access and Indoor Systems, ETSI Technical Specification, June 2008.
- [54] D. Liu, E. Flint, B. Gaucher, and Y. Kwark, "Wide band AC Power Line Characterization", IEEE Trans. on Consumer Electronics, pp.1087-1097, November 1999.
- [55] Walter Y. Chen, "Home Network Basis: Transmission Environments and Wired/Wireless Protocols", Prentice Hall PTR, July 11, 2003
- [56] de Lacerda Neto, R.L. Menouni, A. Debbah, M. Fleury, B.H. "A Maximum Entropy Approach to Ultra-Wideband Channel Modeling", ICASSP 2005.

11 Annexes

11.1 Additional information on PLC channel measurement campaign

In this part, extra information and statistics are given concerning PLC channel measurement that were presented in section 2.2.

The list of measurements made in section 2.2 is recalled in Table 29.

Site number	Site information	Number of transfer functions
1	House - Urban	19
2	New house - Urban	13
3	Recently restored apartment – Urban	12
4	Recent house – Urban	28
5	Recent house – Urban	34
6	Recent house – country	22
7	Old House - country	16

Table 29: Distribution of transfer functions by site

The observed measurements were separated in 9 classes as detailed in section 3.1. The distribution of the sites by class is indicated in Table 30. Excepting the class 1, the other classes consist of transfer functions from various sites (3 to 6 sites). The sites are variable in terms of size (apartments, houses) and building construction date (recent and old electric installations), as the CTF measured on of each site may correspond to low-capacity classes as well as high-capacity classes.

Class number	Sites
1	6
2	1, 5, and 6
3	1, 3, 4, 5, 6, and 7
4	1, 3, 4, and 7
5	1, 3, 4, 5, and 7
6	2, 4, 5, and 7
7	2, 4, 5, and 6
8	2, 3, 4, and 6
9	1, 2, 3, 5, 6, and 7

Table 30: Distribution of sites by class

Table 31 gives for each channel class the repartition between channels where the Tx and Rx pertain to the same electrical circuit, and channels where the Tx and Rx pertain to different electrical circuits.

Class	Same circuit	Different circuits
1	0%	100%
2	0%	100%
3	0%	100%
4	0%	100%
5	0%	100%
6	0%	100%
7	46%	54%
8	100%	0%
9	100%	0%

Table 31: Repartition of the channel categories for each class

Finally, Table 32 gives the repartition of the channel classes for each measurement site. We can observe that the channel classes are rather uniformly found in most of the sites types, so no direct link between the type of building or environment and the channel class can be made.

Site	Classes								
	1	2	3	4	5	6	7	8	9
All	3,49%	16,78%	18,18%	11,88%	11,88%	12,58%	9,79%	7,69%	7,69%
1	0%	36,84%	42,11%	5,26%	5,26%	0%	0%	0%	10,53%
2	0%	0%	0%	7,69%	7,69%	30,77%	38,46%	7,69%	7,69%
3	0%	0%	8,33%	33,33%	16,67%	0%	0%	25%	16,67%
4	0%	0%	21,43%	14,29%	17,86%	10,71%	14,29%	21,43%	0%
5	0%	23,53%	17,65%	0%	17,65%	23,53%	8,82%	0%	8,82%
6	22,73%	40,91%	18,18%	0%	0%	0%	9,09%	4,55%	4,55%
7	0%	0%	6,25%	43,75%	12,5%	18,75%	0%	0%	12,5%

Table 32: Repartition of the channel c classes for each site

11.2 Representative Noise Models at Source

Referring to the impulsive noise model presented in section 7, in this annex are shown representative noises (median, short, and long) per class.

11.2.1 Class 1 Model

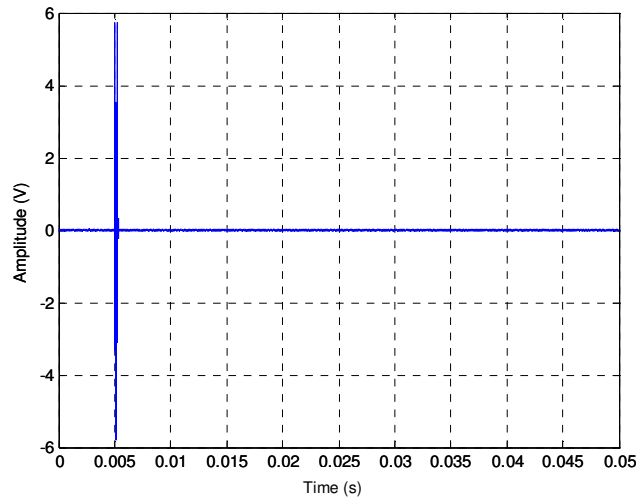


Figure 102: Mean case – Refrigerator opening door event – 0.3 ms.

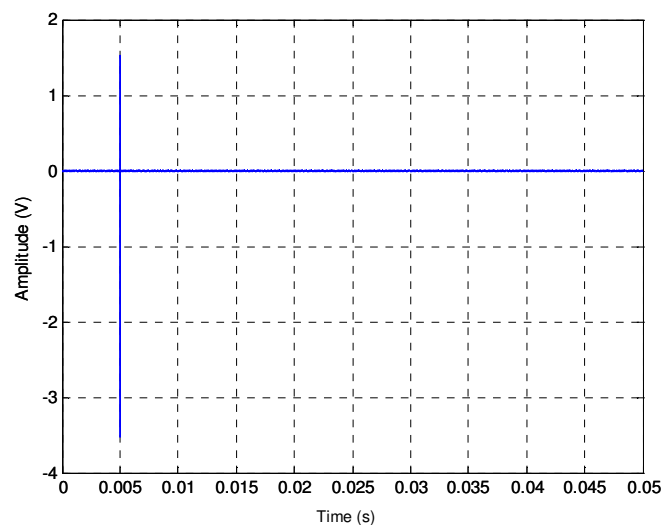


Figure 103: Short case – vacuum cleaner turning On event – 0.003 ms.

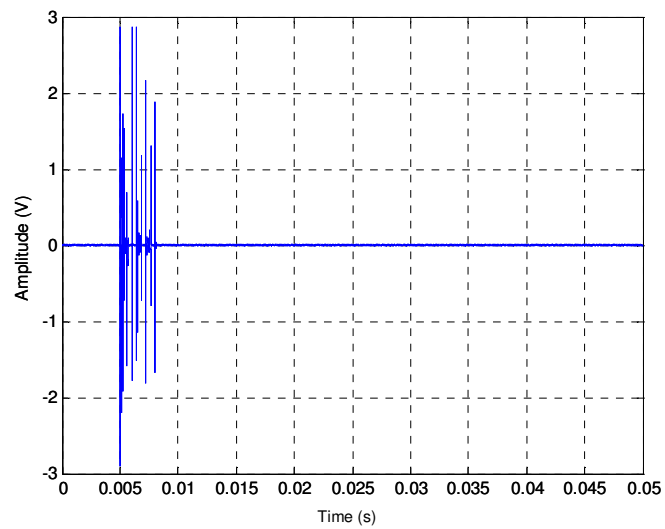


Figure 104: Long case – Iron thermostat On event – 3.1 ms.

11.2.2 Class 2 Model

11.2.2.1 Class 2-2 Noises

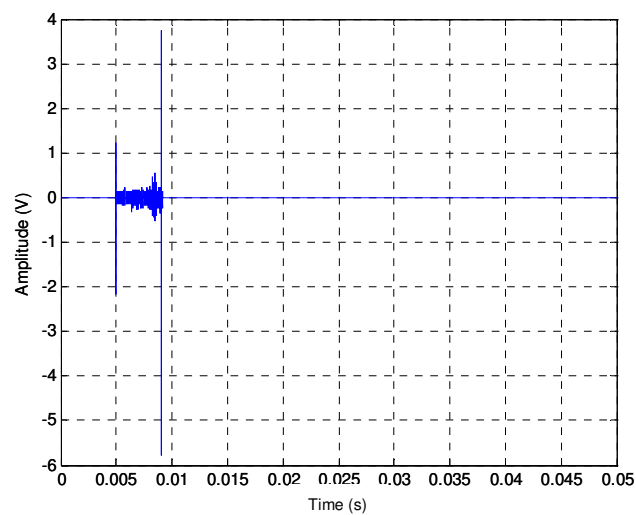


Figure 105: Mean case – Electrical heating thermostat Off event – 4.12 ms.

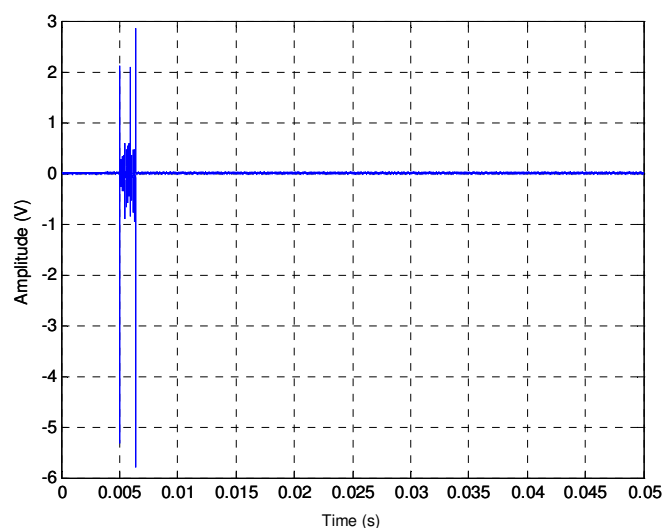


Figure 106: Short case – Paint burner Off event – 1.44 ms.

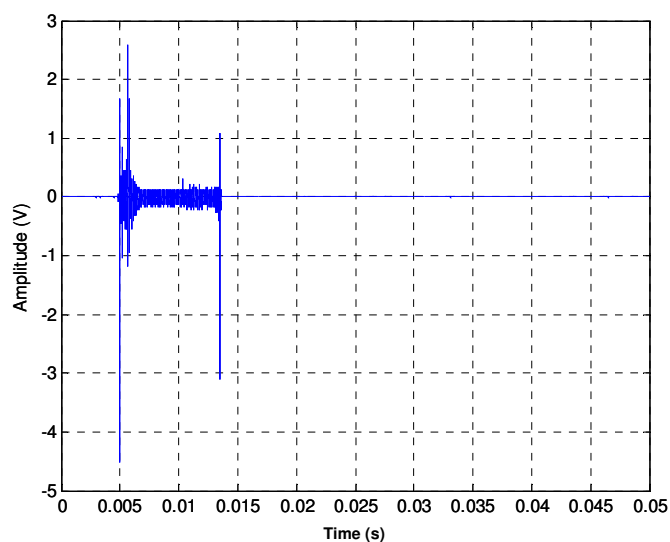


Figure 107: Long case – Paint burner Off event – 8.6 ms.

11.2.2.2 Class 2-1 Noises

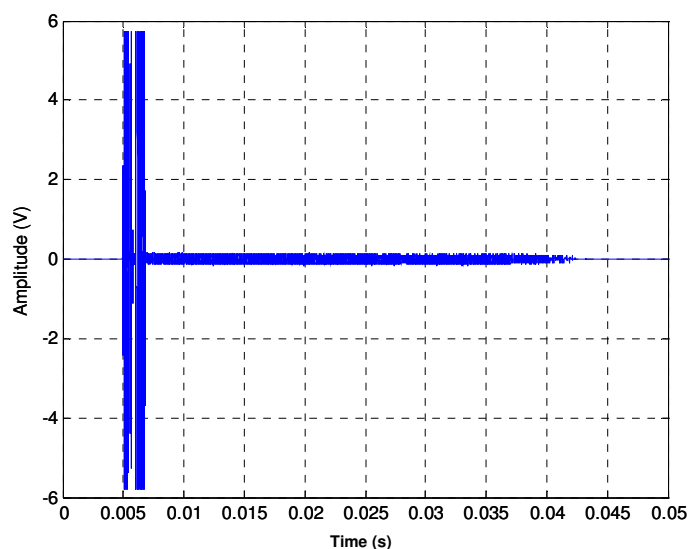


Figure 108: Mean case – Fluorescent lamp Off event – 1.8 ms.

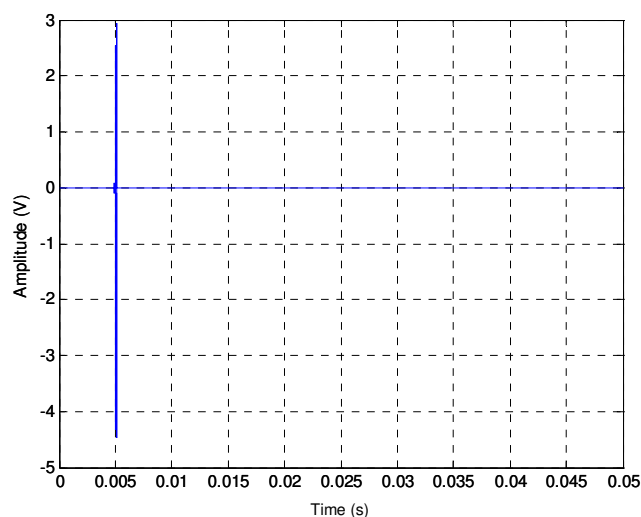


Figure 109: Short case – Refrigerator door closing event – 0.16 ms.

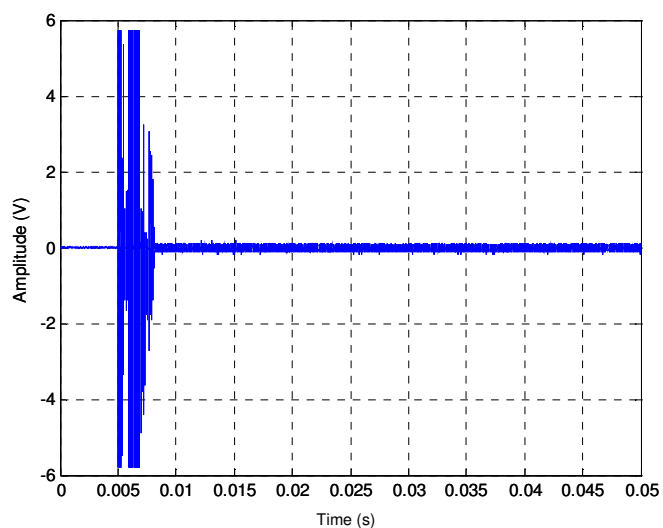


Figure 110: Long case – Fluorescent lamp Of event – 3.1 ms.

11.2.3 Class 3 Model

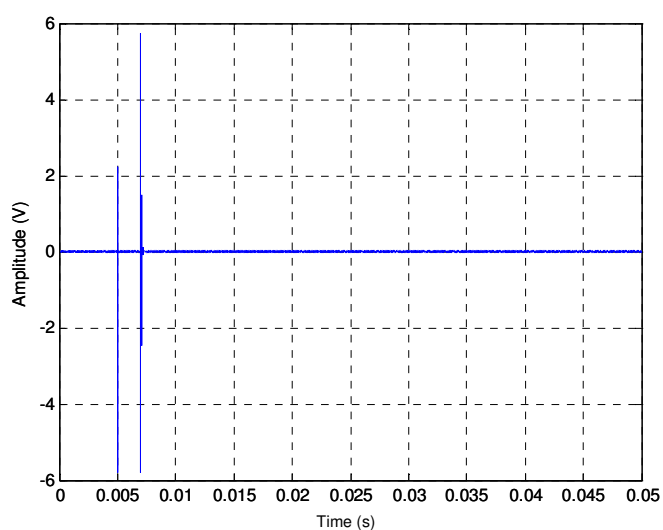


Figure 111: Mean case – Vacuum cleaner plug plugging event – 2 ms.

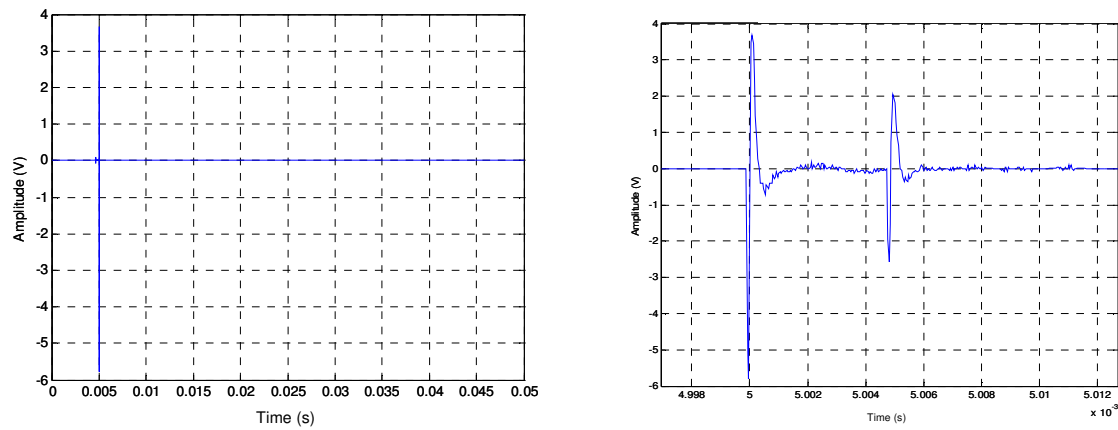


Figure 112: Short case – Vacuum cleaner plug plugging event – 0.006 ms.

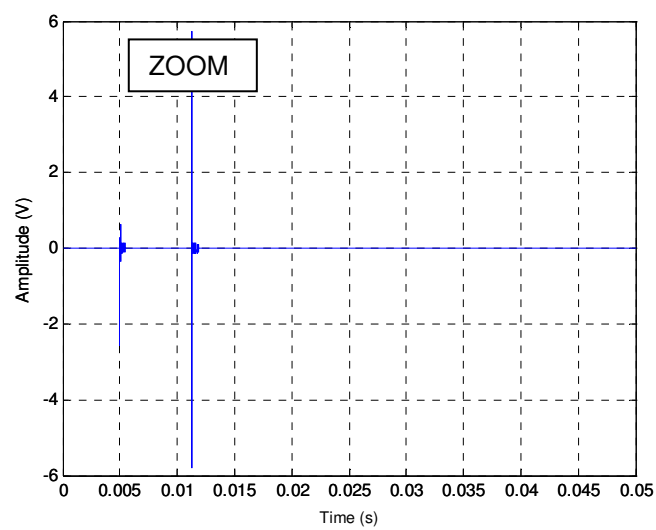


Figure 113: Long case – Vacuum cleaner plug plugging event – 6.8 ms.

11.2.4 Class 4 Model

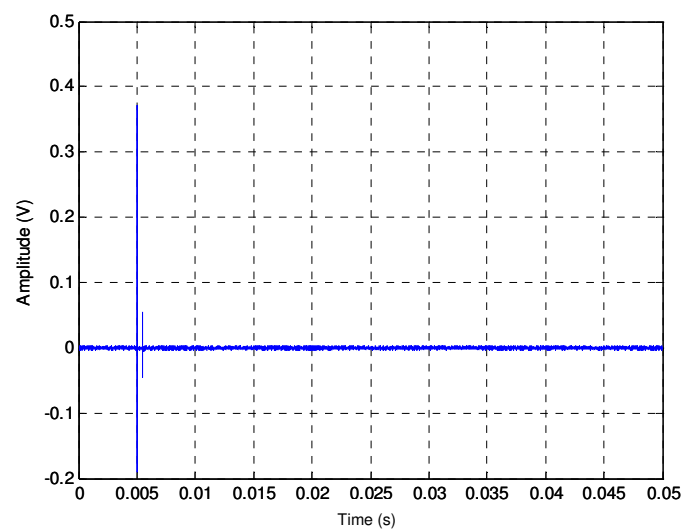


Figure 114: Mean case – Laptop power adapter plug unplugging event – 0.52 ms.

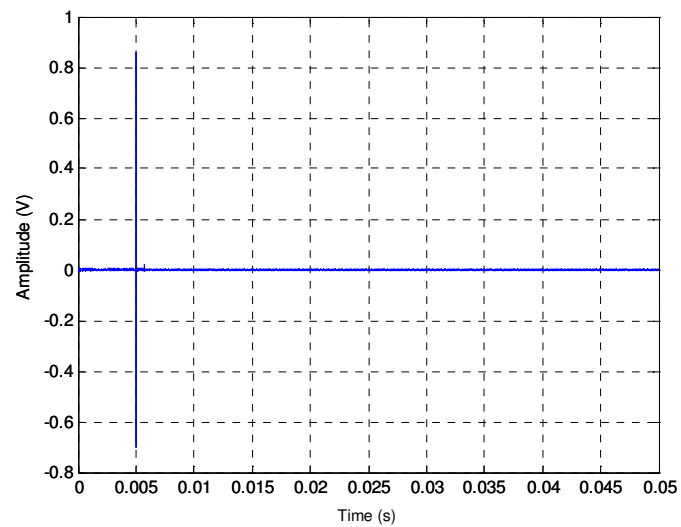


Figure 115: Short case – Laptop power adapter plug unplugging event – 0.012 ms.

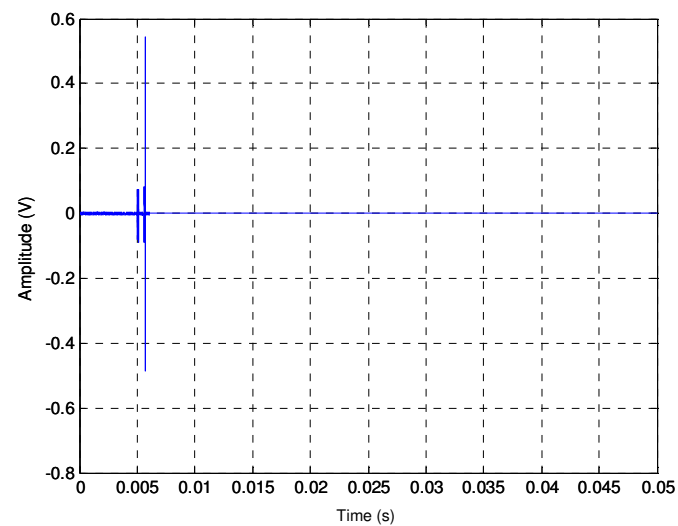


Figure 116: Long case – Laptop power adapter plug unplugging event – 0.73 ms.

11.2.5 Class 5 Model

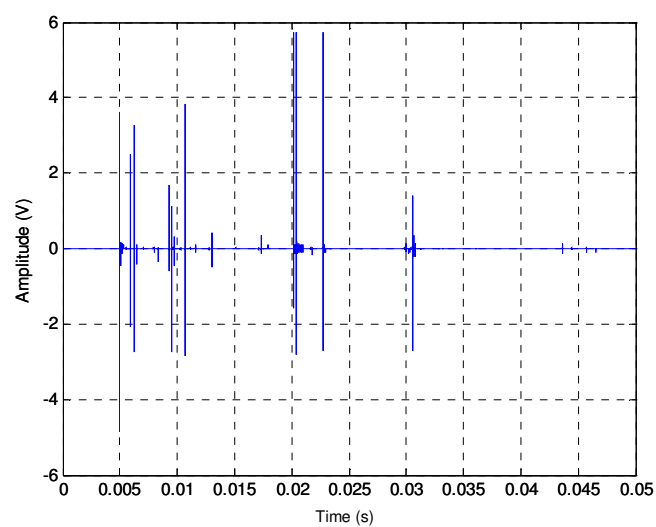


Figure 117: Mean case – Can opener On event – 26 ms.

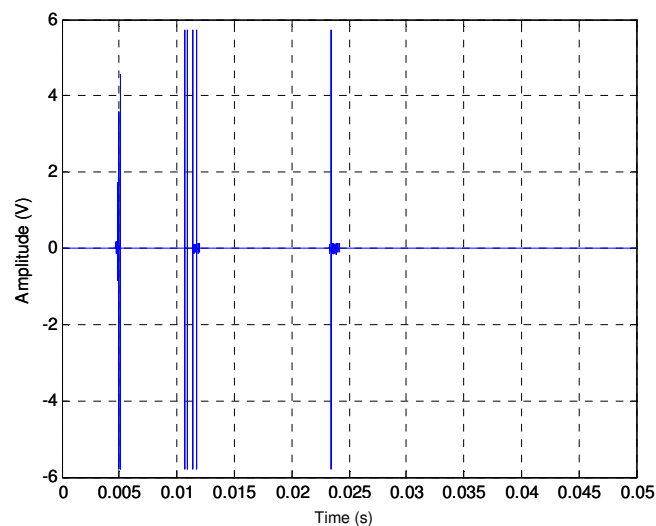


Figure 118: Short case – Fluorescent lamp On event – 18 ms.

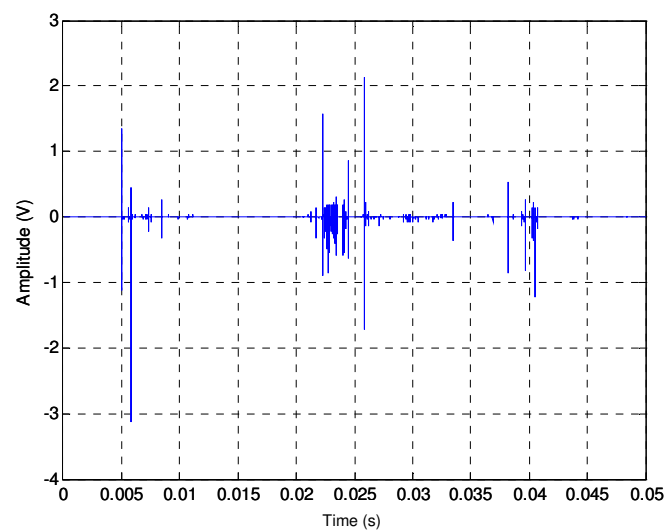


Figure 119: Long case – Can opener On event – 36 ms.

11.2.6 Class 6 Model

11.2.6.1 Class 6-S Noises

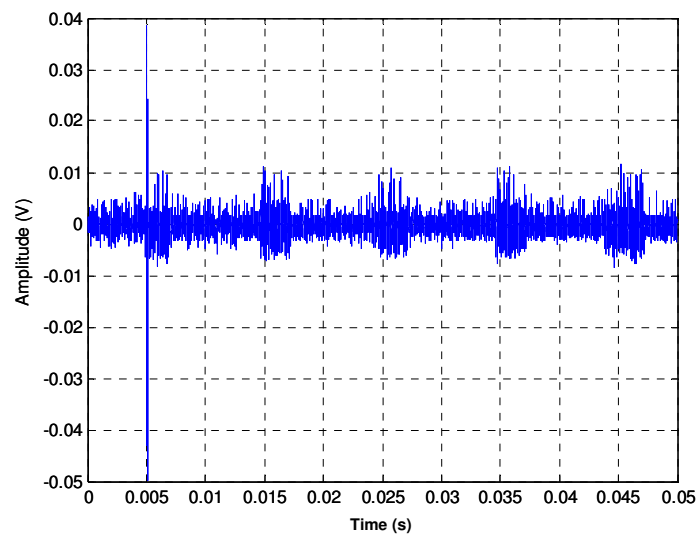


Figure 120: Mean case – Residential Gateway IP Phone pick up event – 0.17 ms.

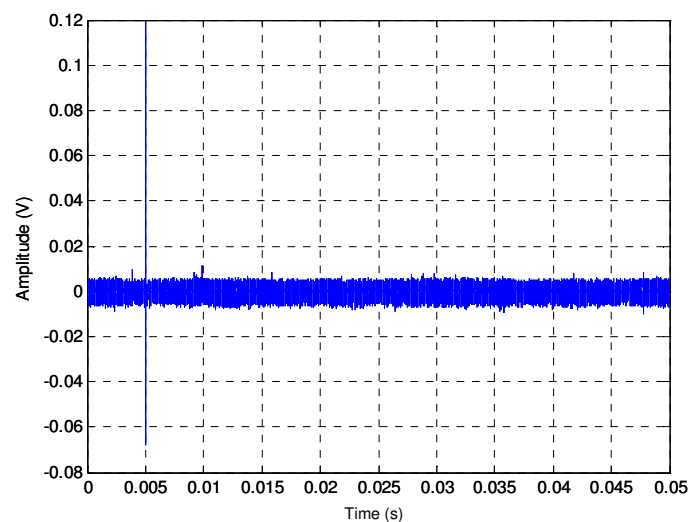


Figure 121: Short case – Induction Hob On event – 0.01 ms.

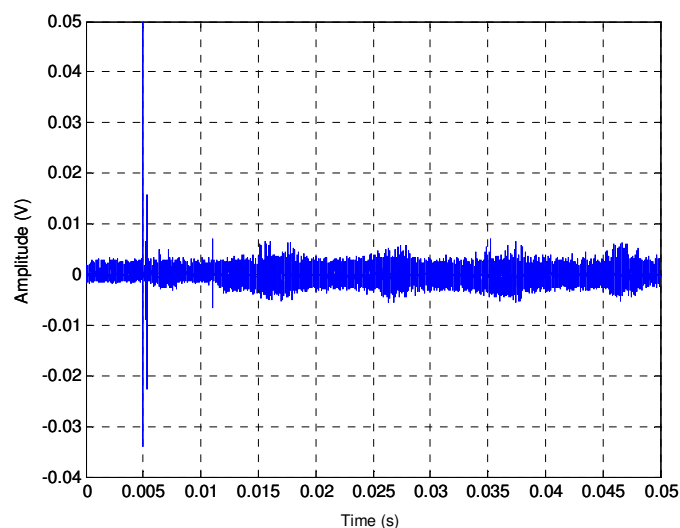


Figure 122: Long case – Residential Gateway IP Phone pick up – 0.29 ms.

11.2.6.2 Class 6-L noises

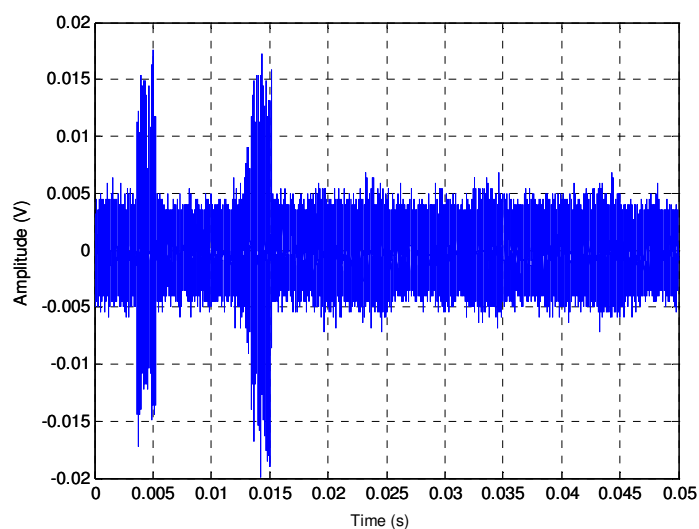


Figure 123: Mean (=short) case – Flat TV On event – 12 ms.

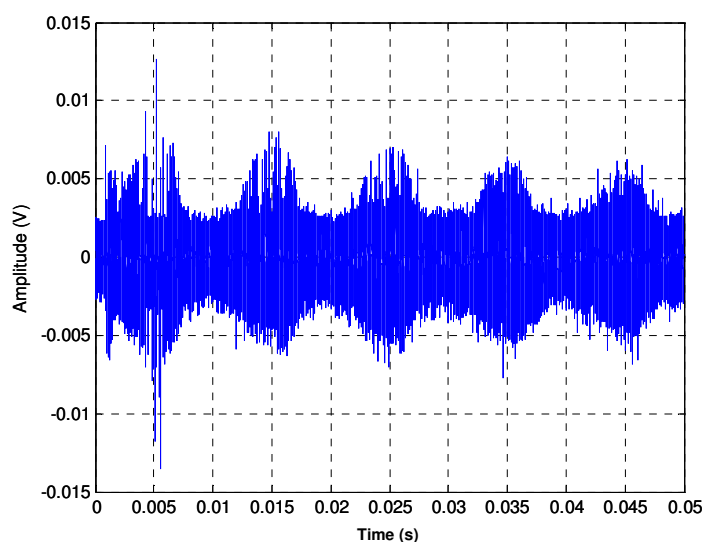


Figure 124: Long case – Laptop On event – 48 ms.

